ORE GENESIS OF THE EE3 GOLD PROSPECT IN THE THONE MYAE SONG AREA, BANMAUK DISTRICT, NORTHERN MYANMAR

テッ, サンダー, アウン

ORE GENESIS OF THE EE3 GOLD PROSPECT IN THE THONE MYAE SONG AREA, BANMAUK DISTRICT, NORTHERN MYANMAR

A thesis submitted in partial fulfillment of the requirements
for the degree of

DOCTOR OF ENGINEERING

By

HTET SANDAR AUNG

Department of Earth Resources Engineering,
Kyushu University

January 2021
Fukuoka, Japan

This work is dedicated to my beloved parents,

U HLA AUNG and Daw MYA MYA,

For a lifetime of love

With love and respect.....

ABSTRACT

Several gold deposits are found in the Central Magmatic-Volcanic Belt (CMVB) of Myanmar, which forms a nearly N-S trending, 1500 km long arc extending from the Andaman Sea to northern Myanmar. The arc consists of Cretaceous granitoids intruded into folded andesites and pillow basalts (the Mawgyi Andesite) which rest on cherts, talc-schists, mudstones and phyllites. The EE3 prospect is part of the Thone Myae Song deposit, located in the Kawlin-Wuntho Block in the northern part of the CMVB. In this area, there have been many small-scale local gold mines since 1980, not only primary but also alluvial gold mines. There are three gold prospects in the Thone Myae Song area such as the EE3 prospect, the Myauk Let Sho prospect, and the Thapan Aing prospect. The gold mineralization is hosted by Mawgyi Andesite. This dissertation describes the characteristics of the gold mineralization of the EE3 prospect based on field observation, ore mineralogy, fluid inclusion and sulfur isotope study. The main purpose of this study is to constrain the condition of gold mineralization in the EE3 prospect. This dissertation consists of the following seven chapters.

Chapter 1 introduces the location of the research area, previous works of the surrounding area, problem statements, thesis aims and objectives, research methodology, field work and sample collection, laboratory works, and expected outcome.

Chapter 2 reviews the geological background and tectonic setting of the study area including tectonic belts related with most important gold deposits surrounding the study area, including Kawt-a-Bum-Mt Loimye Segment, Wuntho-Banmauk Segment, Monywa-Salingyi Segment and Mount Popa Segment in the Wuntho-Popa Arc. The Thone Myae Song deposit is located in the Wuntho-Banmauk Segment in the Wuntho-Popa Arc.

Chapter 3 presents the regional geology, and deposit geology which describes field observation, megascopic, and microscopic study of the Mawgyi Andesite, mudstone and phyllite (Shwedaung Formation), shale and sandstone (Wabo Formation). Lower Cretaceous Mawgyi Andesite is the most widespread and most distinctive volcanic rock of the study area. Upper Triassic mudstone and phyllite are overlain by Mawgyi Andesite.

Chapter 4 demonstrates the hydrothermal alteration related to gold mineralization at the EE3 prospect. Hydrothermal alteration along the quartz veins in the area encompasses proximal (sericite-calcite alteration), intermediate (epidote-calcite±albite alteration) and distal (chlorite-calcite alteration) alteration zones that are defined by mineral assemblages. The strongly altered rocks adjacent to auriferous quartz veins are typically enriched in sulfide minerals. Further away from the vein, the alteration is characterized by various amounts of chlorite and calcite, but the proximal parts of the vein comprise epidote, quartz, chlorite, sericite and carbonate minerals.

Chapter 5 discusses the mineralization style of the EE3 prospect and paragenesis of the deposit. The ore body forms as massive sulfide quartz veins. Based on the mineral assemblages and cross-cutting relationships, three mineralization stages are defined: (1) N-S trending quartz-calcite-sulfide main veins (V1) (Stage-I), (2) E-W trending quartz-calcite vein (V2) that intersected the main veins (Stage-II), (3) the third generation quartz-calcite veins (V3) parallel to the main veins (Stage-III). Stage-I is the earliest sulfide-forming stage. Stage-I veins contain pyrite, chalcopyrite, sphalerite, magnetite and native gold. Stage-II veins contain pyrite with very rare chalcopyrite. The Stage-II is not accompanied by significant gold mineralization. Calcite commonly occurred in this stage. Stage-III veins contain pyrite, chalcopyrite, magnetite, native gold, tellurobismuthite, calaverite and petzite. Tellurobismuthite often coexists with chalcopyrite and pyrite.

Chapter 6 delivers the study on fluid inclusions of the EE3 prospect. This study on the EE3 prospect recognizes three types of fluid inclusions in the Stage-I mineralized

quartz veins: Type-A: two-phase, liquid-dominated, liquid (L)+vapor(V) inclusions. Type-B: two-phase, vapor-dominated, vapor (>60 vol%) + liquid inclusions. Type-C: three-phase, (liquid H_2O + carbonic liquid + carbonic vapor) inclusions. On the other hand, in the Stage-II veins and Stage-III veins, Type-A and Type-B fluid inclusions are found. The homogenization temperatures of Type-A fluid inclusions of Stage-I veins range from 180 to 360 °C (mode at 310 °C), with salinities ranging from 0.3 to 9.2 wt. % NaCl equivalent. The homogenization temperatures of the Type-B fluid inclusions range from 315 to 430 °C (mode at 350 °C) with salinities varying from 0.5 to 6.4 wt. % NaCl equivalent. The homogenization temperatures of Type-C inclusions vary from 220 to 356 °C (mode at 310°C), with corresponding salinities range from 1.2 to 7.4 wt. % NaCl equivalent. Type-A fluid inclusions in Stage-II veins yielded homogenization temperatures ranging from 176 to 387 °C (mode at 310 °C), with corresponding salinities range from 1.7 to 8.8 wt. % NaCl equivalent. The homogenization temperatures of the Type-B fluid inclusions range from 287 to 436 °C (mode at 410 °C) with salinities ranging from 3.5 to 11.1 wt. % NaCl equivalent. The homogenization temperatures of Type-A fluid inclusions in Stage-III veins range from 158 to 340 °C (mode at 210°C), with corresponding salinities range from 0.5 to 10.6 wt. % NaCl equivalent, while the homogenization temperatures of the Type-B fluid inclusions range from 278 to 464 °C (mode at 350 °C) with salinities ranging from 0.9 to 7.5 wt. % NaCl equivalent. Based on the coexistence of Type-A fluid inclusions and Type-B fluid inclusions, the formation temperature and pressure conditions were estimated from the fluid inclusions assuming boiling conditions, at 180 °C and 28 bars for Stage-I, 176 °C and 26 bars for Stage-II and 158 °C and 21 bars for Stage-III, which correspond to formation depths of about 300 m, 260 m and 215 m, respectively. Therefore, the condition of mineralization at the EE3 prospect corresponds to an epithermal system. The $\delta^{34}S$ values of the sulfides narrowly

range from +0.5 ‰ to -3.0 ‰, indicating that sulfur was most likely derived from the volcanic rocks that host the mineralization or a magmatic source at depth.

Chapter 7 presents conclusions of this thesis by general conclusions and recommendations for further research on this area.

ACKNOWLEDGEMENTS

I would like to give my gratitude to the members of my dissertation committee, Professor Dr. Koichiro Watanabe, Professor Dr. Akira Imai, Associate Professor Dr. Kotaro Yonezu, Assistant Professor Dr. Thomas Tindell because this research would not have been successful without their help, guidance, and support from many people during my study at Kyushu University.

I am deeply grateful to Japan International Cooperation Agency (JICA), SHIGEN NO KIZUNA program, for the PhD scholarship and financial support.

I would like to express my honest grateful to Professor Koichiro Watanabe, Department of Earth Resources Engineering, Kyushu University in Japan for his kind support and encouragement to carry out this research work, advice and reading thesis and give facilities in varies ways.

I would like to express my deepest grateful to Professor Akira Imai, Department of Earth Resources Engineering, Kyushu University in Japan for his valuable time to review draft of my dissertation and contributing the crucial ideas, valuable suggestions, helpful comment and disapproval in order to advance the quality of this dissertation. This dissertation would never successfully complete without his supervision, kind support and good instructions.

I am deeply gratitude goes to Associate Professor Kotaro Yonezu, Department of Earth Resources Engineering, Kyushu University in Japan for his kindness, considerate, supporting, encouragement and guidance me a lot during my study in Japan. Associate Professor Yonezu provide me the opportunities to join many field trips, it made me have a chance to learn and expand my knowledge related to economic geology and my study.

I am deepest grateful to Assistant Professor Dr. Thomas Tindell, Department of Earth Resources Engineering, Kyushu University in Japan for his suggestions, encouragements, advices, kindness and crucial reading during the preparation of thesis.

I would like to express thanks to Professor May Thwe Aye, Department of Geology, University of Yangon in Myanmar for her carried out this research work and good advice, suggestions, practical guidance and valuable references.

My special thanks to Professor Khin Zaw, CODES Centre of Ore Deposit and Earth Sciences, University of Tasmania, Australia for his valuable suggestions and critical reading an earlier version of the manuscript and provided valuable advice to improve the manuscript.

I deeply thanks to Professor Aye Thidar Mon, Department of Geology, Taung Oo University in Myanmar for her kind permission to study in Japan.

I would like to express my deepest thanks to U Maung Ko (Eternal mining group Co. Ltd) for allowing and supporting to the field research in the Thone Myae Song area, Banmauk Township, Sagaing area, Northern Myanmar. On the other hand, I would like to give thanks to Naw Taing (geologist), Dehlaing Zaw (geologist) and Mi Sanay Ma (geologist) for field works in mine site.

I would like to greatly thankful to the lab secretary, Ms. Mami Mampuku for her support related documents. I also thank Manuel Augusto Manuel Nopeia and all the lab member from Economic Geology Laboratory, Department of Earth Resources Engineering for their helping hand assistances with analyses, their useful suggestions for me for all circumstances during this PhD period.

Ultimately, my greatest thankful to my parents, sister and brothers, without whose addition their warm love, support and encouragement this work would not be completed.

TABLE OF CONTENTS

LIST OF FIGURES

LIST OF TABLES

CHAPTER 1

INTRODUCTION

1.1 General Statement

1.1.1 Gold Mining in Myanmar

Myanmar is a highly prospective but poorly explored orogenic terrane. Despite limited past exploration, it is known to be well endowed in a diversity of mineral deposits, hosting important known reserves of varying economic significance of tin, tungsten, copper, gold, zinc, lead, nickel, silver, jade and gemstones (e.g., Chibber, 1934a, b; Brown, 1936; Griffith, 1956; Soe Win and Marlar Myo Myint, 1998; Gardiner et al., 2014; Khin Zaw, 2017; Mitchell, 2017). Most of the mineral deposit of the Myanmar has not been systematically investigated yet in detail. Gold deposits in Myanmar remain underexplored and underdeveloped but retain considerable future potential. During recent years, gold exploration is becoming more interest factor among minerals exploration and it is also one of most economic exchange mineral resource in Myanmar.

Myanmar has more than 300 gold occurrences. Gold deposits are classified as either primary deposit or placer deposit. Other potentially significant primary gold deposits and the distribution of some alluvial (placer) gold deposits is shown in Figure 1.1. Most of Primary gold deposits and placer gold deposits are situated northern and central part of Myanmar. The gold deposits of Myanmar can be classified into many types, such as epithermal deposits, porphyry-related, slate-belt type, granite related type, ophiolite-related type, placer gold deposit and unclassified class.

The dominant primary gold deposits of the research area are Kyaukpazat gold mine, Kyaukpahto gold mine and Shangalon gold mine show in Figure 1.1. The Kyaukpazat gold mine lies within the north-south trending central magmatic arc, also known as Central Magmatic Volcanic Belt, in which middle Cretaceous and younger

granodioritic batholith and plutons intruded a thick folded sequence of basaltic andesite and basaltic pillow lava named Mawgyi andesite (Mitchell et al., 1999). Gold mineralization is mainly confined to NNW-SSE and E-W trending gold-sulfide bearing quartz±carbonate veins in the Mawgyi andesite and associated metasedimentary rocks of the Shwedaung Formation. Small diorite bodies also intruded along the NW trending Legyin fault between the Mawgy Andesite and Shwedaung Formation. All of the mineralized zones at the Kyaukpazat mine area are intensively shared and broken due to post-ore fault movements (Cho Aye, 2007). Kyaukpahto deposit is located within the Sagaing Fault zone. Gold mineralization is mainly kept to the northeast-southwest trending extensional faults developed within the shear couple formed between Sagaing and Kyauktan Faults. In the Kyaukpahto gold mine, native gold occurs as stockworks and dissemination with localized breccia zones in silicified arkosic sandstone of the Male Formation (Eocene). The Shangalon-Kyungalon Cu-Au (Mo) ore district is situated on the south-eastern margin of the Kanzachaung batholith in the Wuntho-Popa Arc, Myanmar. In Shangalon, the main copper mineralization is closely related to hydrothermally altered gabbroic diorite, quartz diorite, tonalite porphyry and diorite porphyry. The mineralization style of Shangalon is characterized by dissemination, vein-lets and minor stockworks (Thiri Ye Htut et al., 2020). The estimated ore reserve at Shangalon is about 9 million tons (Cu: 0.23%; Au: 0.17 g/t; United Nations, 1978b).

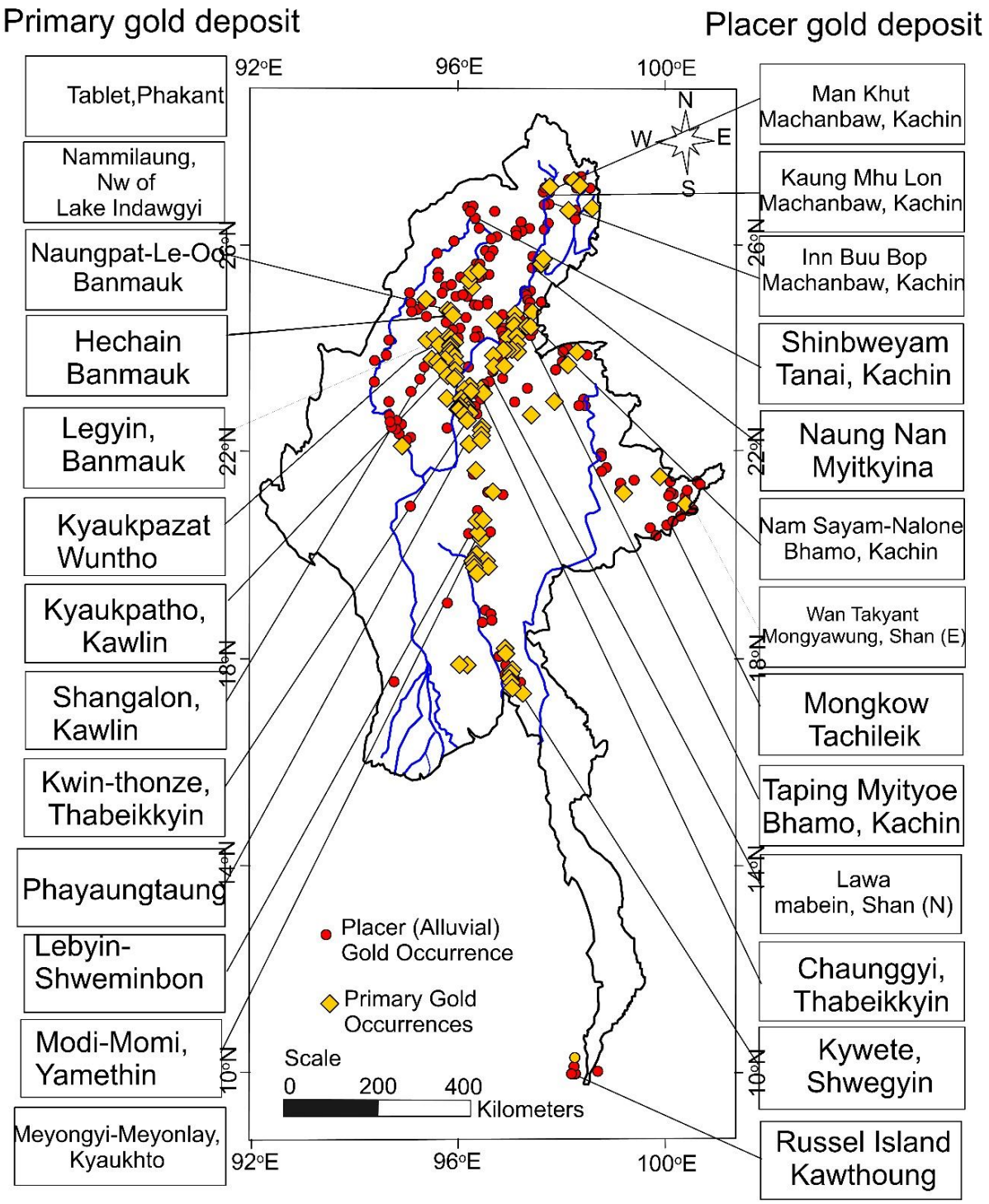

Figure 1.1 Primary and placer gold deposits in Myanmar (modified Ye Myint Swe et al., 2017.)

1.2 Background

Gold deposits in Myanmar occur in six main tectonic belts: (1) porphyry-type copper ± gold ± molybdenum and related epithermal gold mineralization as well as intrusion-related and orogenic gold-quartz veins in the Central Magmatic Arc or Central Magmatic-Volcanic Belt, (2) orogenic gold mineralization along the Tagaung–Myitkyina Belt, (3) skarn gold-copper and gold–quartz veins in marble and granite within the Mogok Metamorphic Belt, (4) sedimentary rock-hosted epithermal gold mineralization along the Sagaing Fault Zone, (5) orogenic gold–quartz veins and skarn-type deposits in Mergui Belt, (6) gold-sulfide-bearing quartz veins hosted in ophiolitic units and greenschists in the Jade Mines Belt (Ye Myint Swe et al., 2017; Khin Zaw, 2017) (Figure1.2).

The Central Magmatic Arc is situated between the Tertiary sediments of the forearc and back-arc basins. Most of volcanoes (e.g Taung Thonlong volcano, Mt. Popa) occur along the Central Magmatic Arc. From Mt Popa northwards to the Wuntho–Banmauk region, has potential for porphyry Cu ± Au ± Mo mineralization and associated low- and high-sulfidation epithermal gold mineralization in the Central Magmatic Arc.

The gold deposits occur in the form of auriferous quartz veins throughout the Naung-Pat area, Le-Oo, He-Chein, Thone Myae Song, Legyin and Kyaukpazat, Sadwin and Shangalon area in the Wuntho–Banmauk district, Monywa–Salingyi area and the Myesaytaung (Lepandan) area in the Central Magmatic-Volcanic Arc (Fig. 1.2).

The Thone Myae Song gold deposit is located in the Central Belt or Wuntho-Popa Arc in the northern part of Myanmar. The arc is exposed further west in the Wuntho area near Banmauk, with granitoids intruded into folded andesites and pillow basalts (the Mawgyi Andesite) which rest on cherts, talc-schists, mudstones and phyllites (United Nations, 1978; Mitchell, 1993). The Mawgyi Andesite has been interpreted by Mitchell (1993) to represent an oceanic volcanic arc thrusted over the West Myanmar Block as a

nappe during the Cretaceous. Gold mineralization in the Banmauk-Wuntho district is found principally as gold-bearing quartz or quartz-carbonate veins, which are exploited by small scale mining at grades of 20-100 g/t Au (Mitchell et al., 1999), and the most veins lie within the Late Cretaceous Kanza Chaung Granodiorite locally extending into the schist and volcanic country rocks (United Nations, 1978; Khin Zaw, 1990; Mitchell et al., 2012). There is no detailed research work on gold mineralization in the Banmauk district and ore genesis is poorly understood. In this study, we present the results of geological, geochemical and mineralogical investigations together with sulfur isotope and fluid inclusion studies on the gold mineralization of the EE3 Prospect in the Thone Myae Song area with the aim of elucidating the origin of ore-forming fluids the ore genesis of the prospect.

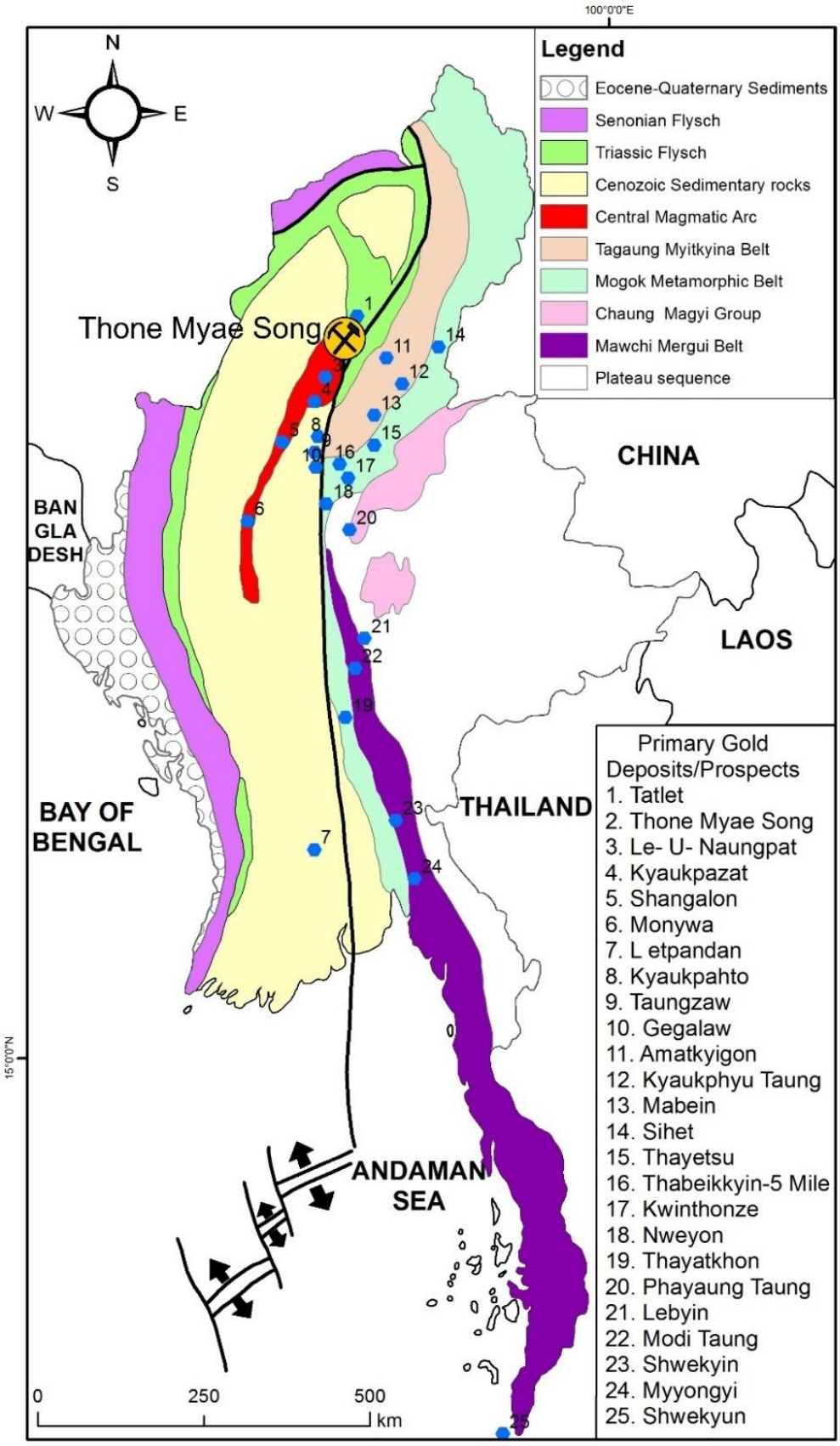

Figure 1.2 Major tectonic belts and location of important gold deposits and prospects in Myanmar including the Thong Myae Sone (EE3 Prospect area) (compiled after Mitchell et al., 1999; Khin Zaw et al., 2014; Ye Myint Swe et al., 2017).

1.3 Location of the Research Area

The study area is located about 35 km southern of Banmauk Township, Sagaing Region, Northern Myanmar (Figure 1.1). It is bounded by latitudes 24° 10′ 0″ N-24°13′ 20″ N and longitude 95° 52′ 40″ E-95° 55′ 0″ E 83 P/16 on a scale 1-inch to 1 mile (1:63360). The research area is easily accessible from Yangon to Banmauk by car. The EE3 Prospect is the one of the largest gold deposits in the Thone Myae Song area, Sagaing region, Northern Myanmar.

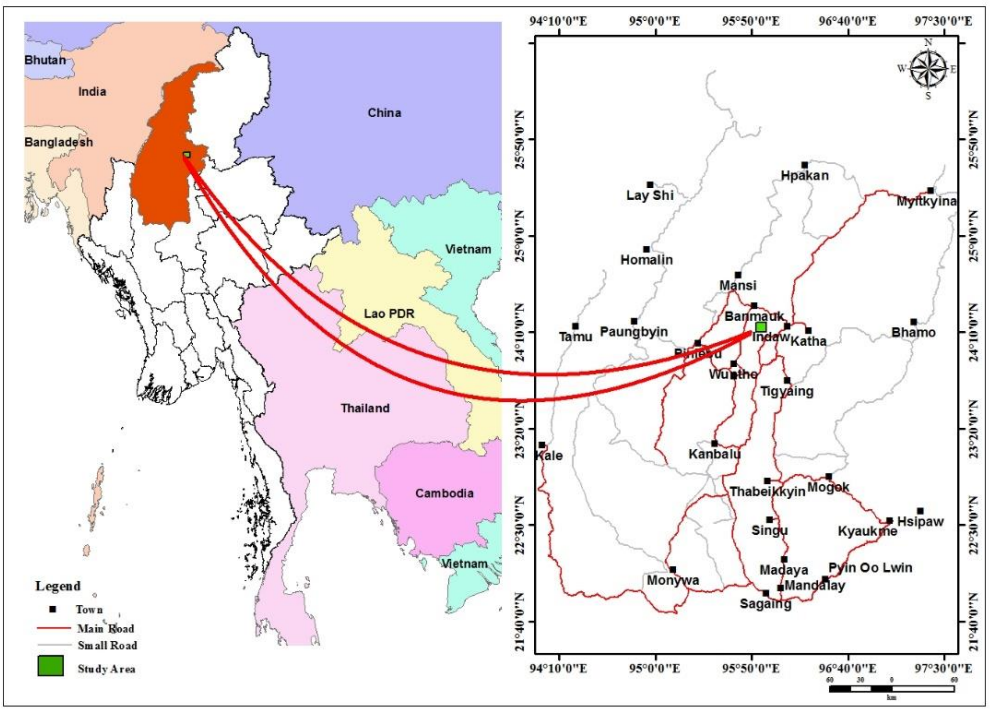

Figure 1.3 Location map of research area (Based on UTM 2495, 83p/16)

1.4 Previous Works of the Surrounding Area

Noetling, 1894. had made the first study on the general geology of the Wuntho area. He proposed that quartz diorite was chiefly developed in the Maingthon Hill Tract and occupied the central part of the region.

Chibber, 1934. mentioned about post-Eocene Orogenic period and igneous activity of Wuntho region and reported that Wuntho area has in situ gold and placer gold deposits.

Chibber, 1934. designated the area as the Wuntho Igneous Complex which comprised a large batholith of granitic rocks (mostly granodiorite) surrounded by a group of extinct volcanoes forming conical hill and dome, pyroclastic, ash beds and tuffs with basalt flows. According to him the igneous activity might have taken place in post-Eocene time under subaqueous conditions.

Geologists of the Department of Geological Survey and Exploration (D.G.S.E) and some UN experts carried out reconnaissance geological exploration and geological mapping in the study area under the G.S.E project in 1974-75.

In the year of 1982, Khin Maung Myint made detailed petrological studies in the Okkan-Ainggyi area (west of Kawlin) and Pinlebu area, respectively.

In 1983, F. Bender published out the regional geology, stratigraphy, tectonics and magmatism around Myanmar including about Wuntho Massif generally.

In 2004, Ohn Thwin studied that the systematic investigation of copper gold mineralization at Shangalon, Kawlin Township, Sagaing Region, Upper Myanmar. He studied systemically alteration, mineralization, structural controls, gold ore mineralogy and established deposit model of Shangalon copper-gold mineralization.

In 2011, Thiha Soe stated that the geology and geochemical characteristics of gold mineralization of Muthein-Hechein-Le-U area, Banmauk in his unpublished Ph. D Dissertation.

In 2011, Zaw Win mentioned that the petrology and economic significance of Pinlebu-Banmauk area, Sagaing region in his unpublished Ph. D Dissertation.

In 2016, Sithu Htun, wrote the Geology and investigation of Gold mineralization in Mansi-Naungpat Area of Bamauk Township, Sagaing Region in his unpublished MSc thesis.

In 2018, Mi Sanay Ma studied that Original and Geochemical Characteristic of Gold Mineralization in Thon Myae Song Area, Banmauk Township, Sagaing Region, Myanmar in her unpublished MRes thesis.

1.5 Problem Statements

There have not been studied in detail for geology and gold mineralization in the Thone Myae Song gold Deposit, Banmauk district. There was no research to mention the detailed investigation of origin and types of the gold mineralization in this study area. Therefore, detailed research work is still required for the characterization and verification of mineralization, related rocks, alteration mineralogy and zoning, ore and gangue mineralogy, geochemistry, characteristics of hydrothermal fluids, characteristics and paragenetic sequences of mineralization, control on the ore mineralization and formation, and origin and evolution of hydrothermal system.

1.6 Thesis Aims and Objectives

The current research will effort to clarify the geological, geochemical characteristics and paragenesis of gold mineralization of the EE3 Prospect, Thone Myae Song area, Sagaing region, Northern Myanmar. This research will focus on the following aims;

To make the detail geological map of the study area.

1. To define the petrological characteristics of host rock and related ore minerals.
2. To classify hydrothermal alteration of the host rock related to ore mineralization.
3. To observe the origin and types ore deposit of the gold and associated mineralization.
4. To classify the origin of hydrothermal fluid responsible for mineralization.
5. To study sulfur isotope in order to understand about source of mineralized fluid.
6. To compare the nature of these deposits with other similar types of deposits.

1.7 Research Methodology

The methodology consists of two sections; field investigation and laboratory analysis. The research laboratory works of mineralogical and geochemical analyses have been supported out.

1.7.1 Field Work and Sample Collection

In the PhD study, the author collected samples in three field periods (September 2016, December 2016, December 2017). Throughout the field works, rock samples and geological data were collected to make detail for the geological map, to consider the structural and lithological controls on mineralization, to determine geological, geochemical characteristics and alteration studies, to collect the representative samples from host rock and characteristics of gold mineralization.

1.7.2 Laboratory Works

A total of about 200 samples of volcanic rocks, altered rocks, and ores assemblages were collected during the field investigation in this study. Fifty-five samples were collected from the underground workings at the EE3 Prospect.

Thirty petrographic thin sections and forty polished sections were prepared to examine textural characteristics of the rocks, alteration minerals and ore minerals with Nikkon Eclipse E600 POL microscope equipped with an AdvanCam-U3II camera at the Department of Earth Resources Engineering, Kyushu University.

The first stage of the preparation for X-ray diffractometry (XRD) on bulk rock, rock samples were roughly crashed using a hammer at first, and then used Agate motor. The samples were then scanned using the XRD spectrometer. The intensity of the diffracted X-ray is measured as a function of the diffraction angle (2θ). These diffraction patterns are used to identify the mineral species. An approximate sample size of the size

of 1cm3 (powder, 10μm) is required. Both on bulk and clay fraction, X-ray diffraction analysis were directed to classify mineral composition, alteration mineral assemblage using a Rigaku Ultima IV under the condition of 50kV and 40mA at Department of Earth Resources Engineering, Kyushu University, Japan.

A scanning electron microscope equipped energy dispersive X-ray spectroscopy (SEM-EDX) SHIMADZU SUPERSCAN SS-550, equipped with energy disperse X-ray analyzer (EDAX) was used to determine the chemical composition and confirmation ore mineral at the Center of Advanced Instrumental Analysis, Kyushu University.

30 representative samples were carefully chosen for whole-rock geochemistry. The concentration of major and minor elements of 30 fresh andesitic rocks were prepared by crushing to small pieces with a hammer and then by powdering to 200-mesh using an alumina disk mill. Concentrations of major and trace elements were determined by X-ray fluorescence spectroscopy (XRF) using a RIGAKU RIX-3100 under the condition of 30 kV and 70mA manufactured by Rigaku Corporation, at the Department of Earth Resources Engineering, Kyushu University. Loss on ignition (LOI) was determined by heating the samples at 1000 °C for 2 h to determine relative weight loss. The sample pellets XRF analysis were prepared by pressing at 20t about 2 minutes in a vinyl chloride ring. The standard JA-3 andesite (Imai et al., 1995) was repeatedly analyzed to monitor precision, yielding an error of less than ± 5%.

About 300 fluid inclusions in seven vein quartz samples were examined in this present study. The detailed microthermometric data are presented mainly on fluid inclusions in vein quartz, hosted in andesites. Fluid inclusion microthermometry on doubly polished sections was conducted at the Department of Earth Resources Engineering, Kyushu University, Japan. Microthermometric analyses were carried out using a Linkam LK600 heating–freezing stage with a Nikon Y-IM microscope. The errors for the temperature measurements were ±0.5, ±0.2, and ±2.0 °C for runs in the range of

−120 °C to −70 °C, −70 °C to 100 °C, and 100 °C to 600 °C, respectively. The final ice-melting temperatures were measured at a heating rate of less than 0.1 °C/min and the homogenization temperatures at a rate of ≤1 °C/min. Total salinities for aqueous fluid inclusions were calculated from final melting temperatures of ice according to Bodnar (1993) and are expressed as wt. % NaCl equiv. The salinities of the CO_2-H_2O inclusions were calculated from the melting temperature of clathrate (Roedder, 1984).

Total salinities for NaCl–H_2O fluid inclusions were calculated from the final ice melting temperatures using the equation of wt. % NaCl = 1.78 T − 0.0442 T_2+ 0.000557 T_3, where T is depression temperature in °C, and is expressed as wt. % NaCl equv. The salinities of CO2-bearing fluid inclusions were calculated using the melting temperatures of clathrate and had standard errors of ±1.0° and ±0.2°C, (in presence of CO_2 vapor and CO_2 liquid) is a function of salinity according to the following mathematical expression (Collins, 1979): wt.% NaCl = 15.52022 - 1.02342T - 0.05286$T_2$where T is the clathrate melting temperature expressed in °C.

Sulfur isotopes for sulfides were also measured on eighteen pyrite samples of the mineralized quartz veins of the EE3 Prospect. Samples preparation method are used of Yanagisawa and Sakai (1983). Sulfide minerals in whole-rock samples were reacted with HNO_3 and Br_2 and decomposed to change sulfur to sulfate. The sulfate was then immobile as barite ($BaSO_4$) using barium chloride solution ($BaCl_2 2H_2O$, 10%). All sulfur isotope analysis was carried out at Queen's University, Queen's Facility for Isotope Research. Sulfur samples were weighed into tin capsules and the sulfur isotopic composition measured using a MAT 253 Stable Isotope Ratio Mass Spectrometer coupled to a Costech ECS 4010 Elemental Analyzer. The results are reported using the delta (δ) notation in units of permil (‰) and are reproducible within ± 0.2 permil $\delta^{34}S$ values were calculated by normalizing the $^{34}S/^{32}S$ ratios in the sample to that of the Vienna Canyon Diablo Troilite (VCDT) international standard.

1.8 Expected Outcome

This research has number of benefits not only to produce more economical mineral resource but also for academic for economic geology for student and researchers.

In this research, we can know what kind of deposit these area and gold mineralization nature. This deposit can bring new geological context to gold mineralization in Myanmar for future exploration.

This research will also support design a regional strategy for gold mineral exploration and the structural control of ore formation and exploration style of mineralization. Moreover, add a new interpretation of geological, petrographical characteristics of hos rock and associated ores, mineralogical, geochemical knowledge of the deposit, petrogenesis and mechanisms of ore formative based on geochemical and fluid inclusion studies.

1.9 Thesis Organization

The dissertation consists of Seven chapters:

Chapter 1 is an Introduction which provides location of study area, previous works of the surrounding area, problem statement, thesis aims and objectives, research methodology and thesis organization.

Chapter 2 demonstrates background of research area, the tectonic setting including Kawt-a-Bum-Mt Loimye segment, Wuntho-Banmauk Segment, Monywa-Salingyi Segment and Mount Popa Segment in the Wuntho-Popa Arc and explain the regional structures of the research area.

Chapter 3 describes the regional geology of the other significant occurrences of the Banmauk gold district and deposit geology. It discusses Mawgyi Andesite unit, Granodiorite unit, Phyllite unit, Mudstone unit, Sandstone unit and Alluvium.

Chapter 4 presents a detailed description of hydrothermal alteration and mineralization of the EE3 prospect.

Chapter 5 A detailed paragenetic sequence for mineralization to determine the genesis of the gold mineralization in the EE3 prospect.

Chapter 6 discusses fluid inclusion microthermometry and sulfur isotopes. Results of Fluid inclusion microthermometry are presented and the origin of ore forming fluids of EE 3 prospect is discussed. Sulfur isotope analysis is also done to understand the source of mineralized fluid at the EE3 prospect.

Chapter 7 (General Discussion and Conclusions) gives general discussion, conclusion and recommendations for further research of EE3 prospect.

1.10 References

Brunnschweiler, R.O., 1966. On the geology of the Indoburma ranges. J. Geo. Soc. Aust. 13, 137-194.

Bender, F., 1983, Geology of Burma, Gebruder, Bomtraeger, Berlin, Stutgart. Best.

Brown, J.C., 1936. India's Mineral Wealth: A Guide to the Occurrences and Economics of the Useful minerals of the Indian Empire. Oxford, Oxford University Press, 335p.

Chibber, H.L., 1934a. The Geology of Burma, London, Mac Millan, 538.

Chibber, H.L., 1934b. The Mineral Resources of Burma, London, Mac Millan, 520.

Cho Cho Aye, Thacpaw, C., Ye Myint Swe, 2007. The nature and distribution of gold in the ores from Kyaukpazat Mine, Myanmar. Journal of Myanmar Academy of Arts and Sciences, 5, 57–69.

Collins, P.L.F., 1979. Gas hydrates in CO_2-bearing fluid inclusions and the use of freezing data for estimation of salinity. Econ. Geol. 74, 1435-1444.

Gardiner, N.J., Robb, L.J., Searle, M.P., 2014. The metallogenic provinces of Myanmar. Appl. Earth. Sci. 123, 25–38, https://doi.org/10.1179/1743275814Y.0000000049.

Griffith. S., 1956. The mineral resources of Burma, Min. Mag. 95, 9-18.

Imai, N., Terashima, S., Itoh, S., Ando, A., 1995. 1994 compilation of analytical data for minor and trace elements in seventeen GSJ geochemical reference samples, "Igneous rock series". Geost. Newslett. 19, 135–213.

Khin Maung Myint, 1982. A Petrological Study of the Okkan-ainggyi Area, West of Kawlin, MSc Thesis, University of Mandalay.

Khin Zaw, 1990. Geological, petrological and geochemical characteristics of granitoid rocks in Burma: With special reference to the associated W-Sn mineralization and their tectonic setting. J. SE Asian Earth Sci. 4, 293-335. https://doi.org/10.1016/0743-9547(90)90004-W.

Khin Zaw, Meffre, S., Lai, C.-K., Burrett, C., Santosh, M., Graham, I., Manaka, T., Salam, A., Kamvong, T., Cromie, P., 2014. Tectonics and Metallogeny of Mainland Southeast Asia- A Review and Contribution. Gondwana Res. 26, 5-30.

Khin Zaw, Ye Myint Swe, Tin Aung Myint, Knight, J. 2017. Copper deposits of Myanmar. In: Barber, A.J., Khin Zaw. Crow, M.J., Eds., Myanmar: Geology, Resources and Tectonics, Geological Society (London) Memoir, 48, 573-500. https://doi.org/10.1144/M48.26.

Mitchell, A.H.G., 1993. Cretaceous-Cenozoic tectonic events and Mergui Group nappe in Myanmar and Thailand. J. SE Asian Earth Sci. 7, 165-178.

Mitchell, A.H.G., Htay, N., Ausa, C., Deiparine, L., Khine, A. Po, S., 1999. Geological settings of gold districts in Myanmar. Proceedings of PACRIM congress 99, Bali, Indonesia., 303-309.

Mitchell, A.H.G., Chung, S.-L., Thura Oo, Lin, T.-H. Hung, C.-H., 2012. Zircon U-Pb ages in Myanmar: Magmatic-metamorphic events and the closure of a neo-Tethys ocean? J. Asian Earth Sci. 56, 1-23. https://doi.org/10.1016/j.jseaes.2012.04.019.

Noetling, F., 1894. Note on the geology of Wuntho in Upper Burma. Rec Geol. Survey India 27.4.115.124.

Ohn Thwin, 2004, Systematic investigation of copper gold mineralization at Shangalon, Kawlin Township, Sagaing Division, Upper Myanmar. PhD. Disseration, University of Yangon, Unpublished.

Roedder, E., 1984. Fluid Inclusions. Rev. Miner. 12, 644p.

Sithu Htun 2016, The Geology and investigation of Gold mineralization in Mansi-Naungpat area, Sagaing Region. MSc thesis. University of Yangon. Unpublished.

Soe Win, Marlar Myo Myint, 1998. Mineral potential of Myanmar. Resour. Geol. 48, 209-218.

Thiha Soe, 2011, Geological and Geochemical Characteristics of Gold Mineralization at Mutthein – Hechein – Le U Area, Banmauk (Unpublished Thesis).

Thiri Ye Htut, Qin, K., Li, G., Sein, K., Evans, N.J., 2020. Eocene arc magmatism and related Cu-Au (Mo) mineralization in the Shangalon-Kyungalon district, Wuntho-Popa Arc, northern Myanmar. Ore Geol. Rev. 125, https://doi.org/10.1016/j.oregeorev.2020.103678.

United Nations, 1978. Geology and Exploration Geochemistry of the Pinlebu-Banmauk area, Sagaing Division, Northern Burma. Technical Report No. 2, Geological Survey and Exploration Project, United Nations Development Programme, United Nations, New York. 1-53.

Yanagisawa, F., Sakai, H., 1983. Thermal decomposition of barium sulfate-vanadium pentoxide-silica glass mixtures for preparation of sulfur dioxide in sulfur isotope ratio measurements. Anal. Chem. 55, 985–987.

Ye Myint Swe, Cho Aye, Zaw, K., 2017. Gold Deposits of Myanmar. In: Barber, A.J., Zaw, K., Crow, M.J., Eds., Myanmar: Geology, Resources and Tectonics,

Geological Society (London) Memoir, 48, 557-572. https://doi.org/10.1144/M48.25.

Zaw Win 2011, Petrology and Economic Significant of Pinlebu-Banmauk Area, Sagaing Region, 1-128. (Unpublished Thesis).

CHAPTER 2

REGIONAL GEOLOGICAL SETTING

2.1 Background

The region records Paleozoic–Cenozoic Tethyan and Indian oceanic subduction, and continental collision among the India, West Burma, Sibumasu, and Indochina terranes (e.g., Mitchell 1993, 2018; Metcalfe 2013; Cai et al. 2017; Gardiner et al. 2016a; Zhang et al. 2017a, 2018). In Myanmar, an important N–S trending magmatic belt, named as the Wuntho–Popa Arc (WPA) or Central Magmatic Volcanic Belt, occurred in the West Burma terrane and consists of Cretaceous–Quaternary mafic–felsic volcanic rocks and intrusions (Gardiner et al. 2017, 2018; Zhang et al. 2018). During ~ 110–90 Ma high-angle subduction of the Neo-Tethyan oceanic lithosphere, partial melting of metasomatized mantle wedge by slab-derived fluids and/or melt-formed basaltic melts, which ascended and underwent fractional crystallization to produce gabbroic–dioritic intrusions. Reversely, coeval magmatic rocks in the West Burma, western Sibumasu, and Tengchong terranes might be caused by the relatively small size of the West Burma terrane during low-angle subduction of the Neo-Tethys oceanic lithosphere Figure 2.1. Cretaceous (~ 110–90 Ma) mafic–felsic intrusions in the West Burma terrane may have formed in an arc setting during subduction of the Neo-Tethyan oceanic lithosphere, suggesting a prolonged Neo-Tethyan magmatic arc system from southern Tibet to Southeast Asia.

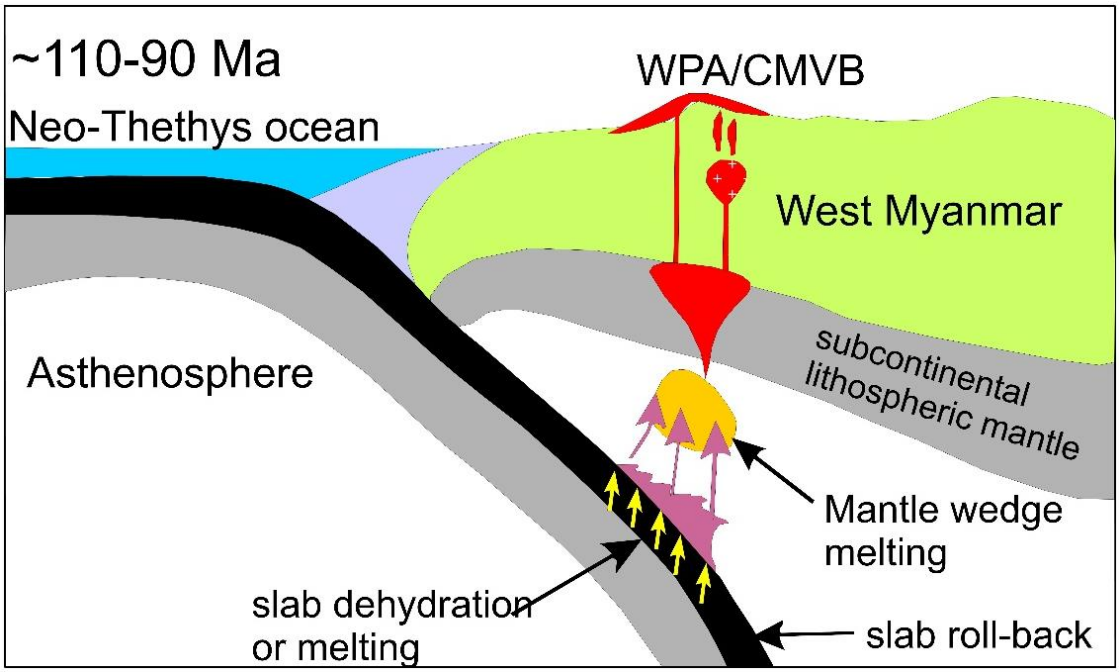

Figure 2.1 Tectonic reconstruction of SE Asian at Cretaceous (~ 110– 90 Ma), showing formation of an extensive Neo-Tethyan magmatic arc (a; modified from Metcalfe 2013; Li et al. 2016; Xie et al. 2016, Li et al. 2020). WPA: Wuntho Popa Arc, CMVB: Central Magmatic Volcanic Belt.

2.2 Tectonic Setting

Myanmar can be separated into four major geological provinces:(1) the Indo-Burman Ranges, (2) the Wuntho-Popa Arc (comprising subduction-related granites with associated porphyry-type Cu-Au and epithermal gold mineralization including the Monywa deposit), (3) the Mogok-Mandalay-Mergui Belt (hosting both significant tin-tungsten mineralization associated with crustal melt granites including the Mawchi deposit, and major orogenic gold resources), (4) the Shan Plateau (massive sulfide-type-lead-zinc including the Bawdwin deposit) (Gardiner et al, 2016). The 1500 km-long arcuate N-S Central Volcanic Belt or Central Volcanic Magmatic Belt formed as a magmatic-volcanic arc of Late Cretaceous-Tertiary age defines the Wuntho-Popa Arc (WPA) and hosts the Monywa high sulfidation Cu-Au deposit (Mitchell et al. 2011; Khin Zaw et al.2017), the Shangalon porphyry Cu-Au-Mo deposit (Hammarstrom et al. 2013; Khin Zaw et al. 2017) and a variety of epithermal to mesothermal-type gold-silver veins

(e.g. the Kyaukpahto deposit). The WPA is a continental magmatic arc (Mitchell and McKerrow, 1975; United Nations Development Programme (UNDP), 1978), and comprises major Cretaceous-Eocene granodiorite intrusions with related volcanic rocks and middle Miocene rhyolites and dacites, principally outcropping in Mount Popa and outliers to the south (Barley et al., 2003; Khin Zaw, 1990; Mitchell and McKerrow, 1975; Mitchell et al., 2012).

In the early 1970s, the Wuntho-Popa Arc was recognized as a volcanic setting (United Nations, 1978), leading to a review of the possibility of epithermal and porphyry-type mineralization. The Wuntho-Popa Arc contains four main segments, (1) Kawt-a-Bum-Mt. Loimye Segment, (2) Wuntho-Banmauk Segment, (3) Monwya-Salingyi Segment, (4) Mt. Popa segment. The Wuntho-Popa Arc also contains three distinct Pliocene-Quaternary stratovolcanoes occur within the magmatic arc: Mt. Popa, Taungthonlone and Mt. Loimye (Stephenson and Marshall, 1984, Mitchell, 2017).

2.2.1 Kawt-a-Bum-Mt Loimye Segment

There are five volcanoes in the magmatic arc including Mt. Loimye, Taung Thonelone, Singu, Monywa and Popa from north to south (Bender, 1983; Searle et al., 2007). Three of the volcanic centers, i.e., Monywa, Mt. Popa and Singu, are located in the central part of the Wuntho Popa Magmatic, whereas the Taung Thonlone and Loimye volcano are at the northern part of the Central Volcanic Belt. The Taung Thonlone volcano is located at just few kilometers north of the study area but the age of volcanism is not known.

In the Kawt-a-Bum-Mt Loimye Segment, diorites intruded into the mica schists, graphite mica schist, quartzite and minor garnet mica schist. The schists are bounded in the west by serpentinites, basalts, and cherts. Alluvial gold and platinum group elements (PGEs) are common but any source is not known yet (Mitchell, 2018). Nyunt Htay et al.

(2010, unpublished) considered that the numerous placer gold and PGE occurrences south and west of Kawt-a-Bum were derived from the volcanic rocks. Mt Loimye is presumed to be one of three stratovolcanoes in Myanmar but is a less prominent topographical feature than the other two, Mt Popa and Taungthonlon. Tatlet Au-working site lies within the Jade Mines-Loimaw Uplift, where this is overprinted by the projected magmatic arc axis between Mt Loimye and Kanzachaung Batholith to the southwest.

2.2.2 Wuntho-Banmauk Segment

The two principal inliers are the northerly 160 km-long Wuntho-Banmauk Segments, and the Monywa-Salingyi Segment in central-south Myanmar. The Wuntho-Popa Arc is underlain by the Burma Seismic Zone, and the observed calc-alkaline magmatism is suggestive of an Andean-type setting. Wuntho-Banmauk Segment is larger than the other segments in the Wuntho-Popa Arc. Major towns are Wuntho and Banmauk east of the batholith and Pinhinga Complex, and Pinlebu to the west. The name Wuntho-Banmauk or Pinlebue Banmauk is sometimes applied to the entire Popa-Loimye Arc. Noetling (1894, 1907 in Brown, 1935) undertook widely spaced traverses on the eastern side of the arc between Kawlin and Banmauk and described a granitic to quartz dioritic core to the Mingin Range bordered by andesitic volcanic ash with quartz and feldspar, which he considered to be Cenozoic in age. Small areas of gneiss, mica schist, and amphibolite mostly occurring as roof pendants in adamellite or diorite are widely distributed around Banmauk. Historically, most Au production in the region has been from Late Cretaceous high-grade auriferous veins found both in granodiorite and surrounding host rocks, and from derived placers in the Wuntho region (Chhibber, 1934).

The Wuntho-Banmauk Segment of the arc contains numerous low sulfidation or quartz-adularia vein type prospects and workings, most of which are hosted in the basaltic and andesitic Mawgyi Volcanics. Most are the relatively accessible eastern side of the

Kanzachaung batholith. Gold-silver tellurides are much more abundant than native gold and associated with pyrite, chalcopyrite, sphalerite, galena, and a trace of base metal tellurides. Vein textures and the presence of tellurides indicate that the Kyaukpazat deposit is a low sulfidation epithermal deposit. Porphyry Cu–Au prospects have been recognized at Shangalon near Wuntho (United Nations, 1996; Mitchell et al., 2011). Low sulfidation epithermal Au quartz veins are also reported from south of Shangalon (United Nations, 1996). Since the early 1970′s, the Shangalon area has been recognized as a potential area for porphyry Cu–Au systems, and somewhat later, the Kyungalon area was recognized as a potential region for epithermal Cu-Au mineralization. Sparse geological and geochronological research shows that the mineralization at the Shangalon-Kyungalon area is Eocene, older than the Miocene Monywa copper deposit (United Nations, 1978b; Mitchell et al., 2011; Gardiner et al., 2016a).

In the Monywa and Banmauk areas the magmatic arc and its metamorphic basement forms a chain of inliers within Late Cenozoic sediments (Mitchell et al. 1999; Myint Soe et al. 2017). The basement rocks were intruded by granodioritic and dioritic plutons and batholiths. The larger intrusions in the Banmauk area have yielded K–Ar ages of 93.7 ± 3.4 and 97.8 ± 3.6 Ma (United Nations 1978a), and Barley et al. (2003) reported a SHRIMP age of 94 Ma for the Kanzachaung Batholith in the Kawlin-Wutho area in northern Myanmar west of the Sagaing Fault. In the Wuntho–Banmauk area, gold-sulfide-bearing quartz ± carbonate veins are crustiform-colloform and hosted by granodioritic to dioritic plutons, basaltic andesite and associated amphibolite and chlorite schist. These veins appear to have telescoped on an earlier porphyry system. In the Kyaukpazat deposit, gold mineralization is confined mainly to NNW–SSE- and nearly east–west-trending gold-sulfide-bearing quartz ± carbonate veins and in highly sheared Mawgyi Andesite and associated chlorite schists of the Shwedaung Formation. Recently skarn-type Au-sulfides ores have also been noted in the Kyaukpazat area. Microscopic and SEM-EDS

studies reveal that t ores from the Kyaukpazat deposit have a complex mineralogy of native gold and gold–silver tellurides associated with pyrite, chalcopyrite, sphalerite, galena and trace amounts of tellurides. Most important gold deposits in Kawlin-Wuntho-Banmauk area and comparison of Thone Myae Song deposit are described in Table 2.1.

Native gold occurs as free, coarse grains in a matrix of quartz, or locked in grain boundaries of sulfides and fine native gold particles, encapsulated in pyrite. Microscopically, gold–silver tellurides (petzite, calaverite and sylvanite) are much more abundant than native gold in these ores, and so the gold contained in gold-bearing tellurides is considered to be a significant proportion of the total gold budget in the Kyaukpazat deposit. The porphyry copper ± gold ± molybdenum mineralization in the Shangalon area, 25 km SW of Kawlin, occurs in diorite and quartz diorite. It is related to the intrusion of tonalite dykes and is closely associated with granodiorite. Mitchell (1993) reported a K–Ar age of 52.9 ± 2.3 Ma for a quartz diorite at the Shangalon porphyry cu deposit, dated by the United Nations (1978a). Barley et al. (2003) also recorded a SHRIMP age of 38 Ma for the intrusive rock at Shangalon. Most mineralization at Shangalon is in quartz sulfide veins as disseminations of chalcopyrite and pyrite with low gold values. Detailed descriptions of significant deposits/prospects or occurrences from the north to the south along the Central magmatic arc.

Table 2.1 Comparison of most important gold deposits in Wuntho-Banmauk Segment, Northern Myanmar.

No	Deposit	Location (N, E)	Deposit Type	Host Rocks/(Ages)	Intrusions/(Ages)	Ore Mineralogy	Alteration	References
1	Shangalon	Map 84M/10 23° 43′ 06″, 95° 30′ 55″	Porphyry-Epithermal deposit	Diorite and quartz diorite	Granodiorite (K-Ar age 93.7 ± 3.4, 97.8 ± 3.6 Ma; U-Pb age 94,6 ± 1 Ma, 98.1 ± 0.47, 102.1 ± 0.95 Ma); Diorite (U-Pb 36.9 ± 0.26 Ma to 38.0 ± 0.35 Ma); One gabbro has a zircon age of 106.7 ± 0.6 Ma, four granites, one granodiorite, and two diorites Cretaceous zircon ages ~ 99 Ma to ~ 90 Ma	Chalcopyrite, minor chalcocite, molybdenite, covellite,	Strong silicification, advanced argillic alteration	UNDP (1978, 1979), Gardiner et al. (2016), Khin Zaw (2017), Khin Zaw et al. (2017), Thiri Ye Htut et al. (2020), Jin-Xiang Li et al. (2020)
2	Kyauk-pahto mine	Map 84M/13 23° 48′, 95° 57′	Sedimentary rock hosted gold deposit	Sandstone, siltstone (Eocene) (U–Pb youngest detrital zircon age 48.7 ± 0.7 Ma)	No known intrusion	Pyrite, galena, sphalerite, electrum, chalcopyrite, arsenopyrite	Silicification, sericitization, argillic alteration, decalcification	Khin Zaw (2008), Ye Myint Swe et al. (2017)
3	Mahar San	23′ 48′ 5″, 95′ 33′ 33″	VHMS	Hosted in a complex sequence of intermediate volcanic and volcaniclastic rocks of probable Miocene age	Miocene	Pyrite, chalcopyrite, chalcocite with galena, sphalerite, covellite, bornite, tennantite	Chlorite-sericite alteration with carbonate and quartz veining	Khin Zaw (2017), Khin Zaw et al. (2017)
4	Kyaukpazat	Map 83P/16 24° 05′ 02″, 95° 50′ 45″	Orogenic gold deposit	Andesite (Mawgyi andesite)	Granodiorite and dioritic plutons of Mid-Cretaceous–Eocene age	Pyrite, chalcopyrite, sphalerite, galena, altaite, calaverite, petzite, native Au, tellurobismuthite, Hematite,	Silicification, sericitization, chloritization	Ye Myint Swe et al. (2017)
5	Thone Myae Song (EE3 Prospect)	Map 83P/16 24° 10′ 0″, 95° 52′ 40″	Epithermal deposit	Andesite (Mawgyi andesite)	No data for Mawgyi Andesite; Cretaceous 98.1 ± 0.47 Ma for Banmauk granodiorite	Pyrite, chalcopyrite, sphalerite, petzite, native Au, tellurobismuthite, calaverite, magnetite, electrum	sericitization, chloritization, epidotization, carbonization	This study Gardiner et al. (2016, 2018)

2.2.3 Monywa-Salingyi Segment

The 45-km-long Monywa-Salingyi Segment is situated on the west bank of the Chindwin river opposite the town of Monywa, some 150 km south-southwest of the Kanzachaung Batholith. The uplift, also known as the Lower Chindwin Volcanic Field or igneous district of Chhibber (1934a), trends north-northwest and lies within a regional geanticline between the Chindwin and Shwebo Basins. Similar basalts with numerous microdiorite intrusions occupy much of the Salingyi Inlier. The lavas are pervasively altered to chlorite epidote rocks in which the flow morphology is well preserved and are interbedded with fine-grained volcaniclastic sediments.

The basalts are equivalent to those in the Mawgyi Volcanics widespread in the Wuntho-Banmauk Segment to the north. Diorites, hornblende gabbros and granites intrude the oceanic basalt at Salingyi where the largest diorite body is 7 km in length. Silicic epidote-bearing dyke-like intrusions, the keratophyres of Barber (1936) and the quartz keratophyres and epidosites of UN-DGSE (1979c), cut the basalt and hornblende gabbros at Salingyi. Similarities to the oceanic basalt at Salingyi and Monywa and the basalt in the Mawgyi Volcanics in the Wuntho- Banmauk Segment suggest a similar pre-mid Cretaceous age for the Taungni Basalt. There are four deposits, of which three, Sabetaung, Sabetaung South, and Kyisintaung, are contiguous, while Letpadaung lies 7 km to the southeast. Kyisintaung is a prominent hill and Letpadaung, rising to 250 m above the Chindwin floodplain, dominates the landscape and contains 70% of the total copper resource at Monywa.

The Mesozoic inliers are only exposed within the Wuntho-Bamauk and Monywa-Salingyi Segments, consisting of early Upper Cretaceous granitoid plutons, intruded into pre-existent basalts and pillow lavas (United Nations, 1978a, and reference therein). While not readily available in the geoscience literature, the regional stratigraphy of Wuntho-Banmauk is described in United Nations (1978a, b), and comprises both older (Kanzachaung batholith; 110–90 Ma) and younger intrusive-volcanic complexes (Shangalon-Kyungalon ore district; 40–33 Ma).

2.2.4 Mount Popa Segment

This forms the southernmost visible segment of the magmatic arc and situate 60 km south of Shinmataung on the northwestern margin of the Pegu Yoma Range. Above this the conical Mt Popa volcano (1518 m) consists of basalt, basaltic andesite, and pyroclastics, with two andesitic plugs. It has a deep central crater with a breach through which extensive lavas have flowed to the north. Lee et al. (2016) conclude that the mid-

Miocene rocks at Mt Popa and Monywa show typical arc lava characteristics and reflect partial melting of a juvenile mantle wedge related to subduction of Indian Ocean lithosphere. At Taungnauk, Taungni, and the Kyaukpadaung Range the quartz-pyrite alteration or lithocap can be explained by condensation of ascending magmatic SO_2 gas in meteoric water at depths of less than about 1.5 km beneath an eroded and now vanished stratovolcano (Mitchell, 2018).

The epithermal veins, while not necessarily including a direct input of magmatic fluid, required a heat source at depth, inferred to be Miocene intrusions uplifted much less than those in the Mt Popa area to the north. At the Monywa copper mine, near Monywa within the Wuntho-Popa Arc in central-western Myanmar, high sulfidation epithermal mineralization is inferred to be underlain by a mid-Miocene pluton (Mitchell et al., 2011). The main hypogene ore minerals found at Monywa are digenite-chalcocite, covellite and minor enargite, typical of high-sulfidation epithermal deposits, Monywa differs from many other high sulfidation deposits in the absence of associated economic Au grades, and in the scarcity of large bodies of replacement quartz (Mitchell, 2018).

This lack of Au is thought to be the result of exposure of a deep epithermal system in which hypogene Cu minerals were not necessarily overlain by Au mineralization (Kyaw Win and Kirwin, 1998). The calc-alkaline to potassic calc-alkaline rocks in Mt. Popa are considered to be a continuation of the Sunda-Andaman Arc in the north (Maury et al., 2004). The Monywa and Mt. Popa areas also display arc-like geochemical signatures indicating a metasomatized mantle origin (Lee et al., 2016).

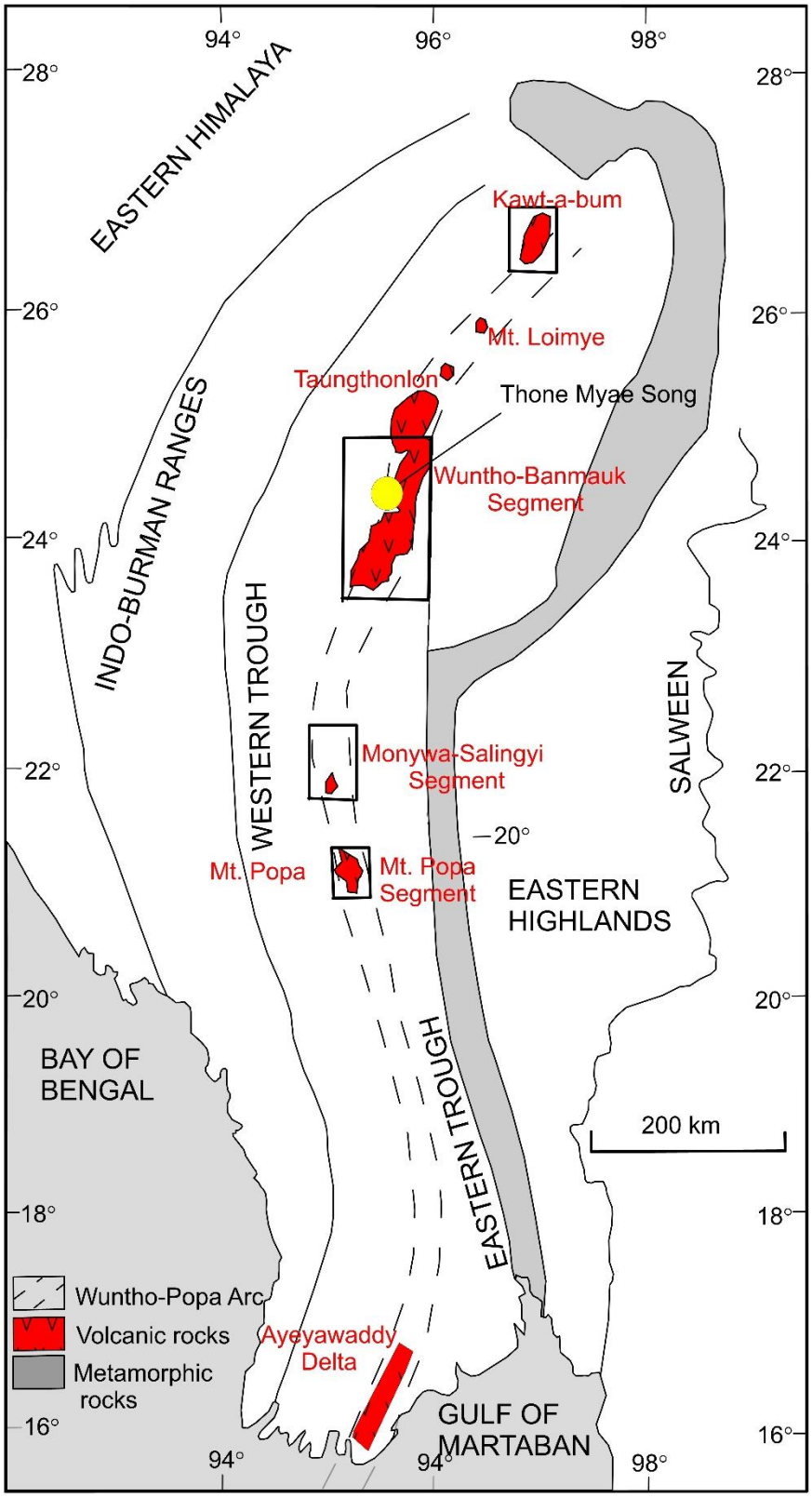

Figure 2.2 Wuntho-Popa Arc with intrusive and eruptive rocks in red and main 4 arc segments (Kawt-a-Bum-Mt Loimye Segment, Wuntho-Banmauk Segment, Monywa-Salingyi Segment, and Mt. Popa Segment) emphasized by squares. The study area is at the yellow point (modified from Mitchell, 2018).

2.3 Regional Structures

The area was also subjected to compressional deformation in the middle to late Miocene, following the development of a spreading centre in the Andaman Sea and the initiation of the Sagaing Fault. This has resulted in open folding of the Male Formation sediments and the formation of the regional-scale dome which exposed the magmatic arc rocks of the Wuntho Massif. In the southern part of the study area, the fault zone comprises two main strands, an eastern fault along the course of the Irrawaddy River (the Sagaing Fault) and a western one (the Kyauktan Fault) near the western licence boundary.

The regional geological structures of the study area are very complex as it lies between Kabaw Thrust and Sagaing Fault. The major trends are nearly N-S and the minor faults trend NE-SW. The Shwedaung Formation is the most extremely deformed unit in this area, showing constricted small-scale folds. The characteristic of Mawgyi Andesite is lack of bedding and structure also very rare. Major N-S trending faults are formed in the eastern part of the study area. The Nankan-Banmauk valley is a fault trough controlled by two major faults, the Taungchaung Fault on the east and the Chutkon-Legyin Fault on the west. In the north, Taungchaung Fault is exposed and downthrows on the west and forms the boundary of the Bongyaung Range and Nankan-Banmauk valley.

The Chutkon-Legyin Fault forms the boundary of the Shwedaung Formation, Mawgyi Andesite and Peinnegon Adamellite. The NE-trending faults control mineralization at Lemi and Patun Hmawgyi Au prospects (Zaw Lin Aung, 2011). In the Shangalon area the Shangalon Fault is mineralized along its entire length, at Shanglon, Wagauktaw, Letpangyin and Kyaukkyan Taung, associated with intrusions of quartz diorite, tonalite and diorite. The gold deposits are related by fault system. Mineralizations of Banmauk area generally occur as N-S, NNW-SSE and E-W trend (Thiha Soe, 2011).

2.4 Conclusions

The study area is situated in the eastern Tertiary sedimentary basin of Myanmar, straddling the Sagaing Fault zone, a continental-scale right-lateral transform fault which marks the boundary between the West Burma continental plate in the west and the Shan-Thai (or Sibumasu) continental plate in the east. The Thone Myae Song gold deposit is also located in the Central Magmatic Volcanic Belt or Wuntho-Popa Arc in the northern part of Myanmar. Wuntho-Banmauk Segment has a variety of styles of copper-gold deposits including high sulfidation Cu-Au-Mo porphyry (e.g., Shangalon), mesothermal Au (Kyaukpazat), polymetallic VHMS (e.g., Mahar San) and epithermal Au deposit (e.g., EE3 Prospect).

2.5 References

Barley, M.E., Khin Zaw, Pickard, A.L., Pak, P., Doyle, M.G., 2003. Jurassic to Miocene magmatism and metamorphism in the Mogok Metamorphic Belt: implications for the India–Eurasia collision in Myanmar. Tectonics 22, 1019–1030. https://doi.org/10.1029/2002TC001398.

Barber, C.T., 1936. The Tertiary igneous rocks of the Pakokku district and the Salingyi town- ship of the lower Chindwin district, Burma, with special reference to the determination of the felspars by the Federoff Method. Memoir of the Geological Survey of India 68 (2), 121-292.

Brown, J.C., 1935. Gold in Burma and the Shan States. Mining Magazine 52, 9-20, 82-92.

Cai FL, Ding L, Yao W, Laskowski AK, Xu Q, Zhang J, Sein KI . 2017. Provenance and tectonic evolution of Lower Paleozoic-Upper Mesozoic strata from Sibumasu terrane, Myanmar. Gondwana Res 41:325–336

Chibber, H.L., 1934a. The Geology of Burma, London, Mac Millan, 538p.

Chibber, H.L., 1934b. The Mineral Resources of Burma, London, Mac Millan, 520p.

Gardiner, N.J., Robb, L.J., Morley, C.K., Searle, M.P., Cawood, P.A., Whitehouse, M.J., Kirkland, C.L., Roberts, N.M.W., Tin Aung Myint., 2016. The tectonic and metallogenic framework of Myanmar: a Tethyan mineral system. Ore Geol. Rev. 79, 26–45.

Gardiner, N. J., Hawkesworth, C. J., Robb, L. J., Whitehouse, M. J., Roberts, N. M., Kirkland, C. L., Evans, N. J., 2017. Contrasting granite metal-logeny through the zircon record: A case study from Myanmar. Scientific reports 7:748.

Gardiner, N. J., Searle, M. P., Morley, C. K., Robb, L. J., Whitehouse, M. J., Roberts, N. M. W., Kirkland, C. L., Spencer, C. J., 2018. The crustal architecture of Myanmar imaged through zircon U–Pb, Lu–Hf and O isotopes: tectonic and metallogenic implications. Gond- wana Res 62:27–60

Hammarstrom, J.M., Bookstrom, A.A. et al. 2013. Porphyry Copper Assessment of Southeast Asia and Melanesia. US Geological Survey, Scientific Investigations Report 2010-5090-D.

Khin Zaw., 1990. Geological, petrological and geochemical characteristics of granitoid rocks in Burma: With special reference to the associated W-Sn mineralization and their tectonic setting. J. SE Asian Earth Sci. 4, 293-335. https://doi.org/10.1016/0743-9547(90)90004-W.

Khin Zaw, 2008. Origin of sedimentary rock-hosted gold deposit at Kyaukpahto, Kawlin–Wuntho District, Northern Myanmar. Proceedings of PACRIM Congress 2008, Australian Institute of Mining and Metallurgy, 24–26 November 2008, Gold Coast, Australia. 457–464.

Khin Zaw., 2017. Overview of mineralization styles and tectonic—metallogenic setting in Myanmar. In: Barber, A.J., Khin Zaw. Crow, M.J., Eds., Myanmar: Geology,

Resources and Tectonics, Geological Society (London) Memoir, J. Geol. Soc. London. 48, 531-556. https://doi.org/10.1144/M48.24.

KyawWin, Kirwin, D., 1998. Exploration, geology, and mineralization of the Monywa copper deposits, central Myanmar. In: Porphyry and Hydrothermal Copper and Gold Deposits: A Global Perspective. Proceedings of the Australian Mineral Foundation Conference, Perth, Australia, pp. 61-74.

Lee, H.-Y., Chung, S.-L., Yang, H.-M., 2016. Late Cenozoic volcanism in central Myanmar: geochemical characteristics and geodynamic significance. Lithos 245, 174-190.

Li, J.X., Fan, W.M., Zhang, L.Y., Peng, T.P., Sun, Y.L., Ding, L., Cai, F.L., Sein, K., 2020. Prolonged Neo-Tethyan magmatic arc in Myanmar: Evidence from geochemistry and Sr-Nd-Hf isotopes of Cretaceous mafic-felsic intrusions in the Banmauk-Kawlin area. Int. J. Earth Sci. 109, 649–668.

Metcalfe. I., 2013. Gondwana dispersion and Asian accretion: Tectonic and palaeogeographic evolution of eastern Tethys. J Asian Earth Sci 66:1–33.

Mitchell, A.H.G., McKerrow, W.S., 1975. Analogous evolution of the Burma orogen and the Scottish Caledonides. Geological Society of America Bulletin 86, 305-315.

Mitchell, A.H.G., 1993. Cretaceous-Cenozoic tectonic events in the western Myanmar (Burma)-Assan region. J. Geol. Soc. London, 150, 108-122.

Mitchell, A.H.G., Htay, N., Ausa, C., Deiparine, L., Khine, A. and Po, S., 1999. Geological settings of gold districts in Myanmar. Proceedings International Congress on Earth Science, Exploration and Mining around the Pacific Rim, Australasian Institute of Mining and Metallurgy, Bali, 10-13 October 1999, 303-309.

Mitchell, A.H.G., Win Myint, Kyi Lynn, Myint Thein Htay, Maw Oo, Thein Zaw, 2011. Geology of the high sulphidation copper deposits, Monywa mine, Myanmar. Resource Geology 61, 1-29.

Mitchell, A.H.G., Chung, S.-L., Thura Oo, Lin, T.-H. and Hung, C.-H., 2012. Zircon U-Pb ages in Myanmar: Magmatic-metamorphic events and the closure of a neo-Tethys ocean? J. Asian Earth Sci. 56, 1-23.

Mitchell, A.H.G., 2017. Geological Belts, Plate Boundaries, and Mineral Deposits in Myanmar. Elsevier, 524p.

Mitchell, A.H.G., 2018. Geological Belts, Plate Boundaries, and Mineral Deposits in Myanmar. Elsevier, Amsterdam, 509p. https://doi.org/10.1016/B978-0-12-803382-1.01001-4.

Myint, S., Takashima, I., Zaw, K., Swe, Y.M., 2017. Remote sensing and GIS studies of alteration and predictive mineral exploration in the Central Volcanic Arc, Myanmar. Geological Society (London). Memoirs, 48, 473-496, https://doi.org/ 10.1144/M48.22.

Noetling, F., 1894. Note on the geology of Wuntho in Upper Burma. Rec Geol. Survey India 27.4.115.124.

Stephenson, D., Marshall, T.R., 1984. The petrology and mineralogy of Mt Popa Volcano and the nature of the late-Cenozoic Burma Volcanic Arc. J. Geol. Soc (London) 141, 747-762.

Thiha Soe, 2011, Geological and Geochemical Characteristics of Gold Mineralization at Mutthein – Hechein – Le U Area, Banmauk (Unpublished Thesis).pages

Thiri Ye Htut, Qin, K., Li, G., Sein, K., Evans, N.J., 2020. Eocene arc magmatism and related Cu-Au (Mo) mineralization in the Shangalon-Kyungalon district, Wuntho-Popa Arc, northern Myanmar. Ore Geol. Rev. 125, https://doi.org/10.1016/j.oregeorev.2020.103678.

United Nations., 1978. Geology and Exploration Geochemistry of the Pinlebu-Banmauk area, Sagaing Division, Northern Burma, Technical Report No. 2, Geological

Survey and Exploration Project, United Nations Development Programme, United Nations, New York, 1-53.

UNDGSE, 1979c. Geology and Exploration Geochemistry of the Salingyi-Shinmataung area, Central Burma. Technical Report No. 5. United Nations Development Programme, UN/ BUR-72-002, United Nations, New York, 38 p.

Ye Myint Swe, Cho Cho Aye, Khin Zaw., 2017. Gold Deposits of Myanmar. In: Barber, A.J., Zaw, K. and Crow, M.J., Eds., Myanmar: Geology, Resources and Tectonics, the Geological Society (London) Memoir, J. Geol. Soc. (London). 48, 557-572. https://doi.org/10.1144/M48.25.

Zaw Linn Aung, 2011, Controls on Gold-copper Mineralization in Patun Area, Banmauk Township, Sagaing Region. Ph. D Dissertation, University of Yangon, Unpublished.

Zhang, J. E., Xiao, W. J., Windley, B., Cai, F. L., Sein, K., Naing, S, 2017a. Early Cretaceous wedge extrusion in the Indo-Burma Range accretionary complex: implications for the Mesozoic subduction of Neo-tethys in SE Asia. Int J Earth Sci 106:1391–1408.

Zhang, J.E., Xiao, W., Windley, B. F., Wakabayashi, J., Cai, F., Sein, K., Wu, H., Naing, S., 2018. Multiple alternating forearc- and backarc-ward migration of magmatism in the Indo-Myanmar Orogenic Belt since the Jurassic: Documentation of the orogenic architecture of eastern Neotethys in SE Asia. Earth Sci Rev 185:704–731

CHAPTER 3

REGIONAL AND DEPOSIT GEOLOGY OF THE THONE MYAE SONG AREA

3.1 Introduction

This chapter includes a review of the Central Volcanic Line relate Banmauk gold district. It discusses deposit geology and classification of the host rocks.

3.2 Regional Geology

The geological map of the Banmauk district is shown in Figure 3.1. The Banmauk district lies in the northeastern part of the Wuntho Massif and it is located at the northern segment of Central Magmatic-Volcanic Belt or so called Central Volcanic (Igneous) Line (CVL) (Barber et al., 2017; Khin Zaw, 2017; Mitchell, 2017). The Wuntho Massif is composed of intermediate to felsic igneous rocks and bordered in the west by the Chindwin Basin and in the east by a 1500 km long N-S trending right lateral strike slip fault called the Sagaing Fault. The Wuntho Massif includes granodiorite of batholithic dimension and occurs as an elongated body trending generally NNE-SSW.

This area is traditionally known in ancient time as the Maingthon Hill Tract (Noetling, 1894) and then later named as the Wuntho Igneous Complex (Chhibber, 1934a). This complex has several igneous rock types and older metamorphic rocks and is encircled by the older and younger Tertiary sedimentary rocks. The CVL passes through this igneous complex (Chhibber, 1934a). Along the CVL, Miocene to Quaternary volcanic rocks are also exposed including tufaceous sedimentary rocks, ashes and breccia, dolerite sills and rhyolites (United Nations, 1978). The main volcanic rocks of the Wuntho Massif are Mawgyi Andesite unit (basaltic andesite, andesite, pillow lava), Kanza Chaung

Batholith (hornblende granodiorite, biotite hornblende granodiorite and diorite) and Pinhinga Plutonic Complex (Mitchell, 1981).

The regional geology of the Wuntho area by Department of Geological Survey and Exploration (D.G.S.E) (1976) is as follows: the metamorphic rocks and pre-batholithic stratigraphic units comprise possibly pre-Triassic basement the Hpyu Taung Metamorphic rock (schist and schistose quartzites), Upper Triassic Shwedaung Formation (laminated cherty, tuffaceous sedimentary rock, micritic limestone, tremolite schist and andesite), Lower Cretaceous Mawgyi Andesite (dark green andesite or flow breccia, interbedded with the massive andesite) and Lower Cretaceous Kondanchaung Group of sedimentary rocks. The plutonic rocks of mafic, intermediate and felsic compositions occupy nearly a quarter of the whole region. The plutonic rocks consist largely of granodiorite, diorite and quartz diorite, adamellite with subordinate amounts of gabbro, dolerite and micro-leucocratic rocks. The regional geological structure of the study area is very complex as the area lies between the Kabaw Thrust and the Sagaing Fault. The major structural trend is N-S superimposed by several faults trending NE-SW. Movement and deformation along the N-S trending Sagaing Fault also affected the later stage of mineralization as evidenced by later stage network of quartz veins which are aligned along the N-S trending faults.

The large Kanza Chaung Granodiorite in the Banmauk district yielded K-Ar ages of 93.7±3.4 and 97.8±3.6 Ma (United Nations, 1978). A SHRIMP U-Pb zircon age of the Kanza Chaung Granitoid yielded 94.6 ± 1.0 Ma (Barley et al., 2003). At the Shangalon copper-molybdenum-gold deposit, Barley et al. (2003) recorded a SHRIMP U–Pb age of zircon 38.5 ± 0.6 Ma for the Shangalon Granodiorite Porphyry. Gardiner et al. (2016, 2018) reported ages of 98.1 ± 0.47 Ma for Banmauk Granodiorite (24° 24′ 46″ N/95°45′35″ E) and 102.1 ± 0.95 Ma for the Wuntho Granitoid (24° 00′ 12″ N/95° 27′ 56″ E) and 40.0 ± 0.2 Ma for the Shangalon Diorite using U–Pb geochronology on zircon. Li

et al. (2013) indicated a U-Pb zircon age of 102 ± 0.8 Ma for a granite from south of the Kawlin-Wuntho area. Recently Li et al. (2020) reported additional zircon ages from ten intermediate–felsic intrusions (five granites, one diorite, and four granodiorites) from the Kawlin area and they recorded Cretaceous ages of ~ 104–101 Ma and ~ 94 Ma. Thiri Ye Htut et al. (2020) also recently undertook U-Pb dating on zircon of the Shangalon-Kyungalon porphyry and epithermal type deposit, 55km southwest of the EE3 Prospect area. They yielded Eocene age of 38.0 ± 0.35 Ma on gabbroic diorite, 37.8 ± 0.35 Ma on diorite porphyry, 37.4 ± 0.27 Ma on tonalite porphyry, and 36.9 ± 0.26 Ma on granodiorite.

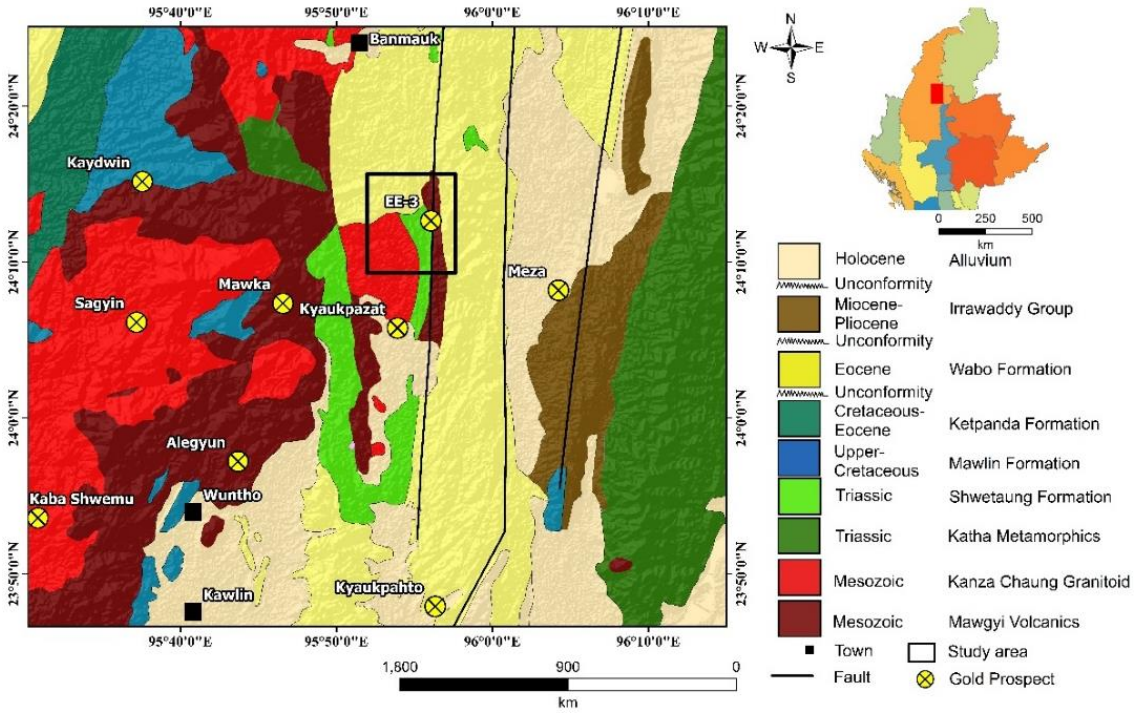

Figure 3.1 Regional geological map of the Banmauk area (modified after UNDP, 1978, 1979; Mitchell 2018).

3.3 Deposit Geology

The Thone Myae Song deposit consists of three orebodies which have been mined (Figure 3.2). The orebodies at the EE3, Myauk Let Sho, Thapan Aing Prospects occurred as main mineralized zones. This study focuses on the EE3 orebody of the Thone Myae

Song deposit in the Banmauk district. Gold mineralization in the Thone Myae Song deposit occurred as massive veins, stockworks and disseminations. The general orientation of quartz veins is N-S. The study area is mainly composed of volcanic rock unit, locally called Mawgyi Andesite (Cretaceous), phyllite and mudstone of Shwedaung Formation (Upper Triassic), sandstone of Wabochaung Formation (Miocene) and granodiorite (Mesozoic and Paleogene).

The Mawgyi Andesite unit is the most widespread unit of volcanic rocks in the study area. According to United Nations (1978), this formation consists of a succession up to 2000m thick volcanic and volcanoclastic rocks with minor sedimentary units. It is composed of andesitic clastic rocks and basaltic andesite. It is poorly exposed and is widely covered by residual soil and if exposed, it is massive in nature. The majority of mineralized quartz veins are hosted by this andesitic rock. Granodiorite is mainly found in the western part of the study area near the Mankhin Village. It is reddish brown or dark grey on weathered surface and whitish grey and yellowish grey on fresh surface. The granodiorite body has been deeply weathered in some localities. Mottled mudstones in the area are interbedded with siltstones, sandstones and gritty to cobbly sandstones but lacking tuffaceous rocks. The gritty to cobbly sandstones contain fragments of andesite, dacite, granodiorite and vein quartz. The granodiorite body has been described as the Cretaceous Kanza Chaung Batholith.

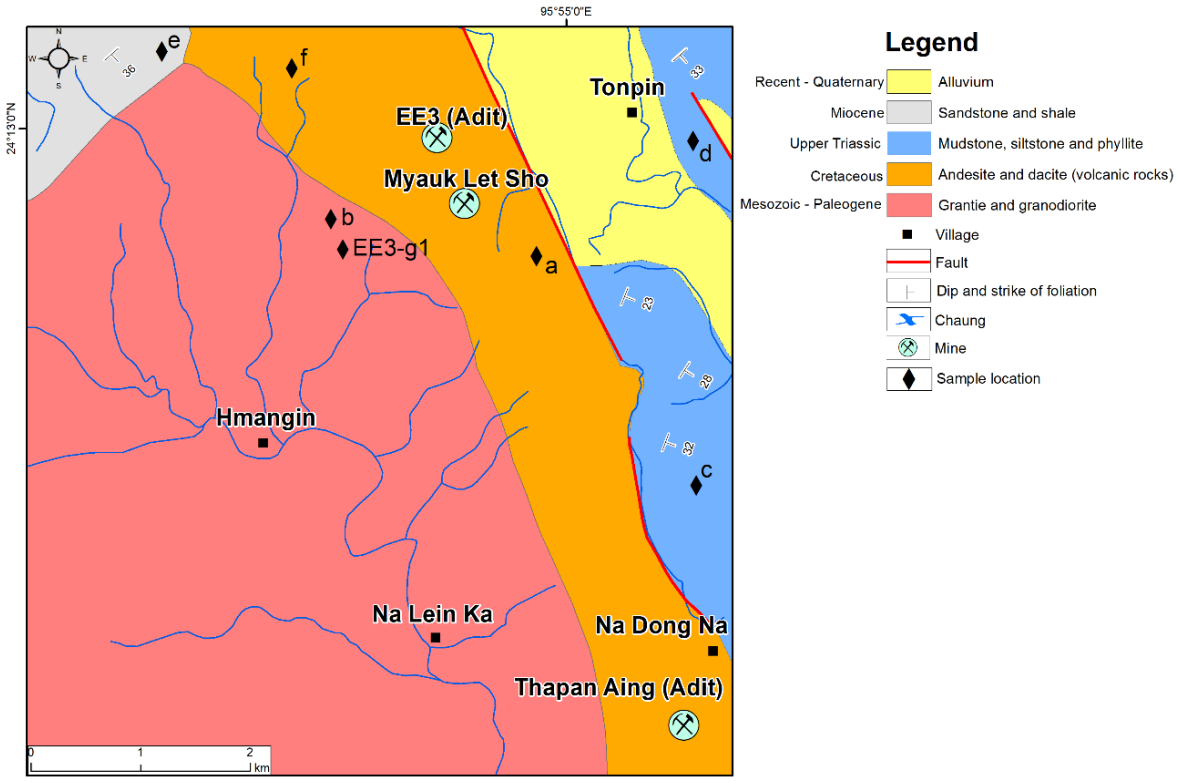

Figure 3.2 Geological map of the Thone Myae Song area (based on UTM 2495, 83p/16 on 1 inch to 1-mile map).

3.3.1 Description of Lithologic Units

In the study area, Mawgyi Andesite, granodiorite, phyllite, mudstone, younger alluvial and sandstone units are well exposed. The lithological characteristics of the rock units are described below.

3.3.1.1 Mawgyi Andesite

This unit is one of the most widespread volcanic units in the area. It is distributed in the northern part of the study area. It overlies the tuffaceous sedimentary rocks of Shwedaung Formation and schists. The predominant lithology is dark grey to green or black andesite volcanic clastic rock or massive, hard and compact andesite (Figure 3.3a). Mostly, this andesite is fine-grained massive hornblende andesite. Phenocrysts are mainly hornblende, augite and plagioclase. Mostly, this andesite is fine-grained dark grey to

greenish black color but massive structureless, which is more or less altered to chlorite. Opaque minerals in the altered andesite include pyrite.

3.3.1.2 Granodiorite

Granodiorite is found at the western part of the study area and near the Mankhin Village (Figure 3.3b). It is reddish brown or dark grey on weathered surface and whitish grey and yellowish grey on fresh surface. Granodiorite bodies are deeply weathered in some localities. Dark inclusions or rounded mafic enclaves are observed in the granodiorite. The inclusions are darker and finer-grained than the enclosing granodiorite or host rocks, with sharp contact. They are oval shaped, varying in size from 3 cm to 10 cm and show the parallel alignment.

3.3.1.3 Phyllite

This unit belongs to in Shwedaung Formation. The name Shwedaung Formation was applied by UNDGSE (1978a) to chlorite schists, tremolite schists, silicic tuffs, and slaty mudstones, phyllite and sandstones cropping out on the eastern side of the batholith. Phyllite is well exposed in the southeastern part of the study area. It is moderately hard and has fissile character. It shows buff color in weathered surface and grey in fresh surface. It is a low-grade metamorphic rock related to regional metamorphism. The unit is foliated, and lineation is well-developed. In the outcrop, phyllitic texture is seen which was formed by the parallel arrangement of platy minerals usually mica (Figure 3.3c).

3.3.1.4 Mudstone

This unit is one of the units of Shwedaung Formation and well exposed in the western part of the study area. It is bedded, moderately hard and compact, yellowish grey on weathered surface and light grey in fresh surface (Figure 3.3d). The rock unit strikes nearly N-S.

3.3.1.5 Sandstone

This unit belongs to in Wabo Chaung Formation. This unit was first established by D.G.S.E (1976) to describe mottled mudstones interbedded with siltstones, sandstones and gritty to cobble sandstones lacking tuffaceous rocks. The gritty to cobbly sandstones contain rocks fragments of andesite, dacite, granodiorite and vein quartz (Figure 3.3e). The formation is exposed in the northwestern parts of the study area. The predominant lithology of this formation is massive to thick cross-bedded concretionary sandstones, sandy siltstones and thin laminated mudstones.

The sandstones are friable, micaceous, yellowish-brown to green-grey and ash-white. The sandstone and siltstone are interbedded with shale and in some places associated with carbonaceous shale and coal (Figure 3.3f). The sandstones are sometimes calcareous and concretionary, and usually cross-bedded. conglomerates and boulder beds up to 10 m thick are interbedded with sandstones and gray, purple, or green shales. Myint Thein et al. (1987) correlated the Wabo Chaung with their Eocene Male Formation exposed near the Ayeyawaddy River east of Wuntho. The conglomerates are over- lain by cross-bedded felspathic and sometimes calcareous sandstones with thin conglomerates and siltstones.

3.3.1.6 Alluvium

The alluvial deposits occur especially along the banks of Taung Chaung and Man Lon Chaung in the southern parts of the study area. It consists of sands and clays. Silicification is often observed. There are paddy fields and some alluvial gold worksite are also found in these alluvials. Some of the alluvial gold workings are shown by UN-DGSE (1978a).

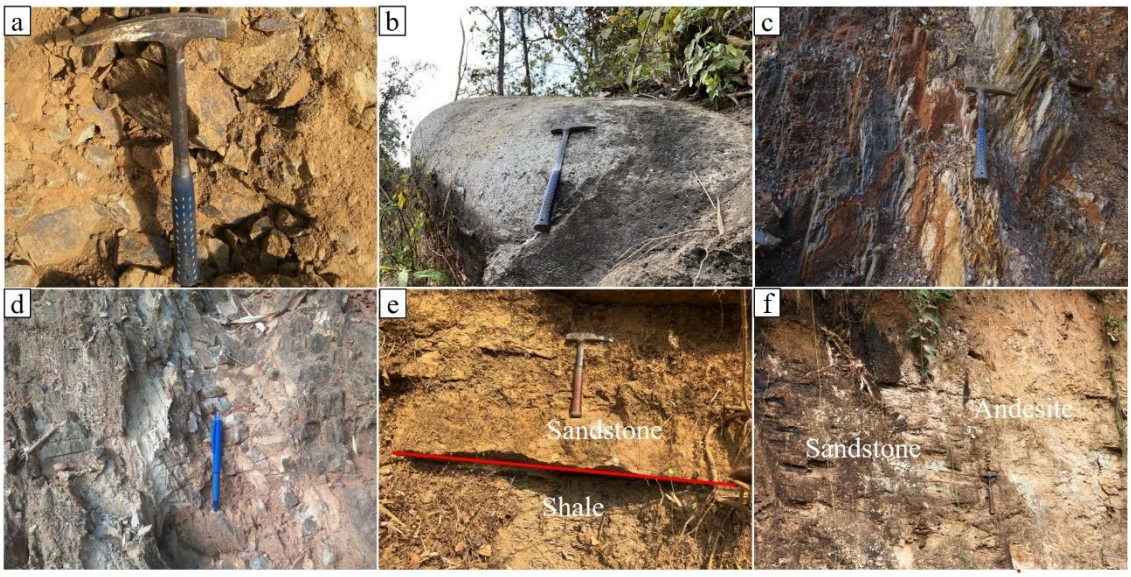

Figure 3.3 Photographs of lithologic units in the Thone Myae Song deposit area. (a) Outcorp of Mawgyi Andesite unit, (b) Outcrop of granodiorite, (c) Outcrop of phyllite, (d) Outcrop of mudstone, (e) Interbedded nature of shale and sandstone, and (f) Sandstone change to the fine andesite, and (f) Sandstone change to the fine andesite.

3.3.1.7 Petrographic and Textural Characters of Mawgyi Andesite and Granodiorite

The petrography and textural features of the Mawgyi Andesite are shown in Figure 3.4. The main constituent minerals of the Mawgyi Andesitic are plagioclase, augite, hornblende and quartz. Hornblende crystals are commonly altered to chlorite and partially to sericite, whereas plagioclase grains in the groundmass are altered to sericite (Figure 3.4a). Plagioclase phenocrysts in porphyritic andesite are altered to fine- grained sericite and pyrite are also found in the groundmass (Figure 3.4b). Plagioclase phenocrysts are often set in the groundmass with irregular boundaries.

Clinopyroxene also occurs in basaltic andesite as phenocrysts; some grains are altered to chlorite. Pyrite is noted as dissemination in the groundmass (Figure 3.4c). Quartz phenocrysts with irregular outlines are found to be associated with the pyroxene which is also present in the groundmass. Microfractures are present in some quartz

phenocrysts. The groundmass is composed of plagioclase laths and mafic minerals. Plagioclase commonly occurs as phenocrysts or laths in the groundmass (Figure 3.4d, e). Plagioclase phenocrysts in the fine-grained laths in the groundmass are altered to chlorite, epidote and calcite occurs as small veinlets (Figure 3.4f). The andesite shows ophitic texture with plagioclase phenocrysts and groundmass displaying flow structure. Quartz in the groundmass is anhedral, very fine-grained, colorless, whereas feldspars in the groundmass are fine-grained, subhedral, cloudy. Most of the ophitic plagioclase are altered to sericite.

The petrography and textural characteristics of the Kanza Chaung Granitoids are presented in Figure 3.4g, h, i. The granodiorite is mainly composed of quartz, K- feldspar, plagioclase, hornblende, biotite, opaque minerals and exhibits coarse hypidiomorphic-granular texture. Quartz is anhedral, and interstitial between other minerals, whereas K-feldspar is cloudy, subhedral to euhedral with carlsbad twining and some are altered to chlorite and illite. Myrmekitic and perthitic textures are quite common in some samples. Sometimes the intergrowth of quartz and K-feldspar show graphic texture. Plagioclase is also colorless to cloudy and subhedral with polysynthetic twining; some are altered to sericite. Offset twinning, fracturing, and brecciation of plagioclase are observed.

These features probably indicate that the rock underwent cataclastic and shear effects. Normal oscillatory zoning is mostly found in plagioclase crystals. Hornblende is greenish brown with two set of cleavages and some grains are altered to chlorite. Some smaller grains of hornblende are enclosed in larger plagioclase crystals, suggesting that the hornblende formed earlier than the plagioclase. Hornblende crystals are also found in the interstices between larger plagioclase grains. Biotite is brown to yellowish brown and one set of cleavage is distinct. Some biotite flakes are distorted and ruptured due to the deformation such as fracture, folding and faulting. It gives parallel extinction and partially altered to chlorite. The accessory minerals are sphene, magnetite, apatite, and zircon.

Magnetite, zircon, apatite, and hornblende grains are included in some plagioclase crystals.

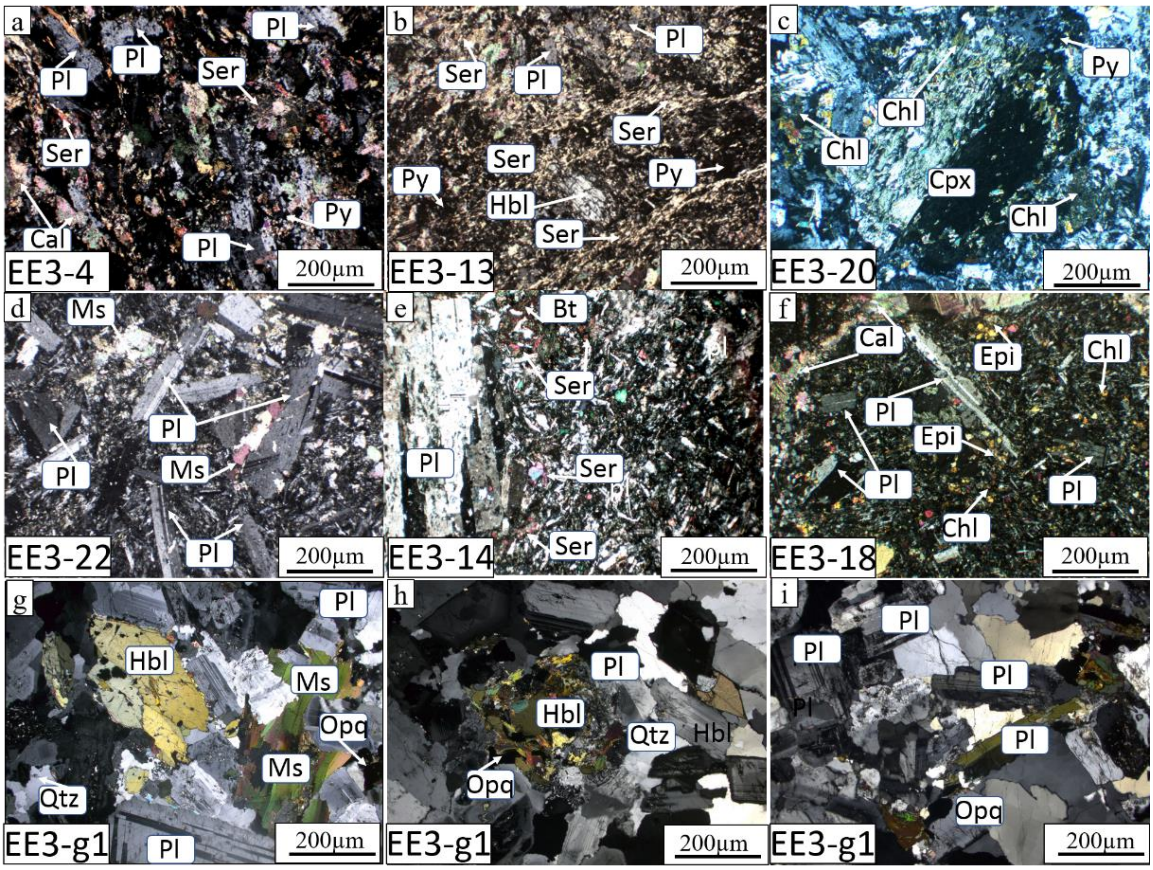

Figure 3.4 Photomicrographs showing petrographic characteristics of the andesite basalt and granodiorite in the study area. (a) Euhedral plagioclase altered to sericite in the groundmass of the andesite EE3-4, (b) Plagioclase in porphyritic andesite altered to fine-grained sericite, with and pyrite occur disseminated in the groundmass of the basalt EE3-13, (c0 Phenocrysts of clinopyroxene in basaltic andesite, occasionally partially altered to chlorite and pyrite disseminated in the groundmass of the andesite at EE3020, (d, e) Plagioclase phenocrysts in a groundmass composed mainly of plagioclase laths in basalt of EE3-22 and EE3-14, (f) Plagioclase phenocrysts in a fine-grained groundmass composed mainly of plagioclase laths, occasionally altered to chlorite and epidote, and calcite occurs as small veinlet EE3-18, (g, h, i) Plagioclase, hornblende and muscovite occur in the granodiorite, hornblende crystals are found in the interstices between larger plagioclase grains. Note; sericite=Ser, plagioclase=Pl, clinopyroxene=Cpx, biotite=Bt, muscovite=Ms, chlorite=Chl, epidote=Epi, hornblende=Hbl, quartz=Qtz, calcite=Cal, pyrite=Py, opque=Opq.

3.4 Conclusions

According to the field observation, megascopic, microscopic study and the rock units can be classified as andesite so called Mawgyi Andesite of volcanic rock and mudstone and phyllite (Shwedaung Formation). Mawgyi andesite with the age of Lower Cretaceous is the most widespread and most distinctive volcanic rock of the study area. Mudstone and phyllite with age of Late Triassic is overlained by Mawgyi Andesite.

3.5 References

Barley, M.E., Khin Zaw, Pickard, A.L., Pak, P., Doyle, M.G., 2003. Jurassic to Miocene magmatism and metamorphism in the Mogok Metamorphic Belt: implications for the India–Eurasia collision in Myanmar. Tectonics 22, 1019–1030. https://doi.org/10.1029/2002TC001398.

Barber, A.J., Khin Zaw, Crow, M.J., 2017. The pre-Cenozoic tectonic evolution of Myanmar. In: Barber, A.J., Khin Zaw, Crow, M.J., Eds., Myanmar: Geology, Resources and Tectonics, Geological Society (London) Memoir. J. Geol. Soc. Lond. 48, 687-712. https://doi.org/10.1144/M48.31.

Chibber, H.L., 1934a. The Geology of Burma, London, Mac Millan, 538p.

Department of Geological Survey and Exploration., 1976. Geology and Exploration Geochemistry of the Pinlebu-Banmauk Area, (Unpublished report No. 2).

Gardiner, N.J., Robb, L.J., Morley, C.K., Searle, M.P., Cawood, P.A., Whitehouse, M.J., Kirkland, C.L., Roberts, N.M.W., Tin Aung Myint., 2016. The tectonic and metallogenic framework of Myanmar: a Tethyan mineral system. Ore Geol. Rev. 79, 26–45.

Gardiner, N.J., Searle, M.P, Morley, C.K., Robb, J.L., Whitehouse, M.J., Roberts, N.M.W., Kirkland, C.L., Spencer, C.J., 2018. The crustal architecture of Myanmar

imaged through zircon U-Pb, Lu-Hf and O isotopes: Tectonic and metallogenic implications. Gondwana Res.62, 27–60.

Khin Zaw., 2017. Overview of mineralization styles and tectonic—metallogenic setting in Myanmar. In: Barber, A.J., Khin Zaw. Crow, M.J., Eds., Myanmar: Geology, Resources and Tectonics, Geological Society (London) Memoir, J. Geol. Soc. London. 48, 531-556. https://doi.org/10.1144/M48.24.

Li, J. X. et al., 2020. Prolonged Neo-Tethyan magmatic arc in Myanmar: evidence from geochemistry and Sr-Nd-Hf isotopes of Cretaceous mafic-felsic intrusions in the Banmauk-Kawlin area. Int. J. Earth Sci. 109, 649-668.

Mitchell, A.H.G., 1981. Phanerozoic plate boundaries in mainland SE Asia, the Himalayas and Tibet. J. Geol. Soc. (London) 138, 109–122, https://doi.org/10.1144/gsjgs.138.2.0109.

Mitchell, A.H.G., 2017. Geological Belts, Plate Boundaries, and Mineral Deposits in Myanmar. Elsevier, 524p.

Myint Thein, Kan Saw, Aye Ko Aung, Kyaw Tint, 1987. Geology of the area between Tigyaing and Katha. Research Titles, Natural Science Research Group, Burma, 26 p.

Noetling, F., 1894. Note on the geology of Wuntho in Upper Burma. Rec Geol. Survey India 27.4.115.124.

Thiri Ye Htut, Kezhang Qin, Guangming Li, Kyaing Sein, Evans, N.J., 2020. Eocene arc magmatism and related Cu-Au (Mo) mineralization in the Shangalon-Kyungalon district, Wuntho-Popa Arc, northern Myanmar. Ore Geol. Rev. 125, https://doi.org/10.1016/j.oregeorev.2020.103678.

United Nations., 1978. Geology and Exploration Geochemistry of the Pinlebu-Banmauk area, Sagaing Division, Northern Burma, Technical Report No. 2, Geological

Survey and Exploration Project, United Nations Development Programme, United Nations, New York.

UN-DGSE, 1978a. Geology and Exploration Geochemistry of the Pinlebu-Banmauk Area, Sagaing Division, Northern Myanmar. Technical Report No. 2. United Nations Development Programme, UN/BUR-72 002/6 United Nations, New York, 69 p.

CHAPTER 4

HYDROTHERMAL ALTERATION OF THE EE3 PROSPECT

4.1 Introduction

This chapter discuss the key mineral assemblages of the hydrothermal alteration zones related to the mineralized quartz veins. In this chapter, geochemical analyses were conducted on major elements oxide, trace elements of the EE3 prospect, aiming to classify of the host rocks.

4.2 Whole-Rocks Composition

Whole-rock compositions of 35 volcanic rocks from the EE3 prospect (location of sample in Figure 3.2, Chapter 3) are determined (Table 4.1). The results of whole-rock major and trace element analyses of representative samples of volcanic rocks are listed in Table 1. The SiO_2 concentrations of the volcanic rocks in the EE3 prospect range between 44.8 wt. % and 73.5 wt. %. The concentration of Al_2O_3 varies between 5.2 wt. % and 18.3 wt. %. The content K_2O ranges from 0.07 wt. % to 2.6 wt. %, while the Na_2O content range from (0.5 wt. % to 3.2 wt. %), and total alkali (Na_2O+K_2O) content range from 0.6 wt. % to 4.5 wt. %. The MnO and P_2O_5 concentrations were less than 0.5 wt. % and LOI values range from 2.3 wt. % to 10.9 wt. % (Table 4.1). All of the host rocks data LOI is high > 2.3. Therefore, samples from the EE3 prospect were plotted on an alteration box plot diagram using the alteration index (AI) against the chlorite-carbonate-pyrite index (CCPI) proposed by Large et al. (2001).

Table 4.1 Concentrations of major elements oxides (wt.%), trace (ppm) of volcanic rocks in the EE3 prospect.

Sample No	EE3-1	EE3-2	EE3-3	EE3-4	EE3-6	EE3-7	EE3-8	EE3-9	EE3-10	EE3-11	EE3-13	EE3-15
Rock Type	Basaltic Andesite			Andesite		Basaltic Andesite		Andesite	Basalt	Andesite	Basalt	
Alteration			C-C-A				E-C-A				S-C-A	
SiO_2 wt%	51.91	49.38	50.36	52.34	56.55	49.95	49.15	57.73	45.42	54.45	44.93	50.51
TiO_2	2.24	1.90	1.39	0.77	1.03	1.83	0.26	1.34	1.32	0.60	0.83	1.45
Al_2O_3	13.62	15.77	13.12	14.48	13.40	13.53	7.45	8.83	15.89	7.83	17.86	12.92
FeO	13.08	10.23	8.99	11.07	5.24	10.03	6.43	7.10	9.59	5.48	12.34	7.67
MnO	0.17	0.19	0.17	0.21	0.09	0.18	0.11	0.13	0.17	0.20	0.20	0.15
MgO	3.85	0.91	5.01	5.74	2.67	4.46	0.77	3.87	5.67	3.32	6.83	3.16
CaO	8.69	18.19	12.65	9.63	10.01	11.10	24.62	14.20	9.54	15.22	8.22	14.05
Na_2O	2.35	0.51	1.09	1.90	3.24	3.02	0.57	0.69	1.69	1.54	1.94	2.97
K_2O	0.34	0.08	1.01	1.26	1.18	0.31	0.11	0.49	1.82	0.29	1.90	0.31
P_2O_5	0.56	0.40	0.29	0.11	0.11	0.26	0.04	0.21	0.19	0.10	0.12	0.28
LOI	3.06	2.28	5.77	2.33	6.38	5.22	10.40	5.31	8.57	10.90	4.68	6.42
Total	99.87	99.84	99.84	99.84	99.92	99.89	99.93	99.91	99.86	99.92	99.85	99.90
S (ppm)	151	92	392	373	165	133	169	188	240	330	142	106
V	383	374	213	302	188	285	178	250	324	122	397	274
Cr	15	22	13	116	32	79	n. d	62	93	16	119	96
Co	41	9	66	57	40	60	27	25	48	40	31	32
Ni	35	12	17	40	31	85	12	35	51	33	43	51
Cu	4	21	9	163	6	11	3	39	26	18	61	12
Zn	162	6	101	80	43	104	n. d	67	74	43	98	68
Pb	n. d	n. d	29	2	n. d	3	n. d	n. d	n. d	n. d	1	2
As	n. d	n. d	2	n. d	n. d	n. d	n. d	n. d	n. d	n. d	n. d	n. d
Mo	n. d	1	2	n. d	n. d	n. d	n. d	n. d	n. d	n. d	n. d	n. d
Rb	6	1	17	22	20	6	2	10	34	6	37	6
Sr	85	804	494	221	131	115	272	83	146	62	281	108
Ba	53	n. d	46	104	95	41	n. d	6	144	11	241	48
Y	79	67	51	24	24	49	16	36	36	20	30	45
Zr	274	230	159	47	71	155	28	108	102	54	64	136
Nb	8	9	5	2	3	6	2	4	4	2	3	5

Abbreviation: C-C-A: chlorite-carbonate-alteration, E-C-A: epidote-calcite±albite-alteration, S-C-A: sericite-carbonate-alteration, n.d: not determined.

Table 4.2 Concentrations of major elements oxides (wt.%), trace (ppm) of volcanic rocks in the EE3 prospect. (cont)

Sample No	EE3-16	EE3-18	EE3-19	EE3-20	EE3-21	EE3-22	EE3-23	EE3-24	EE3-25	EE3-26	EE3-28	EE3-29	EE3-31
Rock Type			Basaltic Andesite				Basalt			Andesite			Basalt
Alteration					C-C-A								
SiO_2 wt%	44.77	52.98	46.28	45.72	49.98	49.72	48.45	63.86	53.77	60.71	73.52	56.28	51.43
TiO_2	1.44	1.45	1.34	1.02	1.29	1.48	1.65	0.85	1.18	0.59	0.52	0.74	1.31
Al_2O_3	17.01	12.79	13.04	11.39	12.42	13.57	18.30	13.79	11.29	7.84	5.17	8.45	15.05
FeO	9.73	12.01	10.07	10.21	8.81	9.92	8.66	7.17	7.53	8.83	5.51	5.86	9.74
MnO	0.15	0.17	0.30	0.20	0.13	0.25	0.12	0.18	0.13	0.14	0.07	0.11	0.19
MgO	5.14	5.62	7.08	5.06	3.37	5.74	9.12	2.70	3.08	4.92	3.31	4.22	7.02
CaO	9.77	9.15	13.73	15.17	13.86	11.88	5.73	2.93	13.04	7.87	5.11	14.45	9.06
Na_2O	2.43	2.30	2.33	2.17	1.21	2.59	2.41	2.85	1.36	0.6	0.61	1.58	2.69
K_2O	2.09	0.21	0.25	0.43	2.19	0.28	1.19	1.66	2.14	2.65	0.32	0.07	0.19
P_2O_5	0.18	0.18	0.19	0.17	0.21	0.21	0.16	0.2	0.19	0.18	0.03	0.08	0.16
LOI	6.69	3.03	5.15	6.99	6.28	4.26	4.07	3.08	5.75	5.58	5.79	7.97	3.02
Total	99.39	99.89	99.76	98.53	99.75	99.88	99.85	99.26	99.46	99.92	99.96	99.81	99.87
S (ppm)	5043	145	286	13674	1560	145	159	101	4438	109	108	893	122
V	300	285	359	186	303	344	229	105	290	280	169	181	286
Cr	74	105	104	57	68	128	310	n. d	55	61	8	296	295
Co	25	61	67	39	14	43	63	27	36	7	22	51	56
Ni	61	52	74	47	53	98	138	2	30	51	26	85	126
Cu	n. d	43	10	346	28	12	n. d	3	110	n. d	n. d	240	26
Zn	103	96	104	76	44	93	142	100	26	97	49	41	103
Pb	4	n. d	8	n. d	4	n. d	1	n. d	6	n. d	n. d	n. d	3
As	n. d	n. d	n. d	10	n. d	n. d	n. d	n. d	n. d	n. d	1	n. d	n. d
Mo	n. d	n. d	n. d	n. d	n. d	n. d	n. d	n. d	n. d	n. d	n. d	n. d	n. d
Rb	41	3	4	8	45	3	19	27	42	61	12	1	2
Sr	187	115	161	122	213	148	137	108	168	86	20	60	164
Ba	98	29	23	10	66	17	120	271	70	70	n. d	n. d	n. d
Y	39	43	44	28	40	47	41	40	37	9	7	22	36
Zr	151	126	121	88	106	138	128	115	97	9	14	49	112
Nb	5	4	4	3	4	5	4	4	3	1	1	2	4

Abbreviation: C-C-A: chlorite-carbonate-alteration, E-C-A: epidote-calcite±albite-alteration, S-C-A: sericite-carbonate-alteration, n.d: not determined.

4.3 Hydrothermal Alteration and Alteration Mineral Assemblages

The alteration features and the effects of hydrothermal alteration on whole-rock geochemical composition of the EE3 Prospect were plotted on an alteration box plot diagram using the alteration index (AI) vs the chlorite-carbonate-pyrite index (CCPI) proposed by Large et al. (2001) (Figure 4.1). The alteration index (AI) was calculated by 100 times of the ratio of the sum of K_2O and MgO to the sum of K_2O, MgO, Na_2O, and CaO. The chlorite-carbonate-pyrite index (CCPI) was calculated by 100 times of the ratio of the sum of MgO and FeO to the sum of MgO, FeO, Na_2O, and K_2O. All major elements used to calculate AI an CCPI are expressed as wt. %. LOI of all of samples is high. The least LOI is 2.3 (EE3-2) and the highest LOI is 13.6 (EE3- 19) and (Table 4.1). Thirteen samples are host rock andesite/basalt volcaniclastic succession. The data show that one sample is plotted in the least altered box, and the other samples are near epidote/calcite boundary.

The samples from the EE3 Prospect plotted on the alteration box plot diagram display (1) chlorite-carbonate alteration, (2) sericite-carbonate alteration, and (3) epidote-calcite ± albite alteration. The LOI values may misclassify between the least altered and altered sample in this study. However, the result of least altered rocks classified by box plot are consistent with the petrography. The variation in alteration assemblages in relation to vein geometry is shown in Figure 4.2. The variation in alteration styles has been interpreted as a direct reflection of the depth of the intensity of the wall-rock alteration is a largely controlled by the composition and competence of the host rocks and their associated structures. Distinct hydrothermal alteration mineral assemblages are found adjacent to the mineralized veins within the study area. The rocks in the study area are moderate to intensely altered.

Hydrothermal alteration along the quartz veins encompasses proximal (sericite-carbonate alteration), intermediate (epidote-calcite±albite alteration) and distal (chlorite-carbonate alteration) alteration zones that are defined by mineral assemblages as indicated in Figure 4.3. The strongly altered rocks adjacent to auriferous quartz veins are typically enriched in sulfide minerals. Further away from the vein, the alteration is characterized by various amounts of chlorite and calcite, but the proximal parts of the vein haloes comprise biotite, epidote, albite, quartz, chlorite, sericite and carbonate minerals.

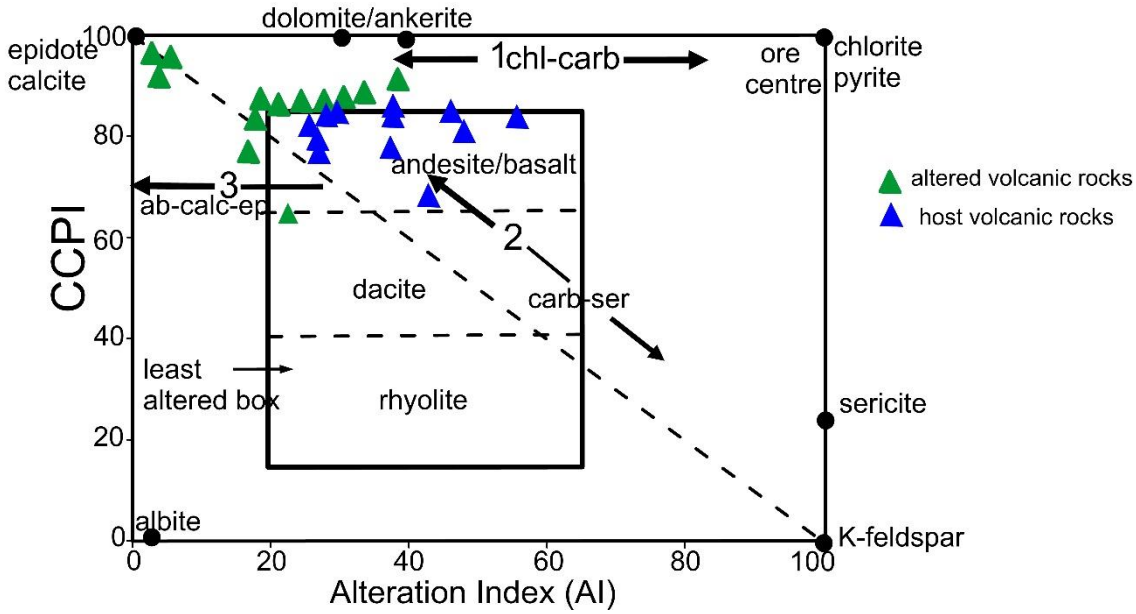

Figure 4.1 Alteration box plot with the alteration index (AI) versus the chlorite-carbonate-pyrite index (CCPI) (modified from Large et al., 2001).

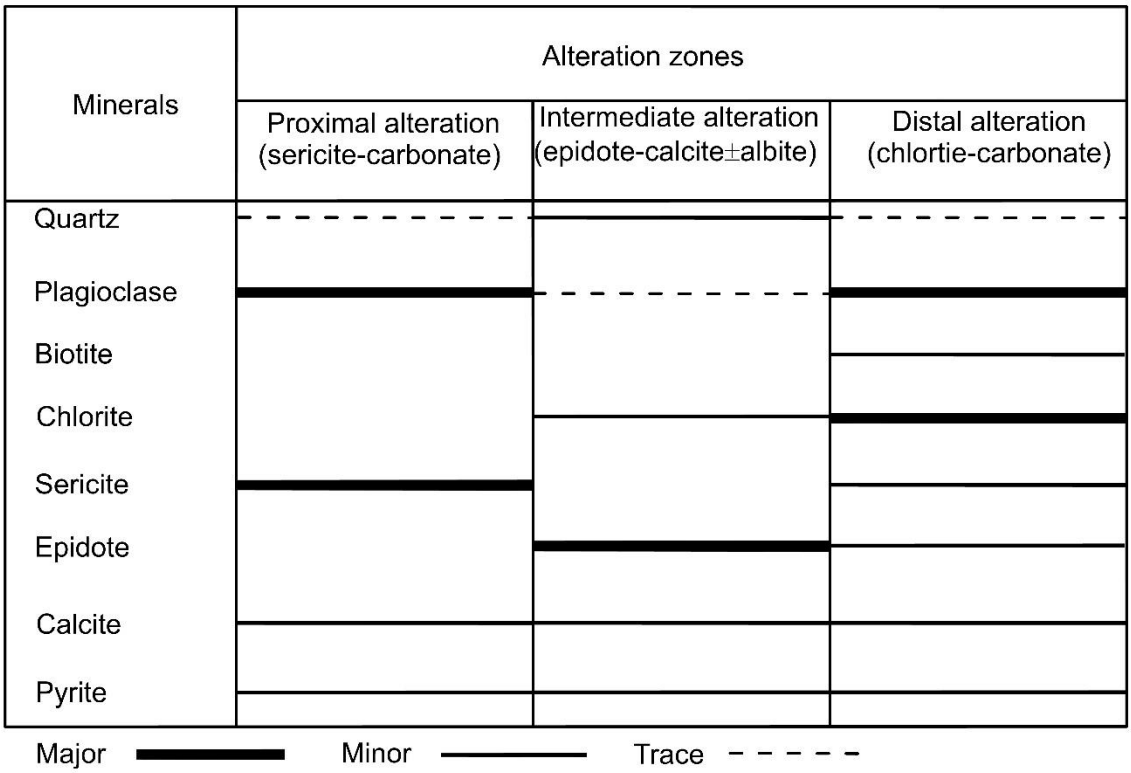

Figure 4.2 Diagrammatic figure showing alteration geometry, intensity and patterns of veins and their adjacent boundaries.

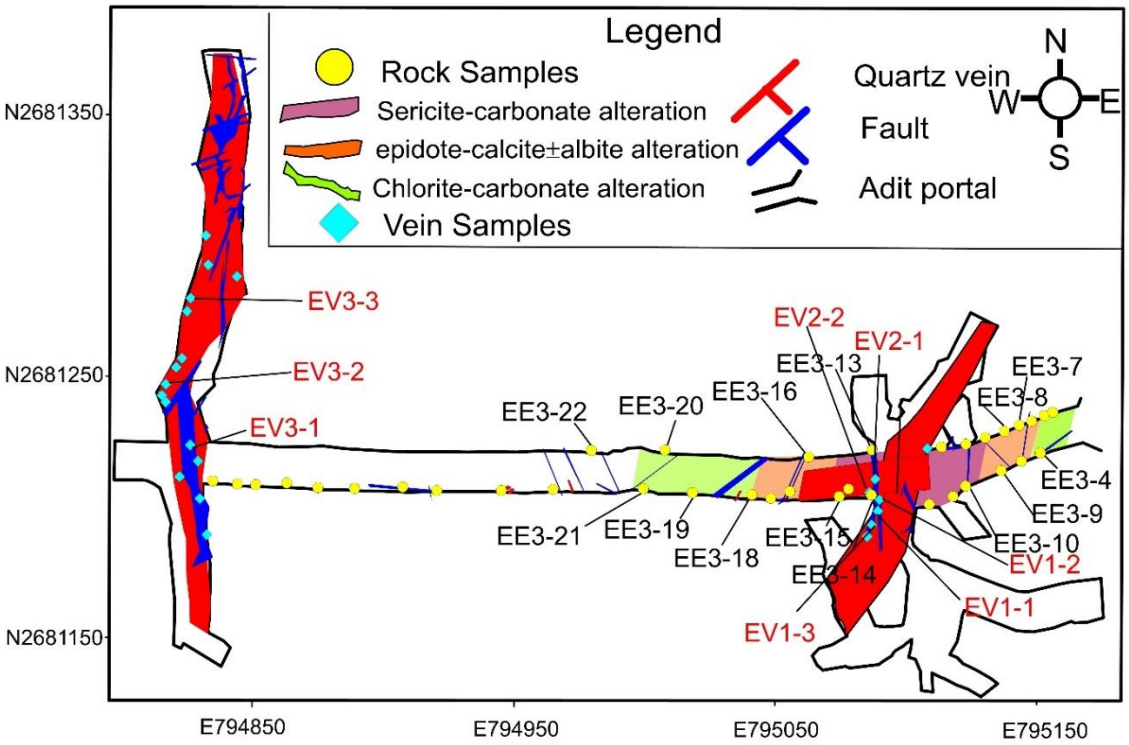

Figure 4.3 Sample location of the Underground map (modified after Eternal mining group Co. Ltd).

4.3.1 Proximal (Sericite-Carbonate) Alteration

The proximal alteration zone (sericite-carbonate alteration) extends up to 15 m from the Stage-I veins. The assemblage is composed of sericite (40 vol %; Figure 4.4 9d, e), plagioclase (30 vol %), quartz (10 vol %), calcite (30 vol %). The felsic minerals were altered to sericite. Sericite replaced plagioclase and occurs as yellowish-brown flakes (Figure 4.4e). The sericite-carbonate assemblages are very common adjacent the ore zone. Sericite-carbonate alteration often formed especially along the marginal zone of the host rock. X-ray diffraction pattern of bulk rock and oriented samples shown in Figure 4.5.

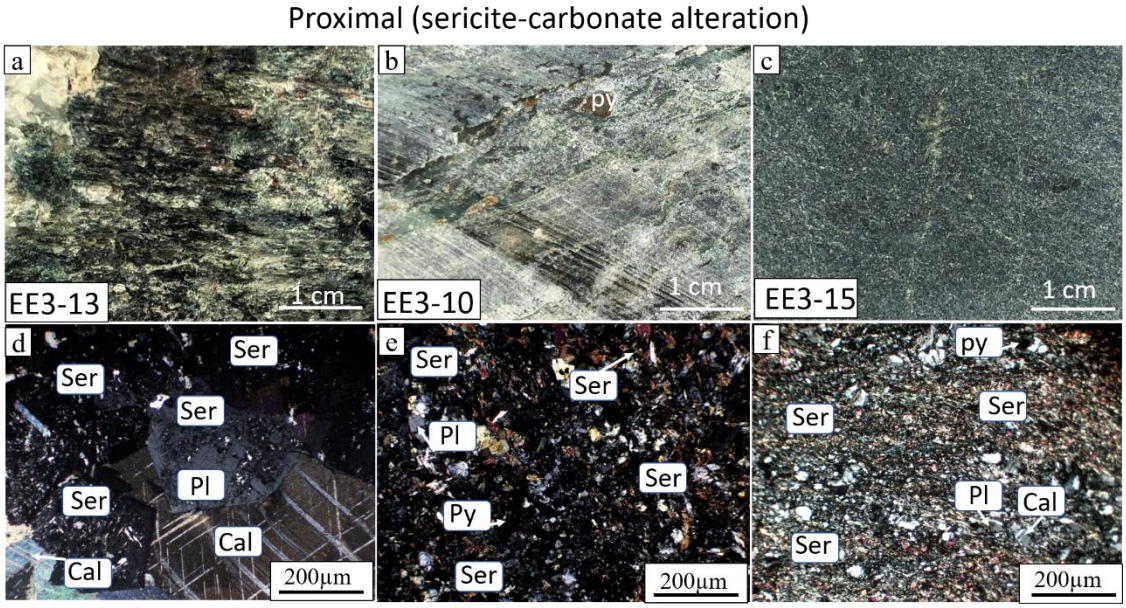

Figure 4.4 Photographs of hydrothermally altered hand samples (a, b, c, g, h, i, m, n, o) and their respective photomicrographs (d, e, f, j, k, l, p, q, r) in the EE3 Prospect. The mode of occurrence and distribution of hydrothermal minerals in proximal (sericite-carbonate alteration) zone area shown in (a, b, c, d, e, f). Abbreviations: Qtz-quartz, Bt=biotite, Py=pyrite, Chl=chlorite, Epi=epidote, Pl=plagioclase, Ser=sericite, Cal= calcite.

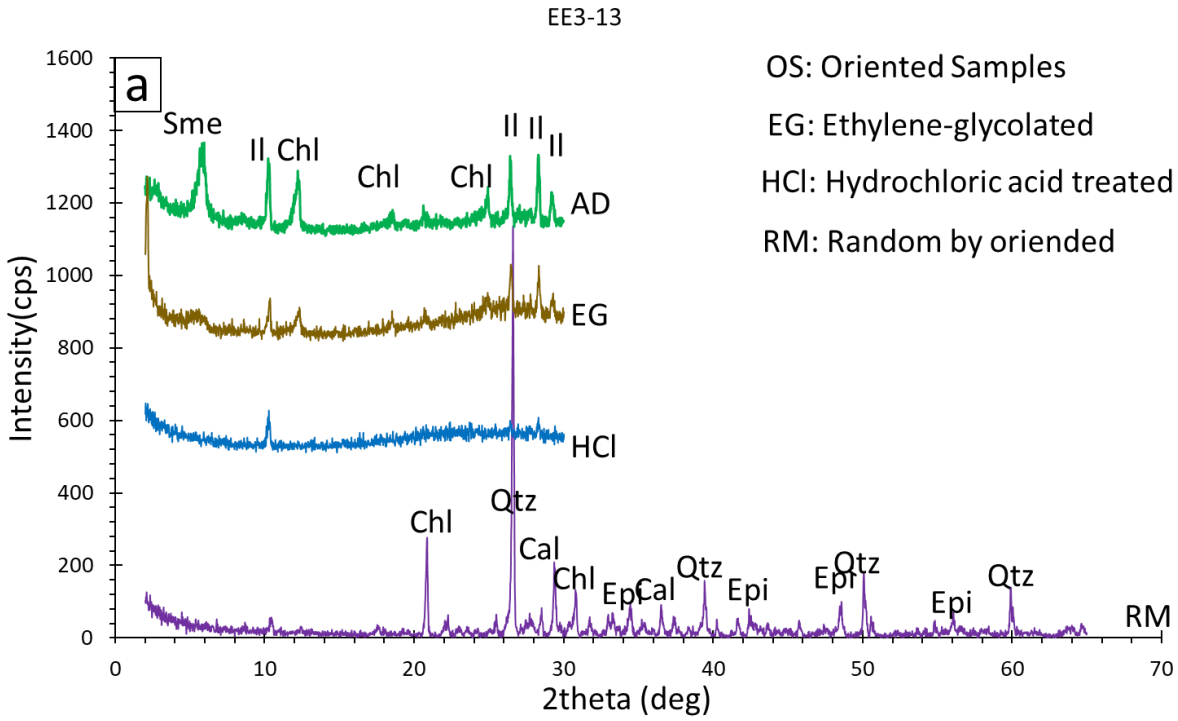
EE3-13
a
OS: Oriented Samples
EG: Ethylene-glycolated
HCl: Hydrochloric acid treated
RM: Random by oriended
Intensity(cps)
2theta (deg)
Sme
Il
Chl
AD
EG
HCl
Qtz
Cal
Epi
RM

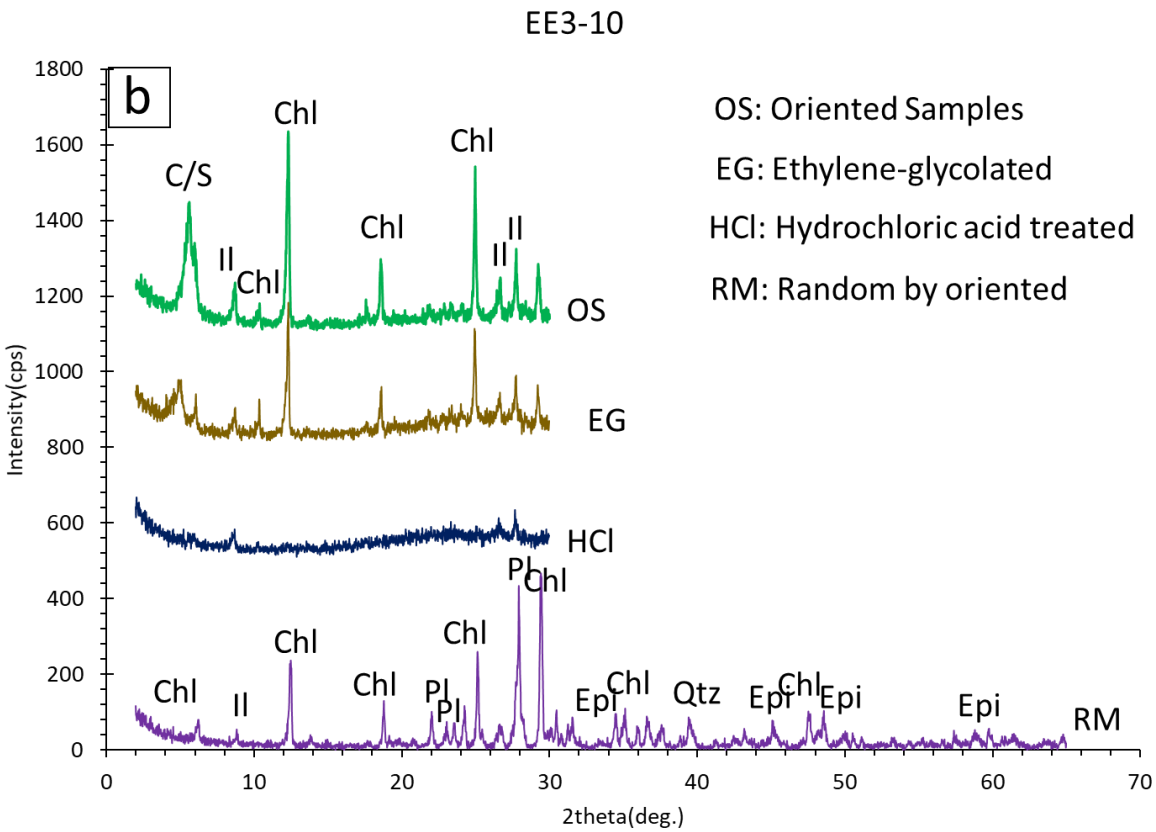
EE3-10
b
OS: Oriented Samples
EG: Ethylene-glycolated
HCl: Hydrochloric acid treated
RM: Random by oriented
Intensity(cps)
2theta(deg.)
C/S
Il
Chl
OS
EG
HCl
Pl
Epi
Qtz
RM

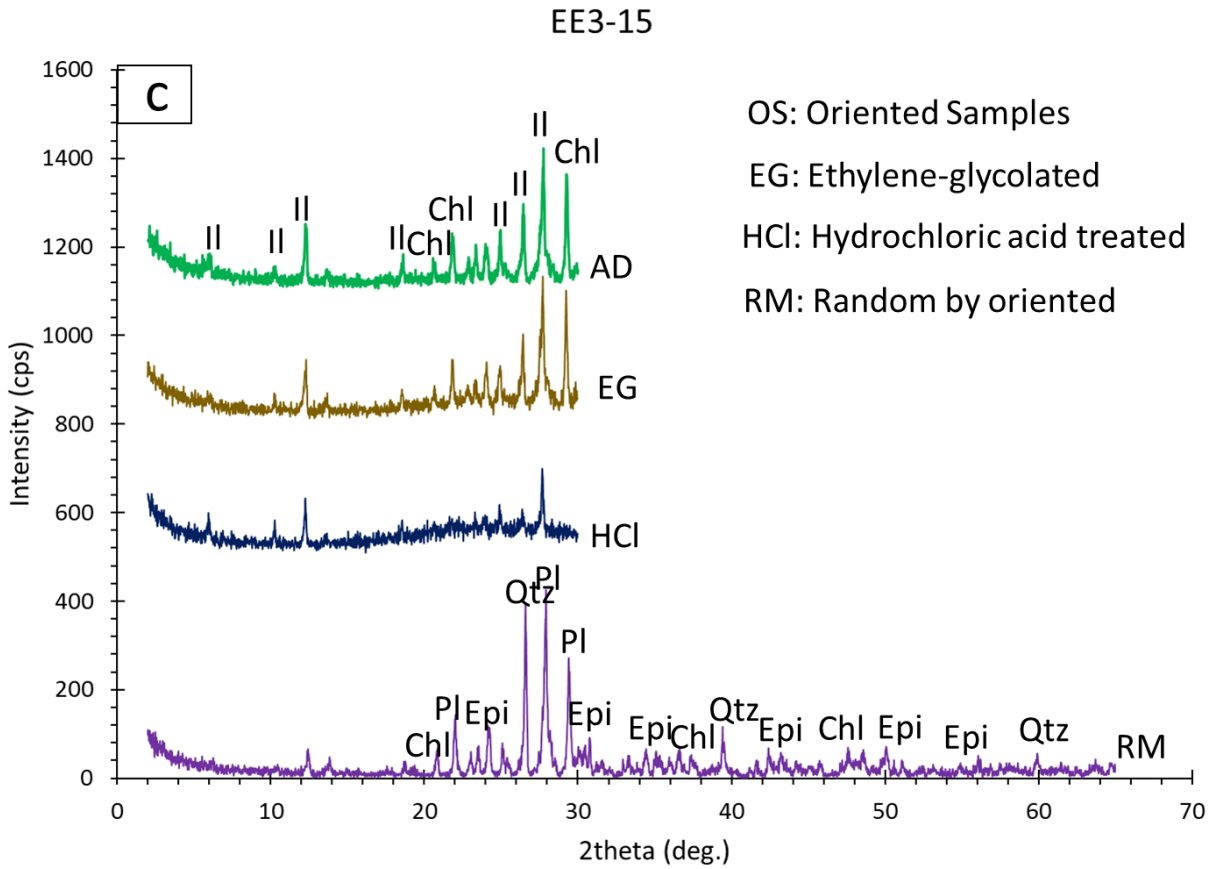

Figure 4.5 (a), (b) and (c) X-ray diffraction pattern of bulk rock and oriented samples of (Sample Id; EE3-13, EE3-10, EE3-15) for proximal alteration zone (sericite-carbonate alteration). Abbreviations: Qtz=quartz, Chl=chlorite, Epi=epidote, Pl=plagioclase feldspar, Ser=sericite, Cal=calcite, Sme=smecite, Il=illite.

4.3.2 Intermediate (Epidote-Calcite±Albite) Alteration

The intermediate epidote-calcite±albite alteration zone ranges between 10 m in width. Seventy volume percent of the rock is composed of epidote, others are chlorite (10 vol %), calcite (10 vol %), and quartz (10 vol %) (Figure 4.6j, k, l). In this alteration zone, epidote, pyrite, sericite and quartz mineral assemblages are indicative of the moderate to high temperatures hydrothermal fluid probably 230-300 ° C (Corbett and Leach, 1995). X-ray diffraction pattern of bulk rock and oriented samples shown in Figure 4.7.

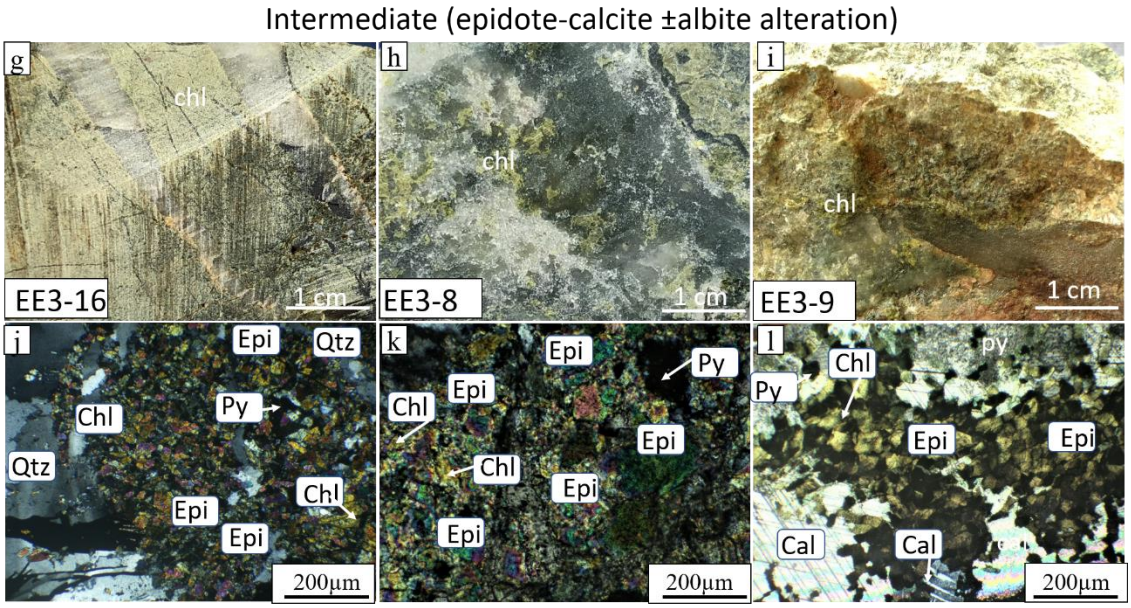

Figure 4.6 Photographs of hydrothermally altered hand samples (a, b, c, g, h, i, m, n, o) and their respective photomicrographs (d, e, f, j, k, l, p, q, r) in the EE3 Prospect. While the mode of occurrence and distribution of hydrothermal minerals in intermediate (epidote-calcite±albite alteration). Abbreviations: Qtz=quartz, Bt=biotite, Py=pyrite, Chl=chlorite, Epi=epidote, Pl=plagioclase, Ser=sericite, Cal=calcite.

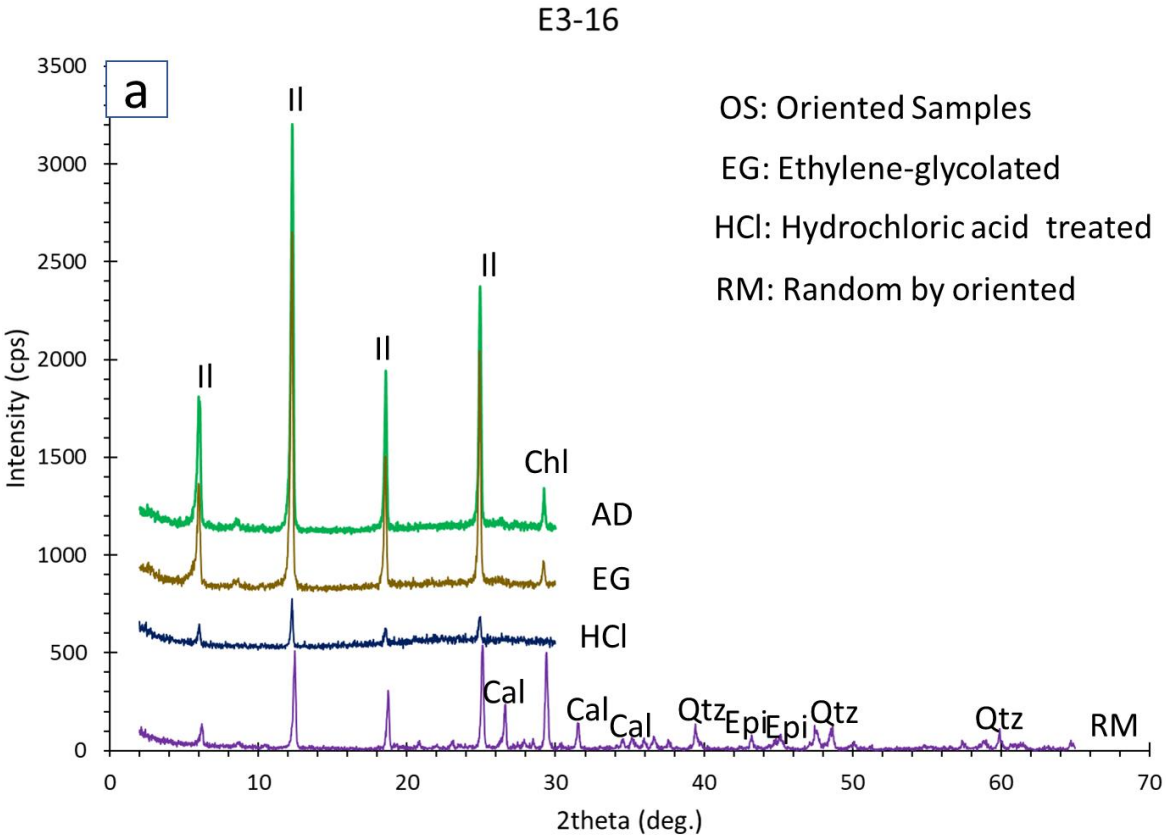

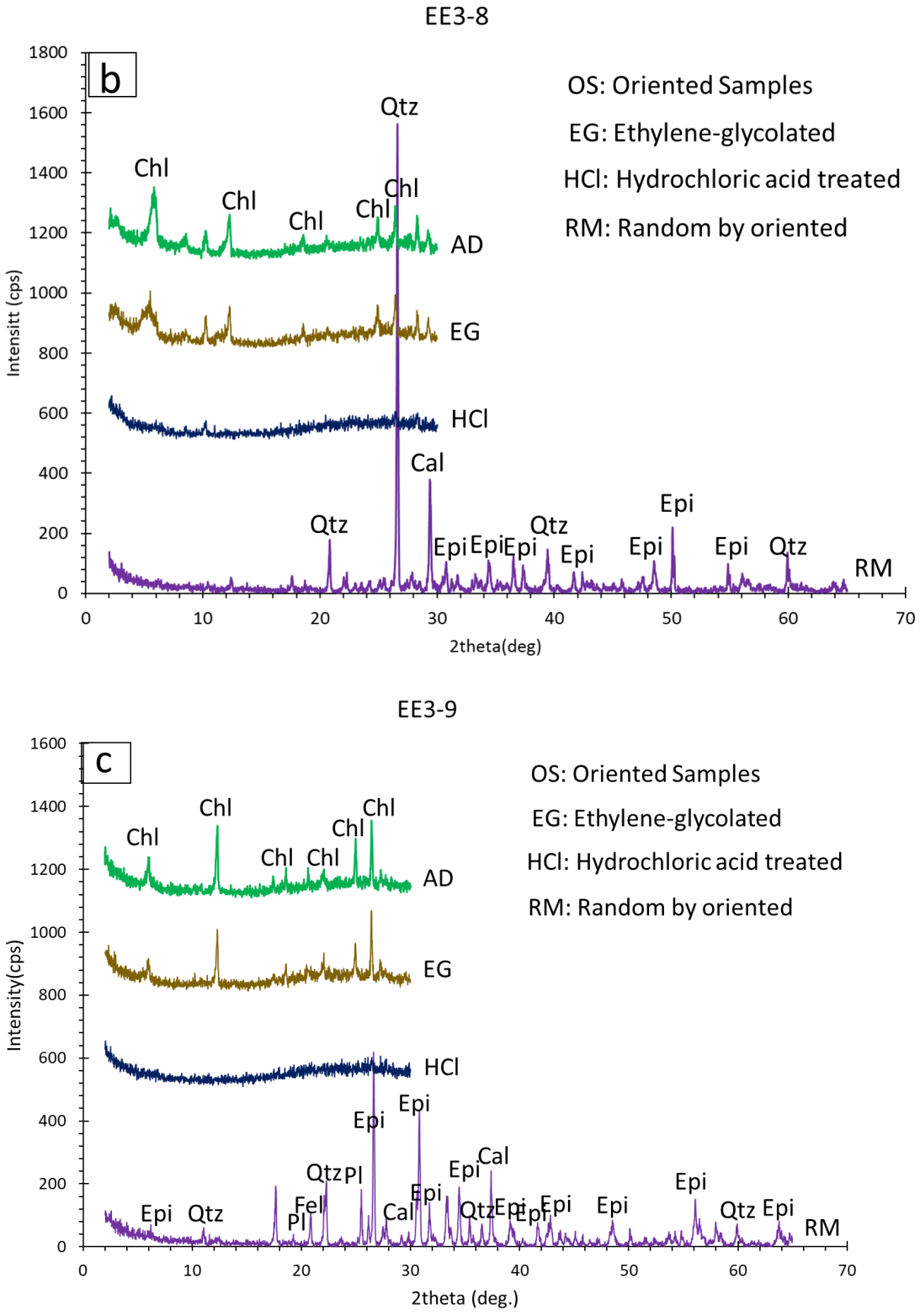

Figure 4.7 (a), (b) and (c) X-ray diffraction pattern of bulk rock and oriented samples of (Sample Id; EE3-16, EE3-8, EE3-9) for proximal alteration zone (sericite-carbonate alteration). Abbreviations: Qtz=quartz, Chl=chlorite, Epi=epidote, Pl=plagioclase feldspar, Ser=sericite, Cal=calcite, Il=illite.

4.3.3 Distal (Chlorite-Carbonate) Alteration

The distal chlorite-carbonate alteration zone in the andesite host rock is defined by the assemblage chlorite-epidote-calcite-feldspar-sericite and the zone extends outwards 5–30 m from the Stage-I veins. The transition from least altered to distal alteration zone is characterized by the presence of epidote and sericite and the increase in chlorite and calcite. Pyrite is always present in trace amounts.

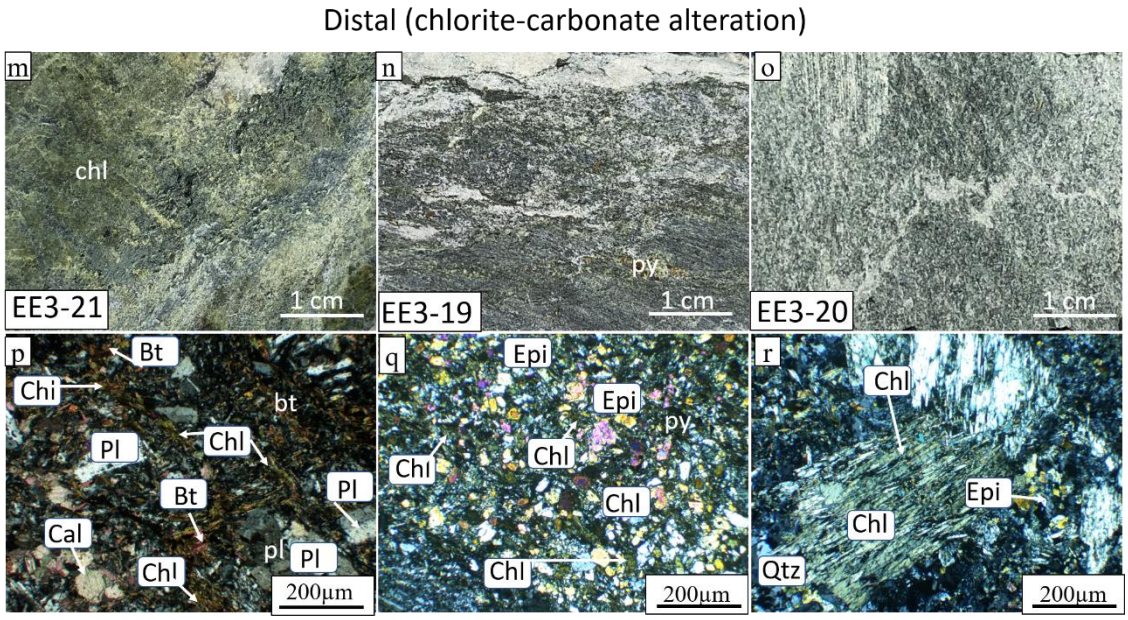

Figure 4.8 Photographs of hydrothermally altered hand samples (a, b, c, g, h, i, m, n, o) and their respective photomicrographs (d, e, f, j, k, l, p, q, r) in the EE3 Prospect. Distal (chlorite-carbonate alteration) zones are shown in (g, h, i, j, k, l) and (m, n. o, p, q, r), respectively. Abbreviations: Qtz=quartz, Bt=biotite, Py=pyrite, Chl=chlorite, Epi=epidote, Pl=plagioclase feldspar, Ser=sericite, Cal=calcite.

EE3-21

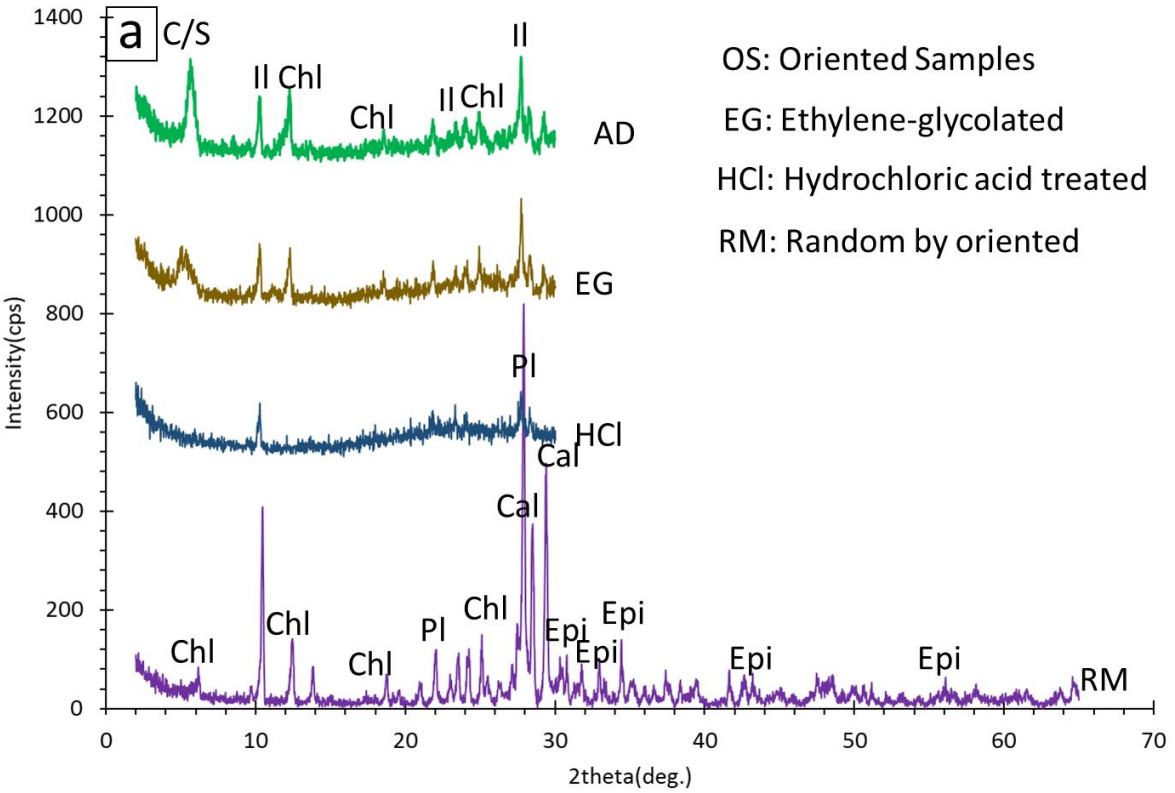
a
C/S
Il
Il Chl
Chl
Il Chl
AD
EG
Pl
HCl
Cal
Cal
Chl
Chl
Pl
Chl
Epi
Epi
Epi
Epi
Epi
Chl
Chl
RM
Intensity(cps)
2theta(deg.)
OS: Oriented Samples
EG: Ethylene-glycolated
HCl: Hydrochloric acid treated
RM: Random by oriented

EE3-19

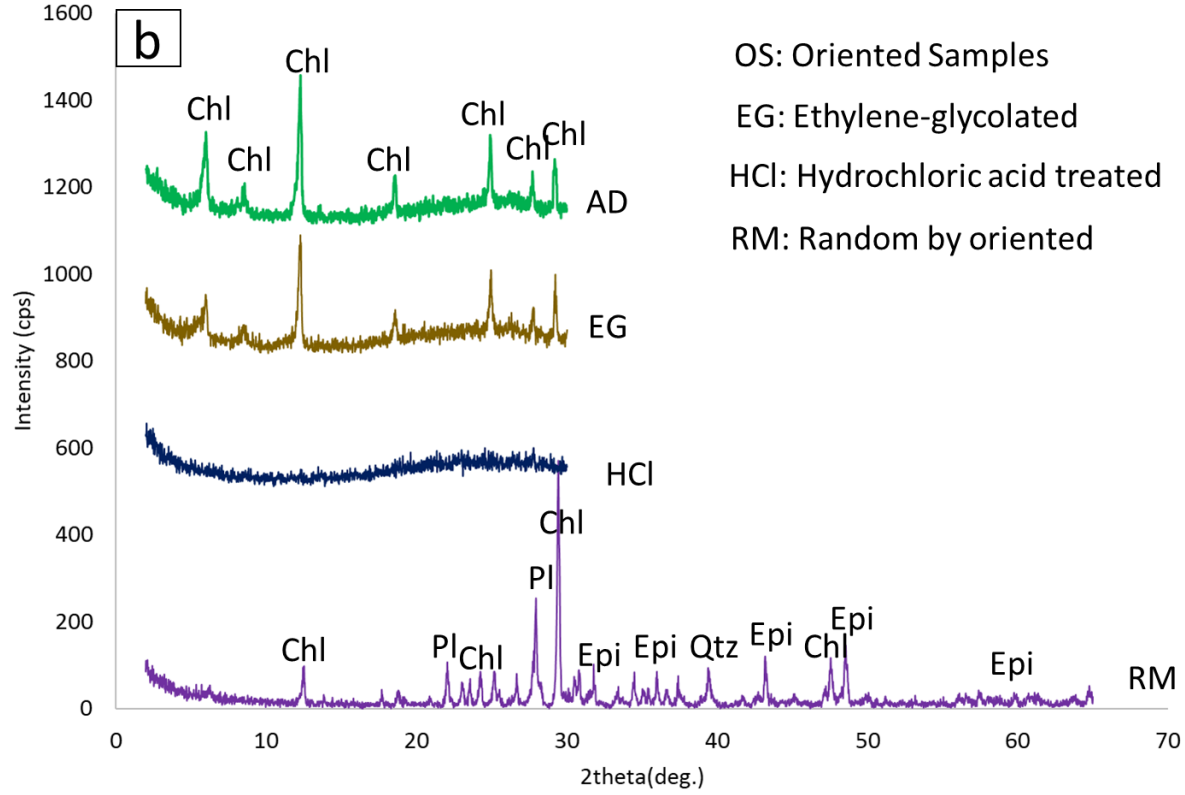
b
Chl
Chl
Chl
Chl
Chl
Chl
Chl
AD
EG
HCl
Chl
Pl
Chl
Pl
Chl
Epi
Epi
Qtz
Epi
Chl
Epi
Epi
RM
Intensity (cps)
2theta(deg.)
OS: Oriented Samples
EG: Ethylene-glycolated
HCl: Hydrochloric acid treated
RM: Random by oriented

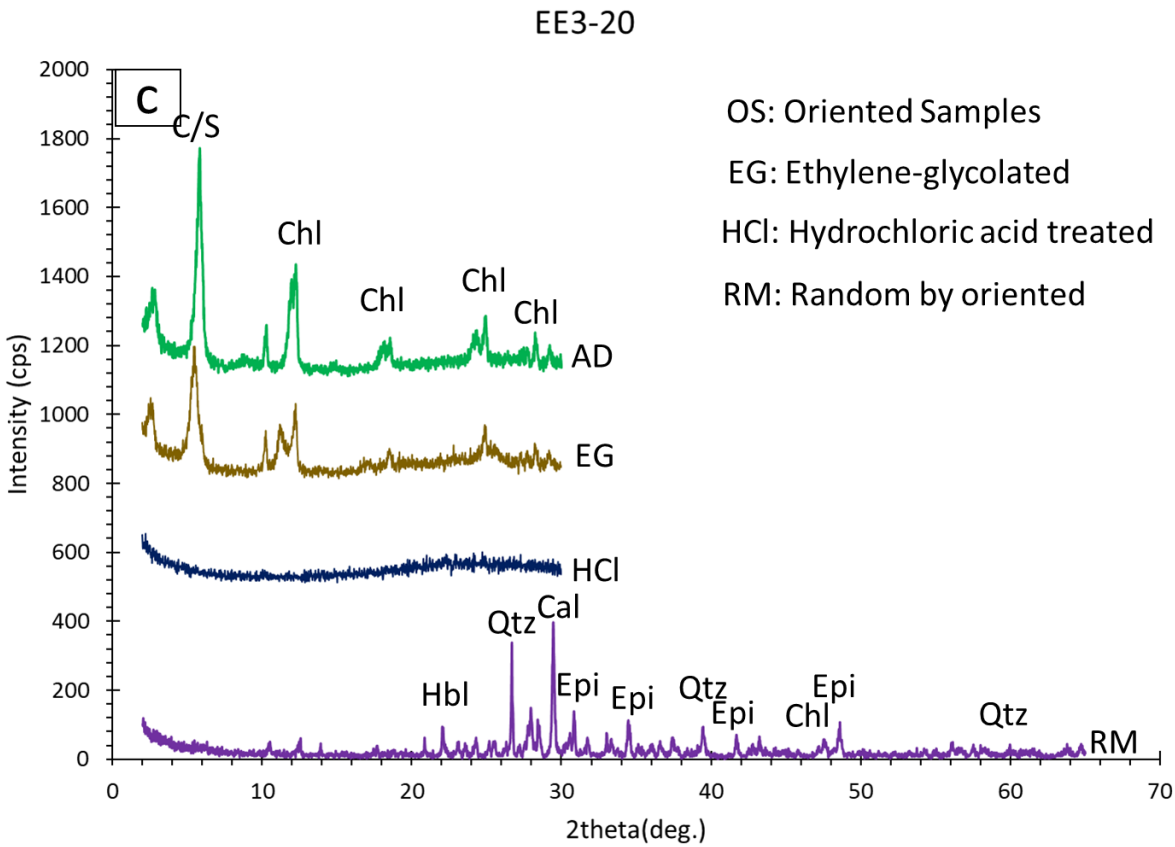

Figure 4.9 (a), (b) and (c) X-ray diffraction pattern of bulk rock and oriented samples of (Sample Id; EE3-21, EE3-19, EE3-20) for proximal alteration zone (sericite-carbonate alteration). Abbreviations: Qtz=quartz, Chl=chlorite, Epi=epidote, Pl=plagioclase feldspar, Ser=sericite, Cal=calcite, Sme=smecite, Il=illite.

Chlorite group minerals are dominant. Chlorite altered especially hornblende and biotite, which gives dark green to pale green color (Figure 4.8p, q, r). Chlorite-carbonate alteration occurs after mafic mineral especially biotite. Chlorite is the most common alteration product of the main alteration assemblages Pyrite occurs in all altered rocks, and it can be recognized in the margin of the quartz vein. Chlorite-carbonate alteration is widespread not only in the fracture zones but also in wall rocks the surrounding stringer, veinlets, and quartz veins. X-ray diffraction pattern of bulk rock and oriented samples shown in Figure 4.9.

4.4 Conclusions

In the EE3 Prospect, the alteration is characterized by various amounts of chlorite and calcite away from the veins, but the altered rock at proximal parts from the vein comprise epidote, chlorite, and sericite. Hydrothermal alteration adjacent to the Stage-I massive quartz vein is classified into proximal sericite-carbonate alteration, intermediate epidote-calcite±albite alteration and distal chlorite-carbonate alteration zones that are defined by using box plot diagram and based on the interpretation of thin sections and XRD results of host rock shown in Figure. 8.

4.5 References

Corbett, G.J., Leach, T.M., 1995. SW Pacific gold-copper system: Structure, alteration and mineralization workshop, PACRIM Conference, Auckland, New Zealand. 23-24 Nov-1995.

Large, R.R., Gemmell, J.B., Paulick, H., Huston, D.L., 2001. The alteration box plot: A simple approach to understanding the relationships between alteration mineralogy and lithogeochemistry associated with VHMS deposits. Econ. Geol., 96, 957-971.

CHAPTER 5

MINERALIZATION OF THE EE3 PROSPECT

5.1 Introduction

The main important factor of this research to understand the genetic aspects and mineralization style. The study contributes the results of petrography, ore microscopy, scanning electron microscope-EDS and wall-rock alteration mineralogy, fluid inclusion studies to emphasize the occurrence of gold mineralization at study area, and to determine deposit type. Therefore, this chapter will discuss the mineralization styles of the EE3 prospect.

5.2 Mineralization of the EE3 Prospect

The total length of tunnel of EE3 prospect is approximately 362 m from mine portal which is located 190 m above of the sea level. The main prospect is 225° trend. In this prospect, gold-bearing quartz vein generally N-S and dipping is nearly vertical. Gold-bearing quartz vein is hosted in andesite. Plan map view of EE3 prospect and mineralized vein is shown in Figure 5.1. Underground mining systems (Figure 5.2a) are used for the ore production, with the gravel pumping method used for weathered exposures.

The major mineralization style of the EE3 prospect is represented by gold-bearing quartz veins that are hosted in the volcanic rocks. This rock is often strongly altered near the fault zone. According to the field observation, the style of mineralization includes massive quartz-sulfide vein, stockwork, dissemination and veinlets. The thickness of vein is 0.1 to 5 m. The geometry of the veins (Stage-I, II, III) are shown in Figure 5.2, 4.12, 4.13 and their hand specimens of sulfide rich quartz veins are presented in Figure 5.5. Three main vein types are identified in this prospect. They are (1) massive quartz-carbonate-sulfide veins (EV1-1, EV1-2, EV1-3) (Stage-I), E-W trending vein (EV2-1,

EV2-2) (Stage-II) that intersected the Stage-I veins, and the third generation veins (EV3-1, EV3-2, EV3-3) (Stage-III) parallel to the Stage-I veins.

The thickness of gold-bearing quartz-carbonate-sulfide vein hosted by andesite (Stage-I quartz vein) is 1m to 5m (Figure 5.2b). Due to the fault movement formed shear plane in the Stage-I quartz vein in Figure 5.2c and mineralized quartz veins are displaced by the fault's movement (Figure 5.2d). E-W trending quartz-carbonate veins (Stage-II vein) that intersected the Stage-I vein (Figure 5.3a, b). The nature of Stage-III quartz-sulfide veins is vein offset due to the fault movement (Figure 5.4a). Mineralized veins occur along the fault zone and breccia zone. In some places, the ore veins are found as the lens-shaped or pinch and swelling structure (Figure 5.4 c, d, e). Some veins show the banded nature (Figure 5.4b). The Stage-I veins and Stage-III veins are the biggest mineralized vein in the volcanic rocks, while the Stage-II veins are barren. Vein style of the Stage-I veins and Stage-III veins are massive and very wide range.

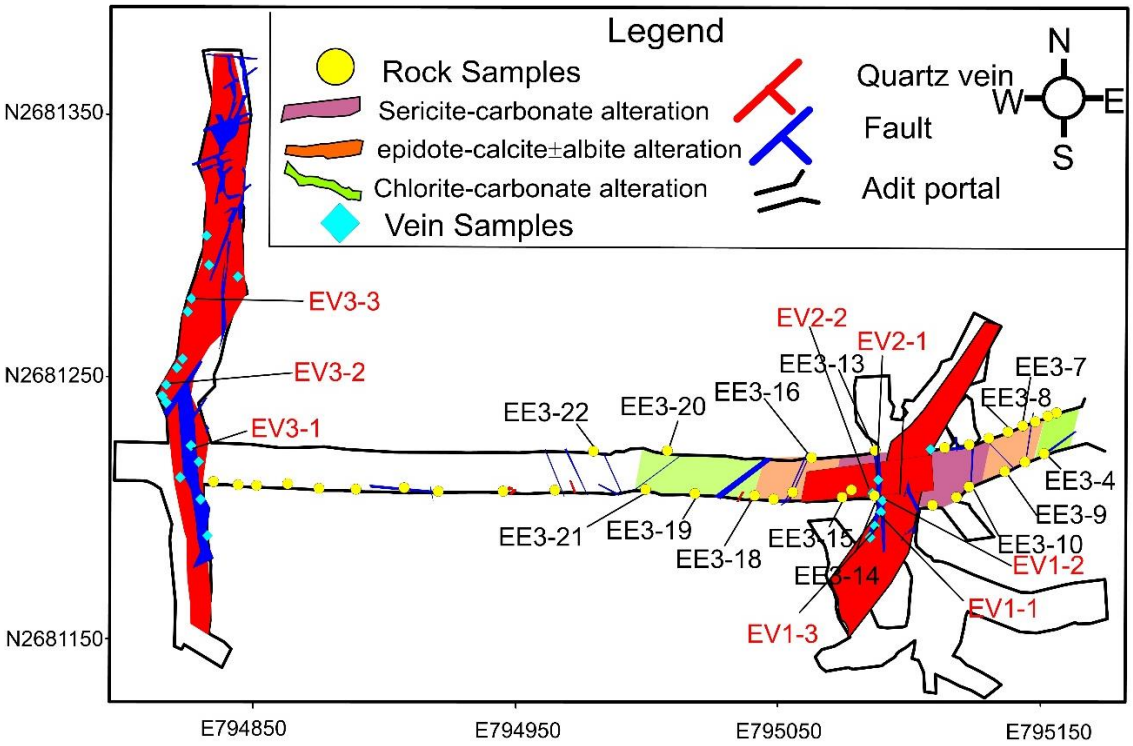

Figure 5.1 Plan map view of EE3 prospect and mineralized veins of EV1-1, EV1-2, EV1-3, (Stage-I veins), EV2-1, EV2-2, (Stage-II veins) and EV3-1, EV3-2, EV3-3d, (Stage-III veins).

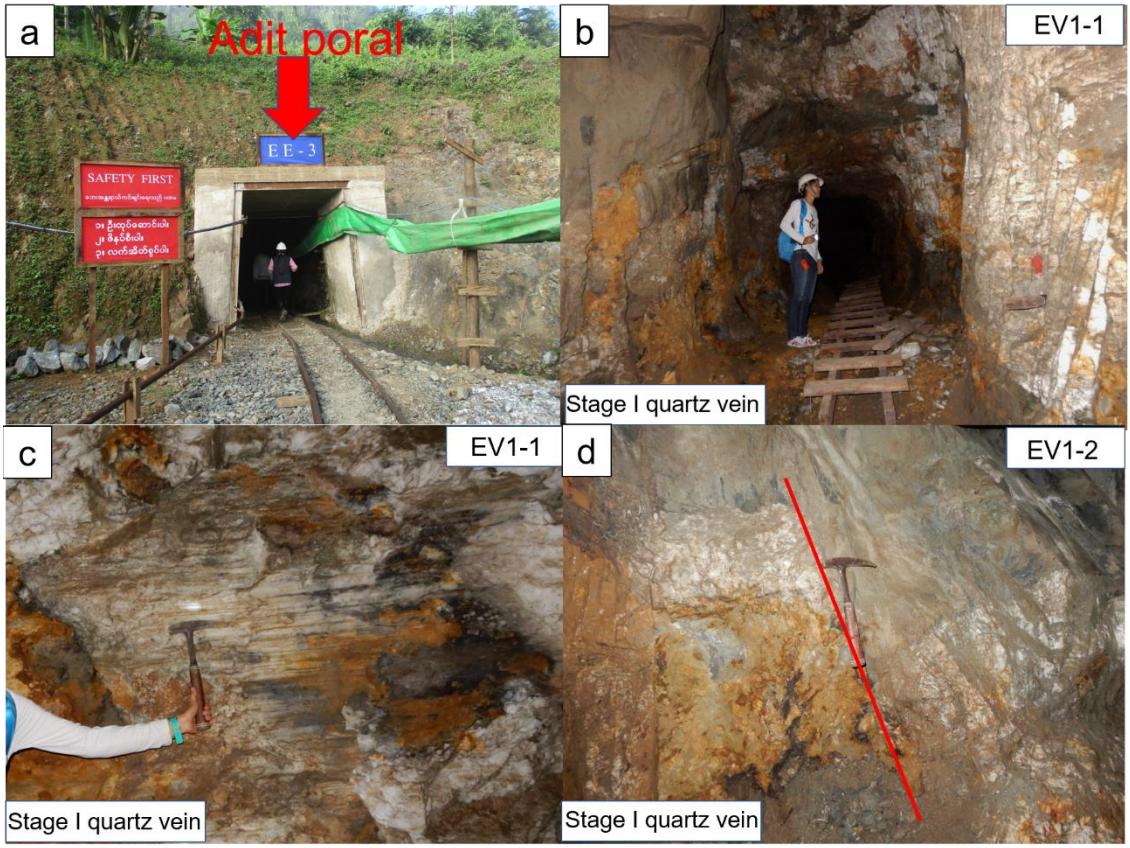

Figure 5.2 (a) the portal of underground adit at the EE3 prospect, (b)photographs showing nature of gold-bearing quartz-carbonate-sulfide vein hosted by andesite of the Stage-I quartz vein (EV1-1), (c) shear plane due to the fault movement of the Stage-I quartz vein (EV1-1), (d) mineralized quartz vein which was displaced by a fault movement (EV1-2).

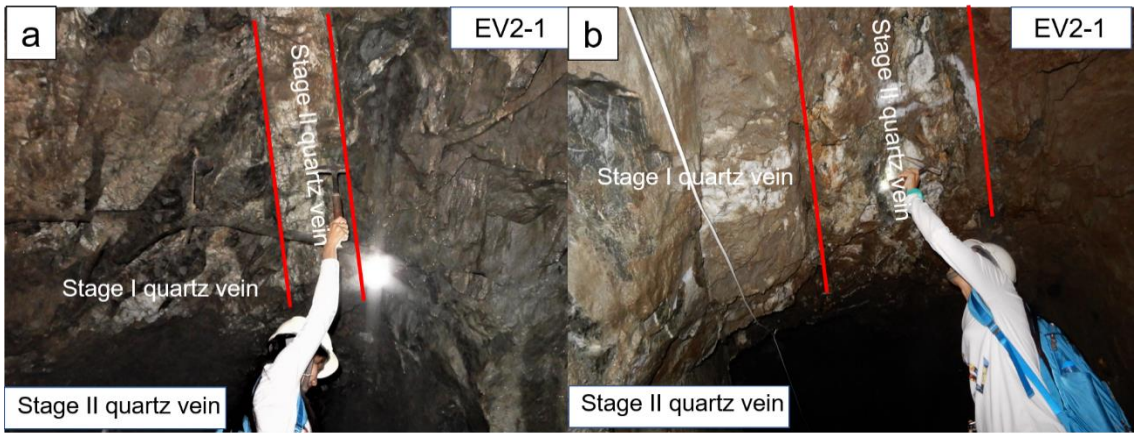

Figure 5.3 (a) Photographs showing (a, b) E-W trending Stage-II vein that intersected the Stage-II vein (EV2-1).

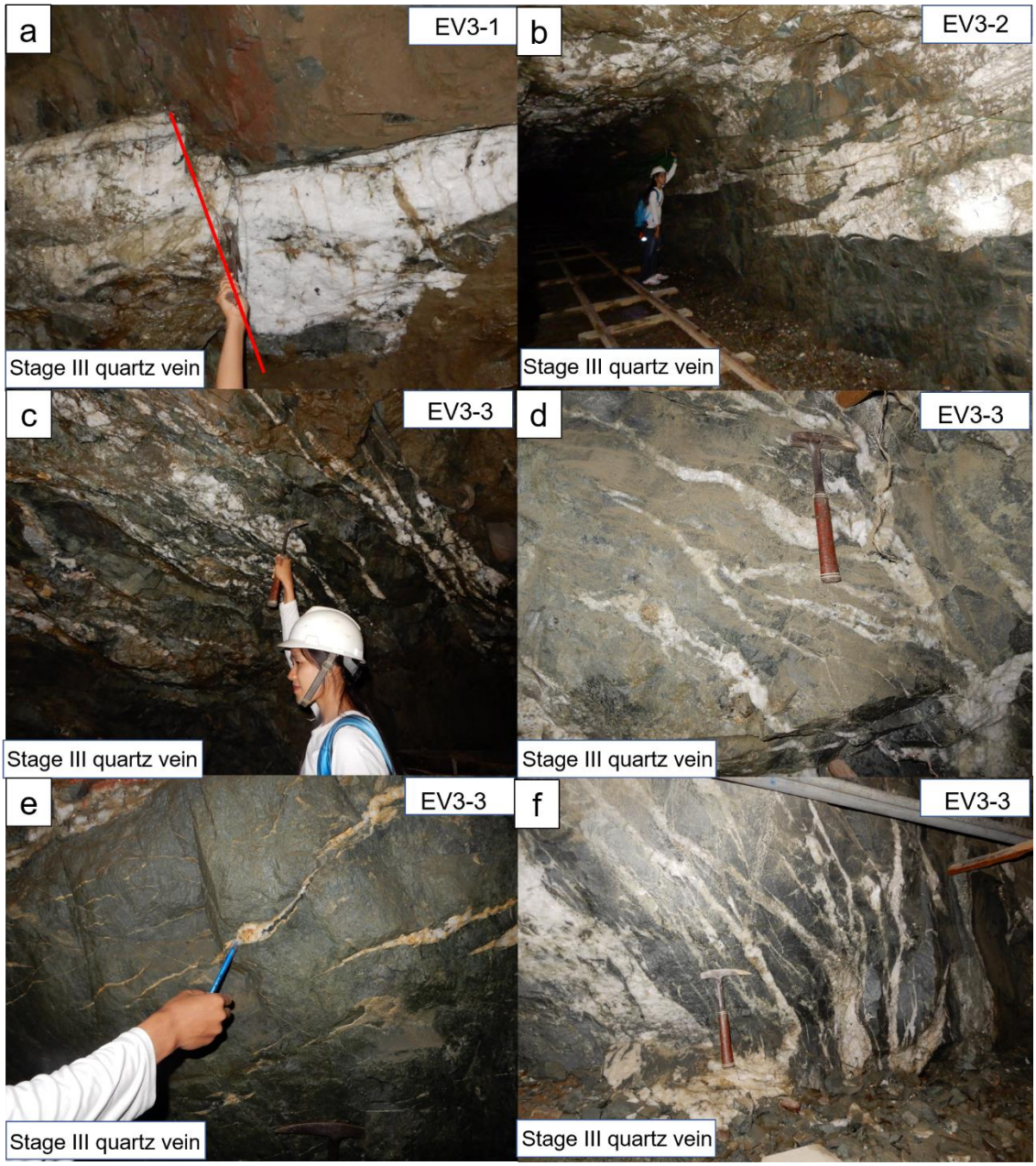

Figure 5.4 (a) photographs showing vein offset due to the fault movement of the Stage-III quartz vein EV3-1, (b) nature of gold-bearing quartz-sulfide vein and extension vein hosted by andesite of the Stage-III quartz vein (EV3-2), (c, d, e, f) the ore veins are found as the lens-shaped or pinch and swelling structure.

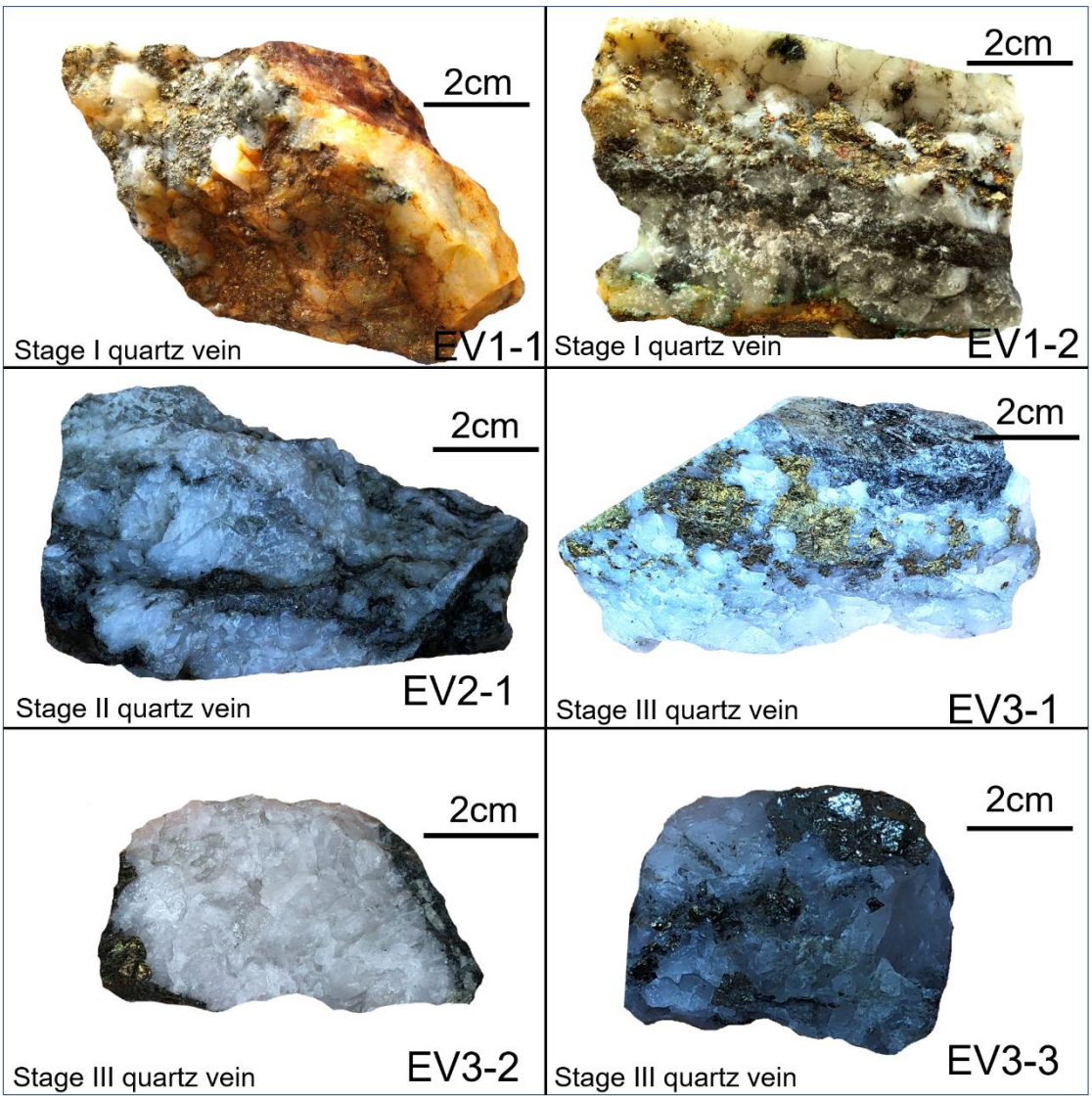

Figure 5.5 (a, b) Photographs showing nature of sulfide-bearing quartz of the Stage-I quartz vein (EV1-1, EV1-2), (c) nature of sulfide-bearing quartz of the Stage-II quartz vein (EV2-1), (d, e, f) nature of sulfide-bearing quartz of the Stage-III quartz vein (EV3-1), (EV3-2), (EV3-3).

5.3 Ore Mineralogy and Paragenesis

The sulfide ores in the mineralized quartz veins consist dominantly of pyrite and pyrrhotite, with significant amounts of chalcopyrite and sphalerite. Pyrite is the most abundant metallic mineral in the EE3 Prospect.

5.3.1 Sulfide Minerals

Sulfide-bearing quartz veins are presented in Figure 5.6a (EV1-1), 5.7a (EV1-2), 5.8a (EV1-3) of Stage-I, Figure 5.9a (EV2-1) for Stage-II and Figure 5.10a (EV3-1), 5.11a (EV3-2), 5.12a (EV3-3) for Stage-III vein. Pyrite is the most abundant sulfide mineral. It occurs as euhedral to anhedral forms and is replaced by chalcopyrite. Large pyrite crystals occur in the Stage-I quartz- carbonate-sulfide vein (Figure 5.6b, c, d). Chalcopyrite in the Stage-I veins usually coexists with native gold which fills the margin of chalcopyrite (Figure 5.7b, c, d).

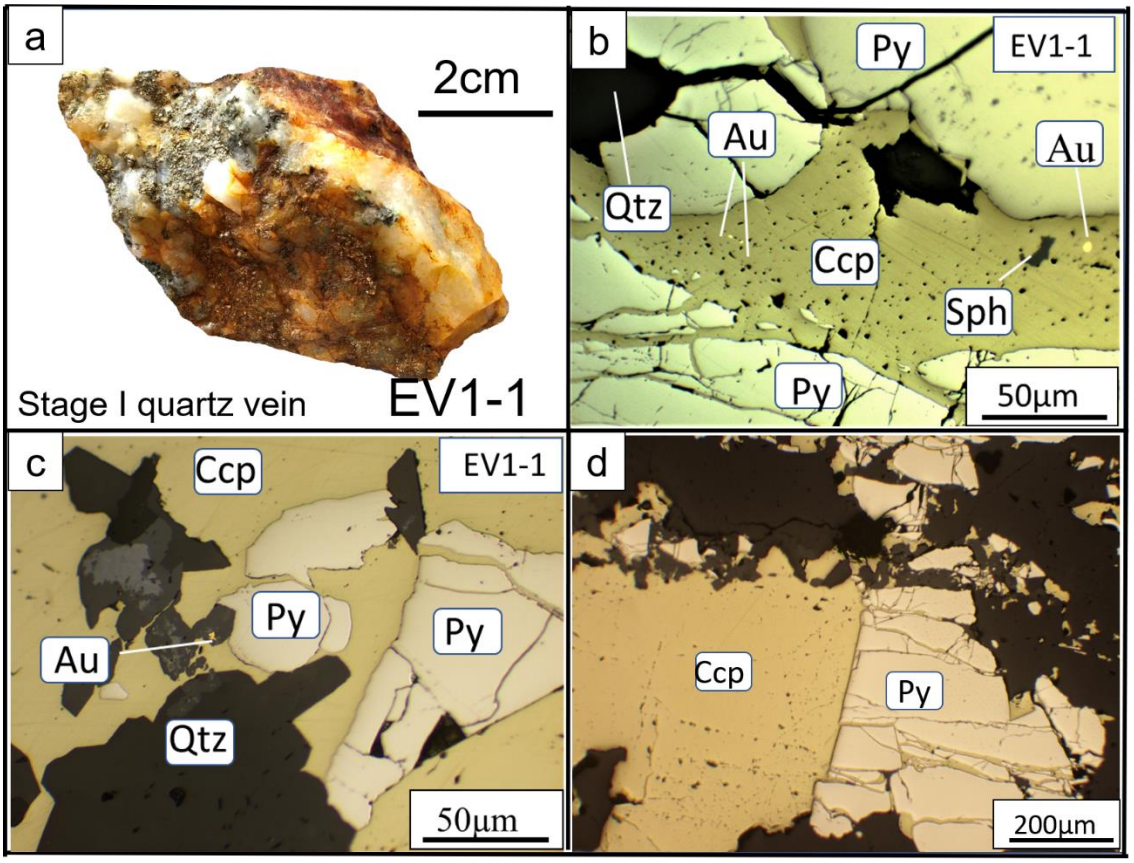

Figure 5.6 Photographs and photomicrographs showing ore and ore minerals from the EE3 Prospect. (a) Hand sample of quartz-sulfide Stage-I vein (Sample ID; EV1-1), (b) Native gold associated with chalcopyrite, sphalerite in the quartz-sulfide Stage-I vein (Sample ID; EV1-1), (c, d) Chalcopyrite replaced pyrite in the quartz-sulfide Stage-I vein (Sample ID; EV1-1). Abbreviations: Py=pyrite, Ccp=chalcopyrite, Sph=sphalerite, Au=native gold, Qtz=quartz.

In some places, pyrite crystals exhibit pitted appearance in the Stage-I quartz-carbonate-sulfide vein (Figure 5.6b, 5.8c). Chalcopyrite is common in the Stage-I quartz-carbonate-sulfide vein. It is replaced to pyrite, and sometimes aggregated with sphalerite and electrum (Figure 5.6b, c, d). That suggests that pyrite was formed earlier than other sulfide minerals.

Sphalerite is associated with the pyrite in the quartz-carbonate-sulfide veins (Figure 5.8b). Sphalerite is the principal zinc ore mineral and one of the most common base-metal sulfides in the Stage-I quartz- carbonate -sulfide veins. Sphalerite is closely associated with chalcopyrite and pyrite in the quartz-carbonate-sulfide veins. The grain size of sphalerite is variable, and most of the individual grains are anhedral; some are elongated. Representative chemical composition of sulfide minerals of the EE3 prospect are shown in Table 5.1, which are determined by EDS. Pyrite occurs as inclusion in the carbonate minerals in the Stage-II carbonate-quartz vein (Figure 5.9b, c). In the Stage-III quartz veins, chalcopyrite hosts petzite, calaverite and tellurobismuthite (Figure 5.10b, c, d, 5.11b, c, d, 5.12b, c, d). Native gold and chalcopyrite occur as filling fissure in the pyrite crystals in the Stage-III quartz veins (Figure 5.11b, c).

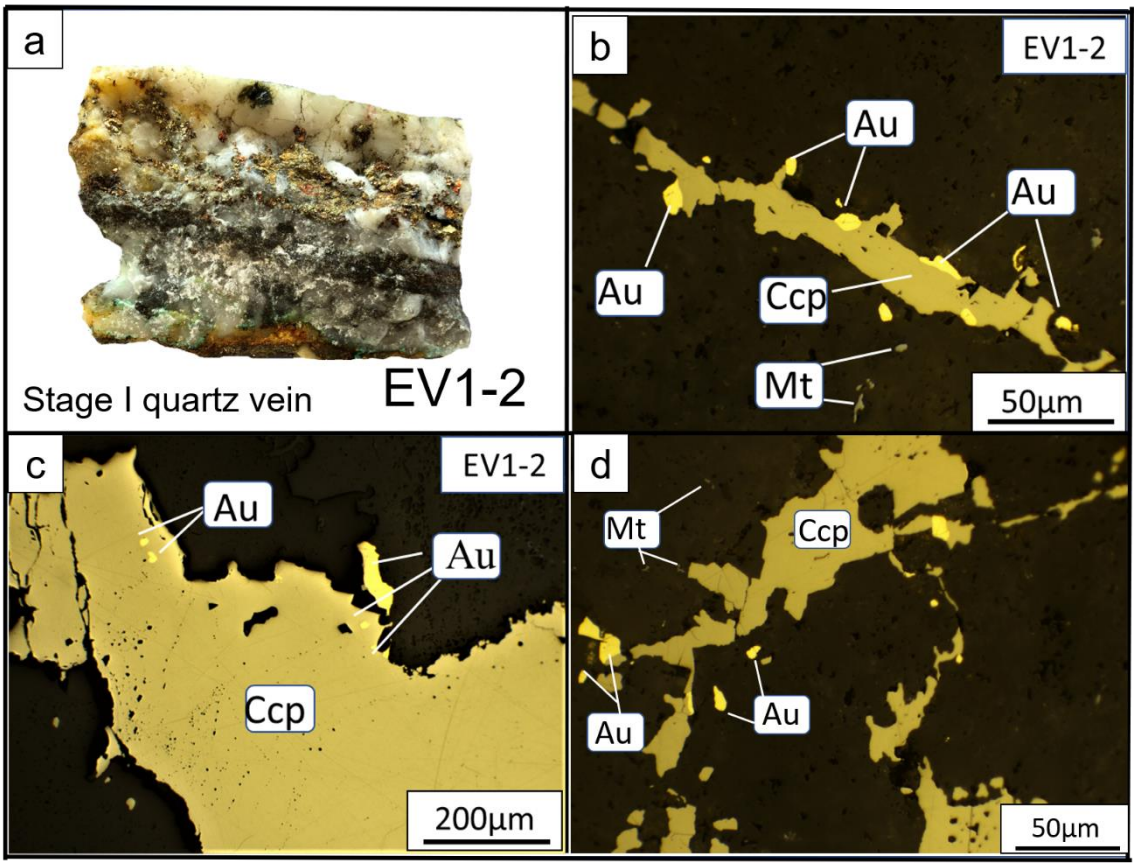

Figure 5.7 Photographs and photomicrographs showing ore and ore minerals from the EE3 Prospect. (a) Hand sample of sulfide bearing quartz vein of Stage-I quartz vein (Sample ID; EV1-2), (b, c, d) Native gold fills the margin of chalcopyrite and isolated magnetite of the quartz-sulfide Stage-I vein (Sample ID; EV1-2). Abbreviations: Py=pyrite, Ccp=chalcopyrite, Au= native gold, Qtz=quartz, Mt=magnetite.

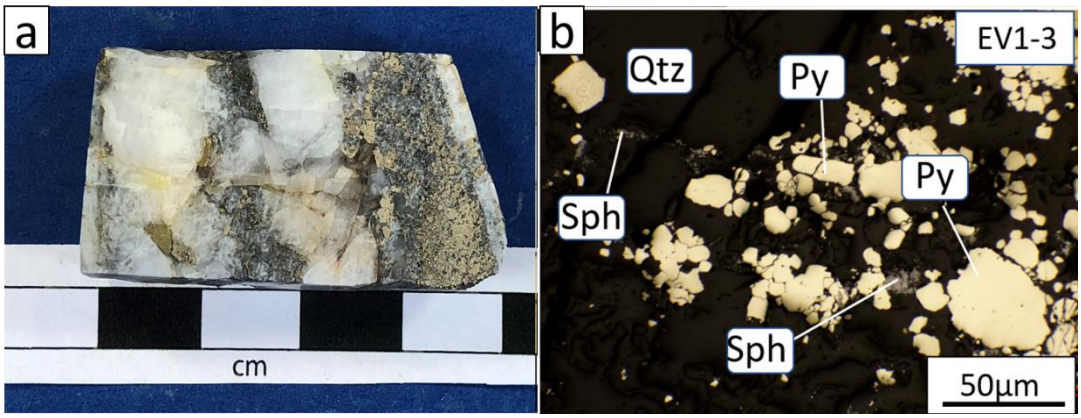

Figure 5.8 (a) Hand sample of sulfide bearing quartz vein of the Stage-I quartz vein (Sample ID; EV1-3), (b) sphalerite is associated with pyrite, small pyrite disseminated in the quartz-carbonate-sulfide veins (EV1-3). Abbreviations: Py=pyrite, Sph=sphalerite

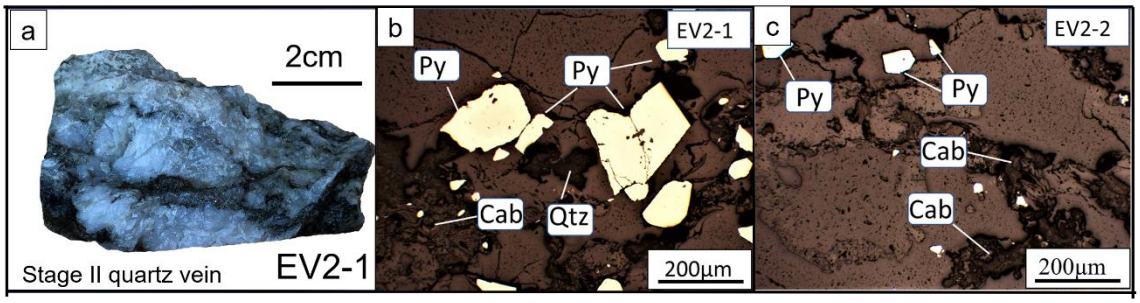

Figure 5.9 Hand sample of the Stage-II quartz vein (Sample ID; EV2-1), (b, c) Pyrite inclusion in carbonate-quartz vein of the Stage-II (Sample ID; EV2-1, EV2-2). Abbreviations: Py=pyrite, Qtz= quartz, Cab=carbonate.

5.3.2 Telluride Minerals

All the telluride minerals are confined in the Stage-III gold-bearing quartz veins. Three telluride minerals occur: Bi telluride (tellurobismuthite), Ag+Au tellurides (petzite), and Au Telluride (calaverite). Tellurobismuthite often coexists with pyrite, chalcopyrite, magnetite, calaverite and quartz. Tellurobismuthite occurs as inclusions in chalcopyrite (Figure 5.10b, d, 4.21c). Petzite is present as minute grains as inclusions in chalcopyrite (Figure 5.10c). Calaverite is the most abundant gold-bearing telluride. Calaverite also occurs as inclusions in pyrite in the Stage-III vein (Figure 5.11c, d, 5.12b). In the Stage-III veins gold-bearing telluride are more abundant than native gold. Based on EDS analysis the composition of the telluride minerals is listed in Table 5.2.

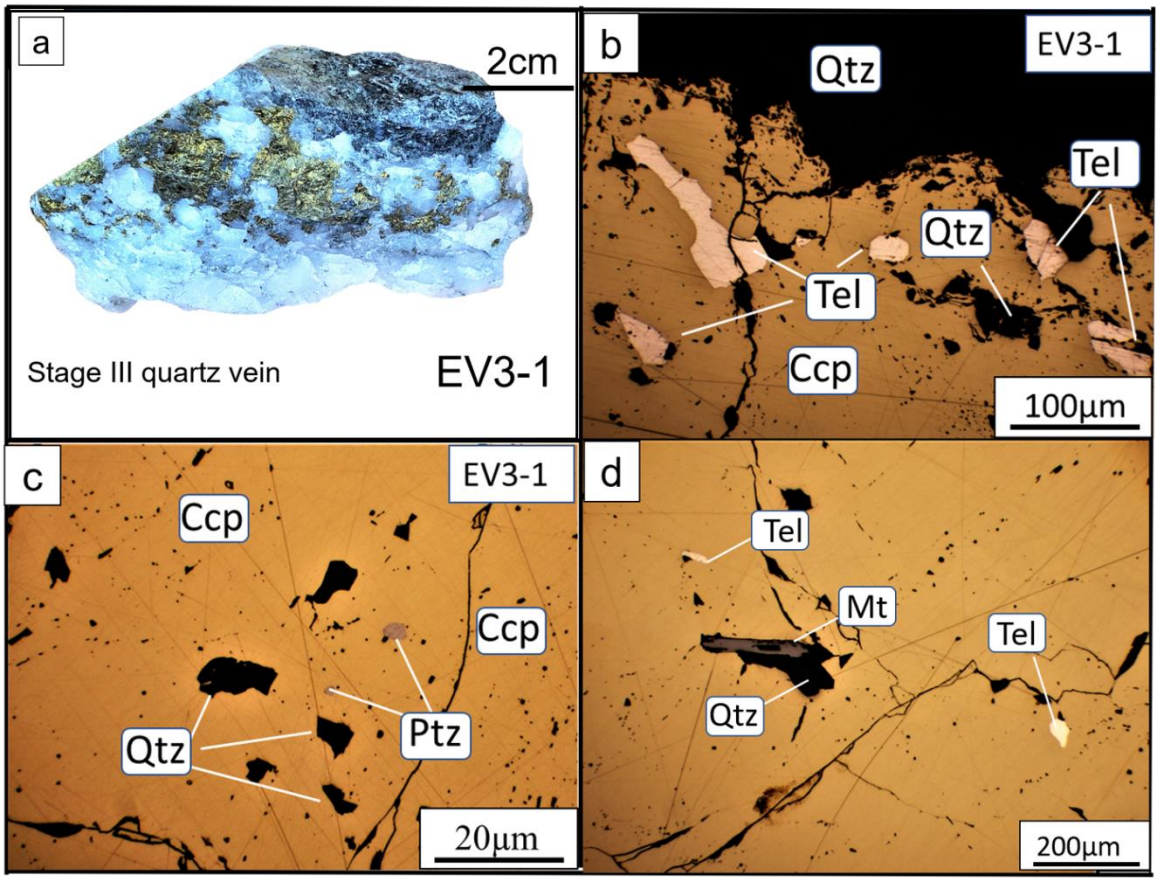

Figure 5.10 (a) Hand sample of sulfide-bearing quartz vein of the Stage-III quartz vein (Sample ID; EV3-1), (b) Tellurobismuthite inclusion in chalcopyrite of the Stage-III quartz vein (Sample ID; EV3-1), (c) Petzite inclusion in chalcopyrite of the Stage-III quartz vein (Sample ID; EV3-1), (d) An aggregate of magnetite, quartz and tellurobismuthite in chalcopyrite of the Stage-III quartz vein (Sample ID; EV3-1). Abbreviations: Py=pyrite, Ccp=chalcopyrite, Au=native gold, Qtz=quartz, Ptz=petzite, Mt=magnetite, Tel=tellurobismuthite, and Cav=calaverite.

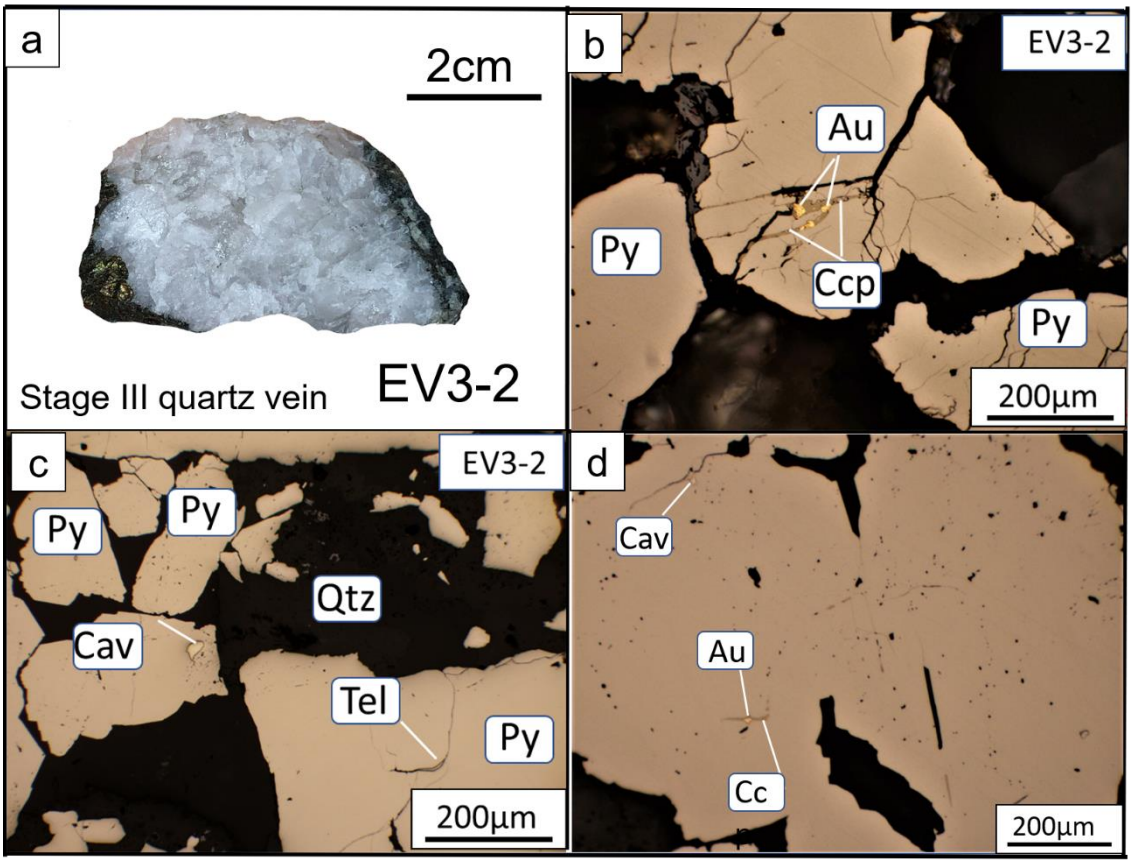

Figure 5.11 (a) Hand sample of sulfide-bearing quartz vein of the Stage-III quartz vein (Sample ID; EV3-2), (b) Native gold aggregate with pyrite and chalcopyrite of the Stage-III quartz vein (Sample ID; EV3-2), (c) Calaverite and tellurobismuthite aggregate with pyrite of the Stage-III quartz vein (Sample ID; EV3-2), (d) Native gold aggregate with chalcopyrite that inclusion in pyrite and calaverite inclusion in pyrite of the Stage-III quartz vein (Sample ID: EV3-2). Abbreviations: Py=pyrite, CCp=chalcopyrite, Au=native gold, Qtz=quartz, Tel=tellurobismuthite, and Cav=calaverite.

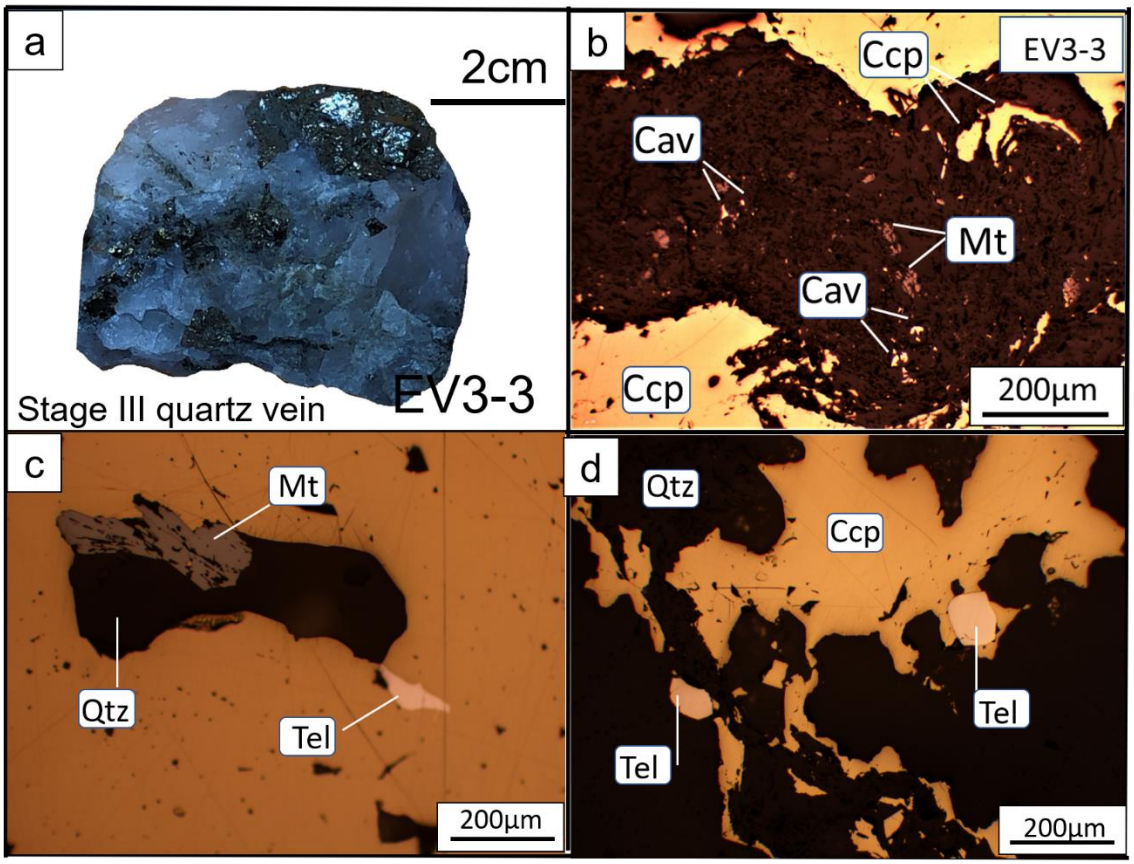

Figure 5.12 (a) Hand sample of sulfide-bearing quartz vein of the Stage-III quartz vein (Sample ID; EV3-3), (b) An aggregate of magnetite, quartz and calaverite inclusion in chalcopyrite of the Stage-III quartz vein (Sample ID; EV3-3), (c) An aggregate of magnetite, quartz and tellurobismuthite inclusion in chalcopyrite of the Stage-III quartz vein (Sample ID; EV3-3), (d) tellurobismuthite occur associate with chalcopyrite in the Stage-III quartz vein (Sample ID; EV3-3). Abbreviations: Py=pyrite, Ccp=chalcopyrite, Sph=sphalerite, Au=native gold, Po=pyrrhotite, Qtz=quartz, Ptz=petzite, Mt=magnetite, Tel=tellurobismuthite, Cab=carbonate and Cav=calaverite.

Table 5.1 Representative chemical compositions of sulfide minerals from the EE3 prospect.

Mineral Name & Formula	Samples ID	Stages	Zn	Cu	Fe	S	O	Total	Zn	Cu	Fe	S	O	Total
			(wt%)						(at%)					
Sphalerite	EV1-1	Stage-I	64.72		2.21	33.06		100.00	48.04		1.92	50.03		100.00
Magnetite	EV1-2	Stage-I			78.07		21.93	100.00			50.49		49.51	100.00
	EV1-1	Stage-I			78.66		21.38	100.00			51.44		48.57	100.00
	EV1-1	Stage-I			79.19		2.81	100.00			52.16		47.84	100.00
	EV1-3	Stage-I			84.73		15.27	100.00			61.38		38.62	100.00
	EV1-1	Stage-I			80.91		19.09	100.00			54.83		45.17	100.00
	EV13	Stage-I			78.52		21.48	100.00			51.15		48.85	100.00
	EV1-1	Stage-I			96.36		3.64	100.00			88.35		11.65	100.00
	EV1-3	Stage-I			80.89		19.11	100.00			54.81		45.19	100.00
	EV1-2	Stage-I			75.77		24.24	100.00			47.91		52.08	100.00
	EV1-2	Stage-I			75.50		24.50	100.00			46.88		53.12	100.00
	EV1-2	Stage-I			75.94		24.06	100.00			48.55		51.85	100.00
	EV1-2	Stage-I			77.27		22.73	100.00			50.05		49.95	100.00
	EV31	Stage-III			71.42		28.58	100.00			41.72		58.28	100.00
	EV3-3	Stage-III			81.22		18.78	100.00			55.33		44.67	100.00
	EV3-3	Stage-III			80.90		19.10	100.00			54.82		45.18	100.00
	EV3-2	Stage-III			78.79		21.21	100.00			51.56		48.44	100.00
	EV3-2	Stage-III			78.36		21.64	100.00			50.92		49.08	100.00
	EV3-1	Stage-III			81.56		18.44	100.00						100.00
Chalcopyrie ($CuFeS_2$)	EV1-2	Stage-I		34.57	30.07	35.37		100.00		24.89	24.63	50.47		100.00
	EV3-3	Stage-III		34.98	30.73	34.29		100.00		25.37	25.35	49.28		100.00

Determined by EDS

Normalized to 100%

Table 5.2 Representative chemical compositions of the Au-Ag-Te-Bi bearing minerals from the EE3 prospect.

Mineral Name & Formula	Samples ID	Stages	Au	Ag	Te	Bi	Total	Au	Ag	Te	Bi	Total
					(wt%)					(at%)		
Native gold (Au)	EV1-2	Stage-I	94.15	5.85			100.00	89.80	10.20			100.00
	EV1-2	Stage-I	93.73	6.27			100.00	89.11	10.89			100.00
	EV1-2	Stage-I	93.35	6.65			100.00	88.50	11.50			100.00
	EV1-2	Stage-I	94.06	5.94			100.00	89.65	10.35			100.00
	EV1-3	Stage-I	94.48	5.52			100.00	90.35	9.65			100.00
	EV1-1	Stage-I	93.00	7.00			100.00	87.92	12.08			100.00
	EV1-1	Stage-I	94.40	5.60			100.00	90.00	10.00			100.00
	EV1-1	Stage-I	89.39	10.61			100.00	82.19	17.81			100.00
	EV1-2	Stage-I	100.00	0			100.00	100.00	0			100.00
	EV3-2	Stage-III	95.11	4.89			100.00	91.41	8.59			100.00
	EV3-1	Stage-III	94.34	5.66			100.00	90.12	9.88			100.00
Tellurobismuthite (Bi_2Te_3)	EV3-1	Stage-III			46.57	53.43	100.00			58.80	41.20	100.00
	EV3-1	Stage-III			45.98	54.02	100.00			58.23	41.77	100.00
	EV3-3	Stage-III			45.18	54.82	100.00			57.44	42.56	100.00
	EV3-1	Stage-III			46.70	53.30	100.00			58.93	41.07	100.00
	EV3-3	Stage-III			48.22	51.78	100.00			60.40	39.60	100.00
	EV3-2	Stage-III			48.14	51.86	100.00			60.32	39.68	100.00
	EV3-3	Stage-III			45.56	54.44	100.00			57.81	42.19	100.00
	EV3-1	Stage-III			46.75	53.25	100.00			58.98	41.02	100.00
	EV3-1	Stage-III			48.37	51.63	100.00			60.54	39.46	100.00
	EV3-1	Stage-III			47.39	52.61	100.00			59.60	40.40	100.00
	EV3-1	Stage-III			47.32	52.68	100.00			59.53	40.47	100.00
Calaverite ($AuTe_2$)	EV3-3	Stage-III	52.16		47.84		100.00	41.39		58.61		100.00
	EV3-2	Stage-III	54.61		45.39		100.00	65.00		35.00		100.00
	EV3-2	Stage-III	47.40		52.60		100.00	36.86		63.14		100.00
	EV3-2	Stage-III	49.10		50.90		100.00	38.46		61.54		100.00
	EV3-1	Stage-III	48.02		51.98		100.00	37.44		62.56		100.00
	EV3-2	Stage-III	49.95		50.05		100.00	39.26		60.74		100.00
	EV3-3	Stage-III	51.98		48.02		100.00	41.22		58.78		100.00
	EV3-3	Stage-III	48.93		51.07		100.00	38.30		61.70		100.00
	EV3-3	Stage-III	54.29		45.71		100.00	64.71		35.29		100.00
	EV3-3	Stage-III	47.37		52.63		100.00	36.83		63.17		100.00
Petzite (Ag_3AuzTe_2)	EV3-1	Stage-III	15.05	41.00	43.94		100.00					100.00
	EV3-1	Stage-III	27.73	40.93	31.34		100.00	18.38	49.54	32.07		100.00
	EV3-1	Stage-III	36.80	37.24	25.95		100.00	25.40	46.94	27.65		100.00
	EV3-1	Stage-III	35.46	38.36	26.18		100.00	24.30	48.01	27.69		100.00

Determined by EDS

Normalized to 100%

5.4 Paragenesis

The hydrothermal mineralization in the EE3 Prospect can be divided into three paragenetic stages based on cross-cutting relation and overgrowth (Figure 4.22). The paragenetic stages are as follows:

The Stage-I is characterized by the main quartz-carbonate-sulfide vein, which are cut by the E-W trending veins (Stage-II). The Stage-I is the earliest sulfide-forming stage. The Stage-I veins contain pyrite, chalcopyrite, sphalerite and native gold. Native gold is mainly associated with chalcopyrite and occurs at the boundary of the chalcopyrite not only in the Stage-I veins but also in the Stage-III veins. Sphalerite formed as small particles with native gold in the Stage-I veins. Stage-II is not associated with gold mineralization. Calcite commonly occurred in this stage. Chalcopyrite is very rare during this stage.

The Stage-III is characterized by tellurobismuthite, calaverite and petzite. Tellurobismuthite often coexists with the chalcopyrite and pyrite. Tellurobismuthite and petzite occur as inclusions in chalcopyrite and calaverite occurs as inclusions in pyrite. Magnetite is associated with chalcopyrite. The Stage-III is the most important stage for tellurides and gold mineralization. The principal gangue and alteration minerals are quartz, calcite, epidote, chlorite and sericite.

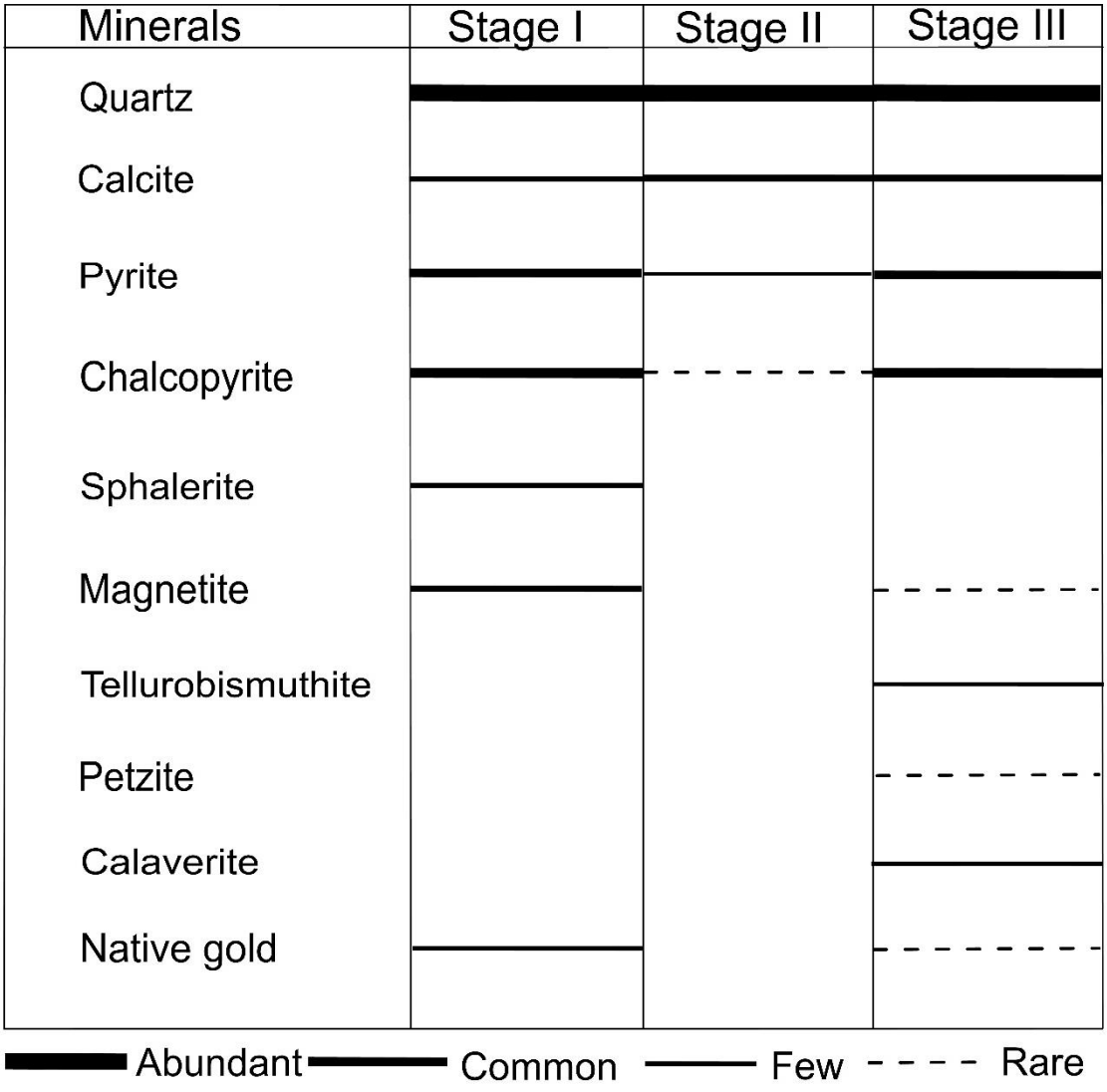

Figure 5.13 Paragenetic sequence of Stage-I quartz-carbonate-sulfide main vein, E-W trending Stage-II quartz vein and Stage-III parallel to the Stage-I main vein in the EE3 Prospect.

5.5 Conclusions

Three mineralization stages are identified at the EE3 prospect: (1) Stage-I quartz-carbonate-sulfide main veins, (2) Stage-II E-W trending veins that intersected the Stage-I main veins, and (3) Stage-III parallel to the Stage-I main veins. Stage-I veins contain pyrite, pyrrhotite, chalcopyrite, sphalerite, magnetite, electrum and native gold. Significant gold mineralization is not accompanied with the Stage-II veins. Stage-III veins are characterized by tellurobismuthite, calaverite and petzite native gold and magnetite associated with pyrite, chalcopyrite.

CHAPTER 6

FLUID INCLUSION MICROTHERMOMETRY AND SULFUR ISOTOPES

6.1 Introduction

This chapter offerings the fluid inclusion study in quartz with different stages to clarify ore forming fluid and sulfur isotope analysis in order to understand about source of mineralized fluid at the EE3 gold prospect.

6.2 Fluid Inclusion Petrography

Fluid inclusions in the auriferous quartz veins of the EE3 Prospect were examined in this study. The fluid inclusions are petrographically classified as primary and secondary in origin based on the criteria provided by Roedder (1984). Those fluid inclusions aligned along growth zones in intragranular crystals were interpreted as primary inclusions (Figure 6.1.a). Fluid inclusions occurring as isolated inclusions, random distributions, or in clusters are also categorized as primary inclusions (Figure 6.1b, c).

The secondary fluid inclusions occur along transgranular healed fractures and were avoided during subsequent microthermometric analysis. The shapes of fluid inclusions are variable, and include spheroidal, irregular, polygonal, rounded, sub-rounded and elongated. The size of fluid inclusion varies from 5 μm to 30 μm in diameter. According to the phases observed at room temperature, fluid inclusions from the EE3 Prospect were classified into three types.

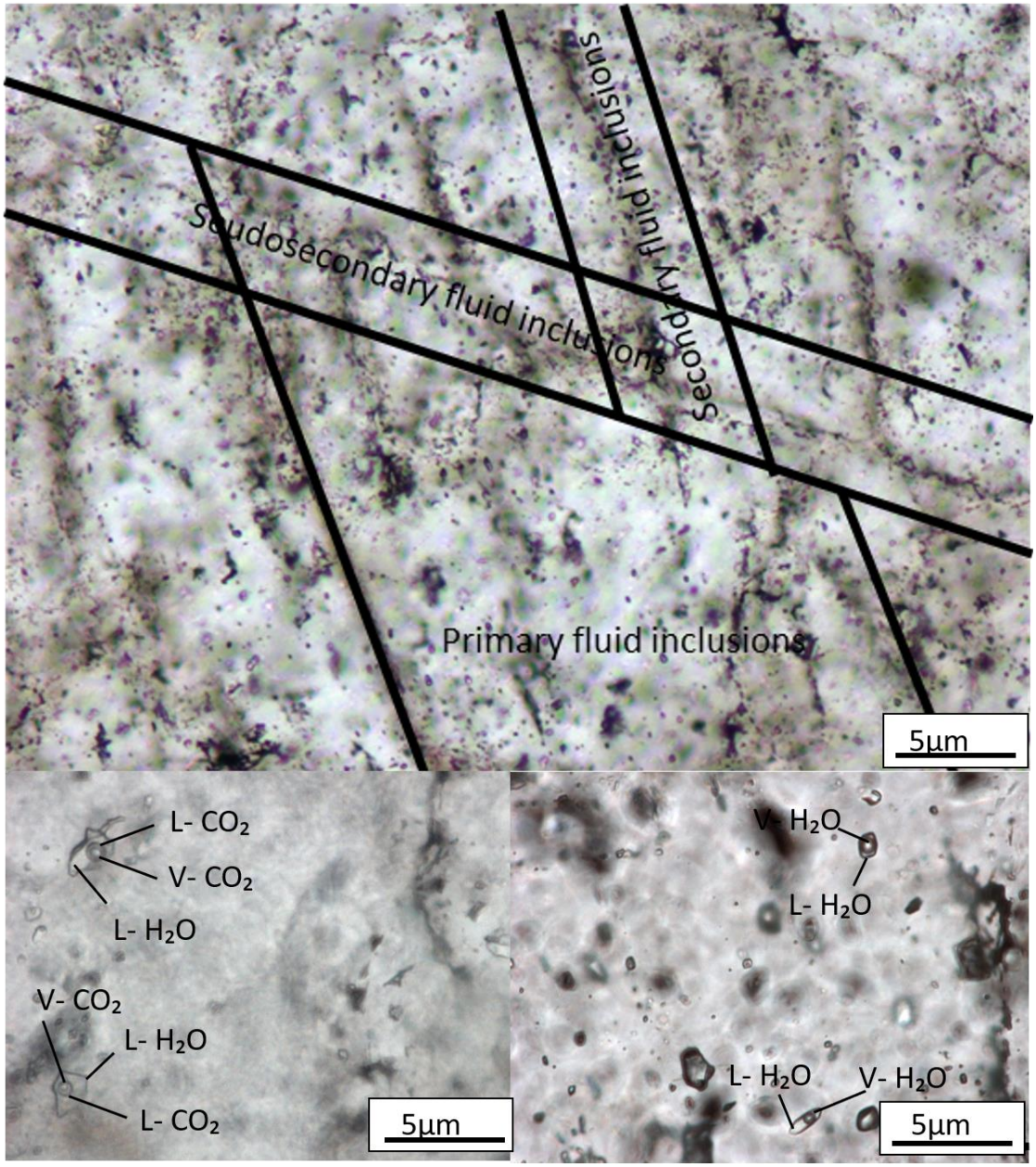

Figure 6.1 Fluid inclusion petrography of mineralized quartz veins at the EE3 prospect. (a) Fluid inclusions are distributed in clusters, in isolation and along growth zones as a primary and fluid inclusions are in healed fractures as a secondary fluid in quartz veins of Stage-III quartz vein (EV3-1), (b) Three phase fluid inclusions are found as rounded and sub-rounded inclusions in the mineralized quartz vein in volcanic rocks of Stage-I quartz vein (Sample ID; EV1-1), (c) Two phase fluid inclusions are observed as tabular, elongated, rounded and sub-rounded inclusions in the mineralized quartz in volcanic rocks of Stage-III quartz vein (Sample ID; EV3-2).

Type A: two phases, liquid-dominated, liquid (L) + vapor (V) inclusions.

Type B: two phases, vapor-dominated (>60%), vapor + liquid inclusions.

Type C: three phases, aqueous liquid + carbonic liquid + carbonic vapor inclusions.

Type A in Stage-I, II and III: Fluid inclusions are liquid-dominated two phases (L+V) at room temperature. This type of fluid inclusions is very common in quartz grains in the quartz-sulfide veins of the EE3 Prospect. The shape of the Type A fluid inclusions includes ellipsoidal or irregular with sizes ranging from 5 μm to 30 μm. The proportion of the vapor bubble is 20-35 vol % (Figure 6.2b, c, d, 6.3b, c, 6.4b, c, d). Type A inclusions coexist with Type B, Type C inclusions within a same quartz crystal in the Stage-I (Figure 6.2b, c, d) and Type A inclusions coexist with Type B in the Stage-II (Figure 6.3b, c) and Stage-III veins (Figure 6.4b, c, d).

Type B in Stage-I, II and III: This type of fluid inclusions is vapor-dominated, two phases (V+L) containing 60-98 vol % vapor in inclusion at room temperature. This inclusion type occurs as isolated inclusions, clusters and as aggregates of inclusions in the mineralized veins (Figure 6.2b, c, d, 6.3b, c, d, 6.4b, c, d). Type B inclusions coexist with Type A inclusions within a same quartz crystal in the Stage-II (Figure 6.3b, c) and Stage-III (Figure 6.4b, c, d). In the Stage-I, Type B inclusions coexist with Type C within a same quartz crystal (Figure 6.2b, c, d).

Type C in Stage-I vein: At room temperature, this type of fluid inclusions comprises three phases (aqueous + carbonic liquid + carbonic vapor), with the volume of the CO_2 phase varying widely from 40 % to 80 % (Figure 6.2b, c, d). The shape of the Type C fluid inclusions includes ellipsoidal or irregular shapes with sizes ranging from 10 μm to 30 μm. They were observed only in Stage-I quartz vein. Type C inclusions coexist with Type A and Type B inclusions in a same quartz crystal in the Stage-I veins (Figure 6.2b, c, d).

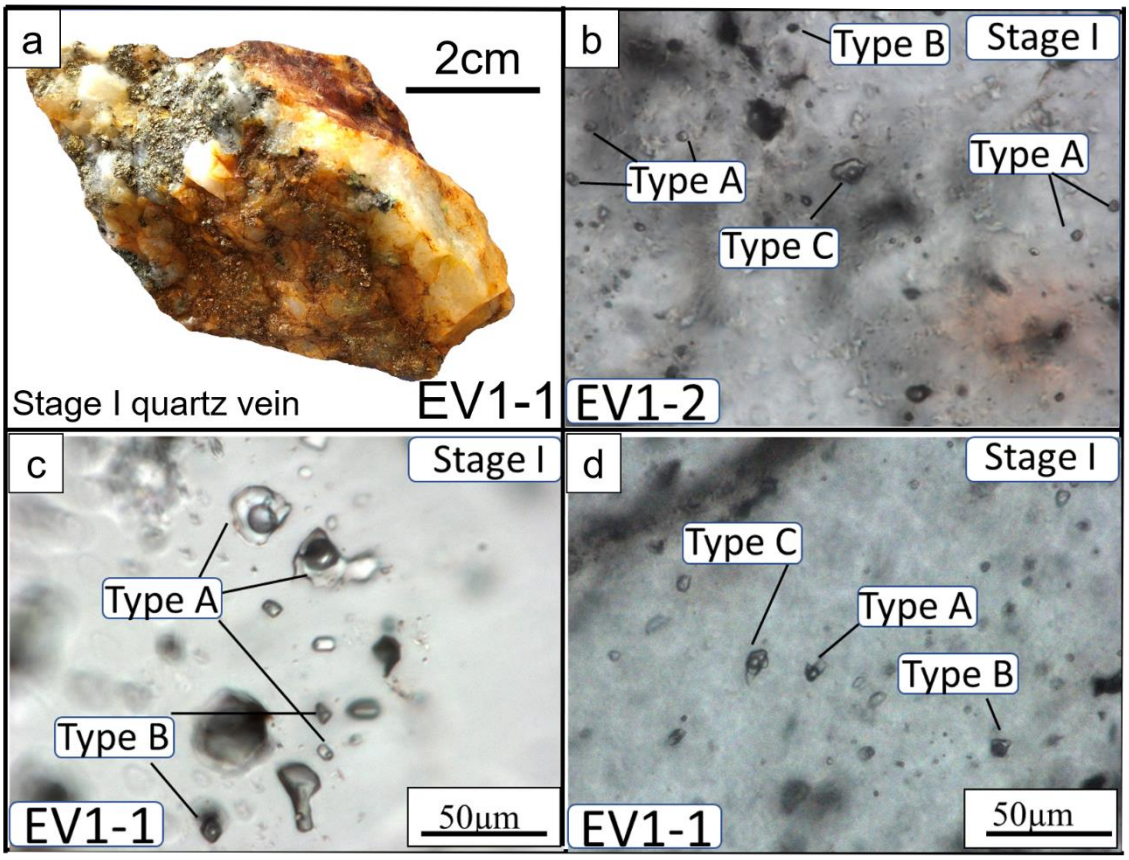

Figure 6.2 Photographs of mineralized Stage-I quartz veins and photomicrographs of fluid inclusion types of the EE3 gold prospect (a) Sulfide-bearing quartz vein in volcanic rock (EV1-1), (b, d) Type A, Type B and Type C coexisting together within a small area in the mineralized Stage-I vein (Sample ID; EV1-2, EV1-2, EV1-1), (c) Type A and Type B fluid inclusions coexisting together within a small area in the Stage-I quartz vein (Sample ID; EV1-1).

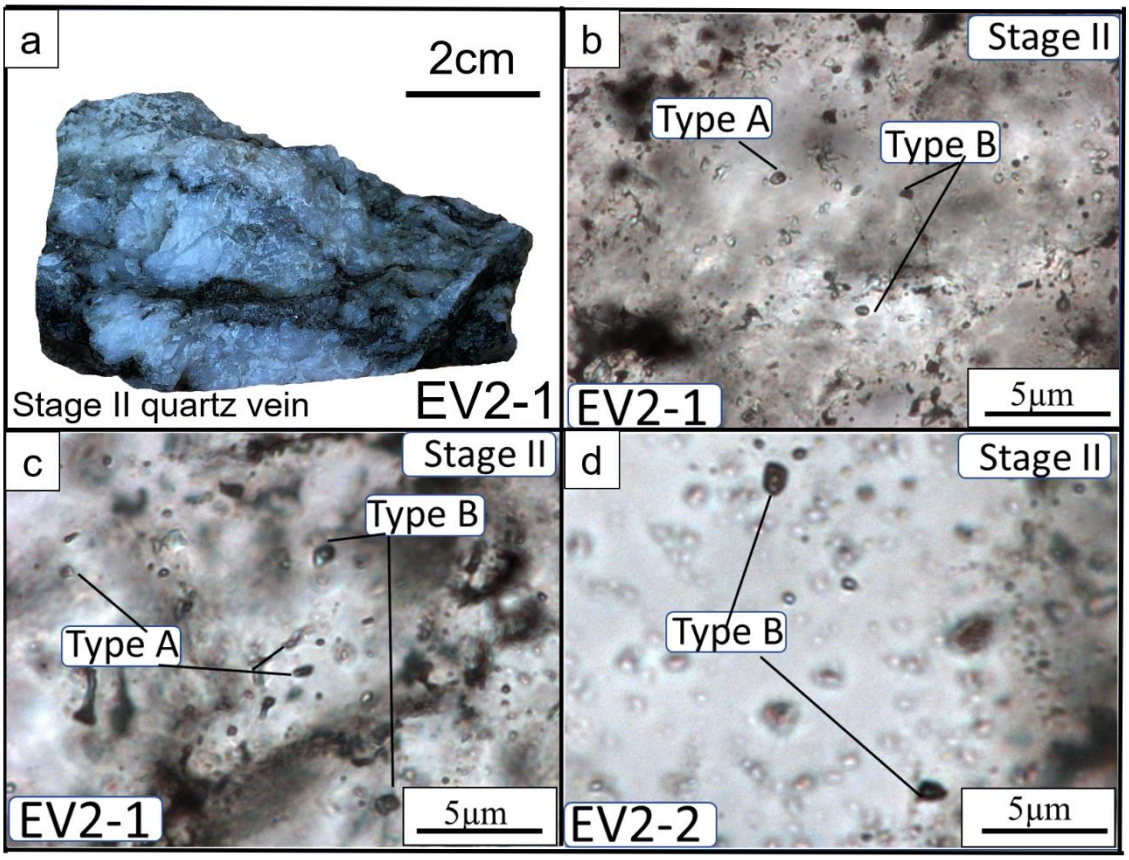

Figure 6.3 Photographs of not mineralized Stage-II quartz vein and photomicrographs of fluid inclusion types of the EE3 gold prospect. (a) Hand specimen of quartz carbonate vein in volcanic rock (EV2-1), (b, c) Type A and Type B fluid inclusions coexisting together within a small area in the Stage-II quartz carbonate vein (Sample ID; EV2-1), (d) Type B fluid inclusion in Stage-II quartz vein (Sample ID; EV2-2).

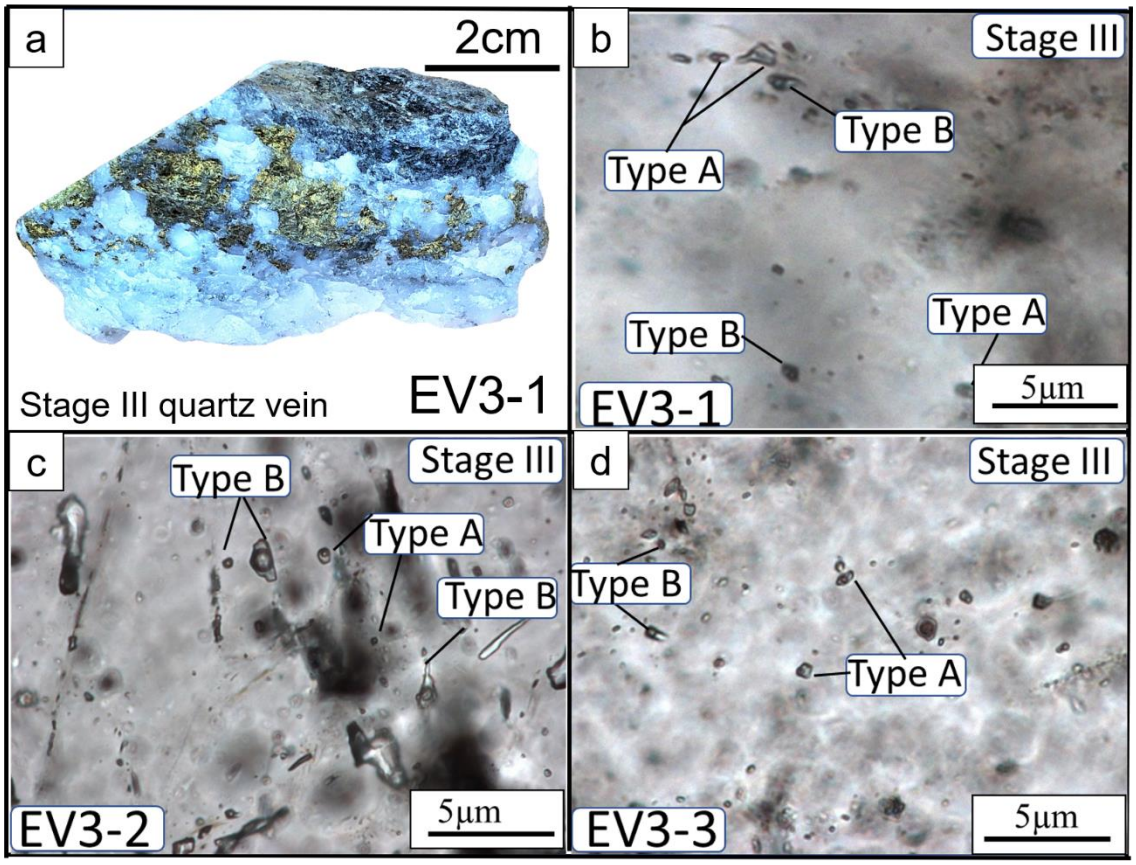

Figure 6.4 Photographs of mineralized Stage-III quartz veins and photomicrographs of fluid inclusion types of the EE3 gold prospect. (a) Sulfide-bearing quartz vein in volcanic rock (EV3-1), (b, c, d) Type A, Type B coexisting together within a small area in the mineralized Stage-III quartz vein (Sample ID; EV3-1, EV3-2, EV3-3).

6.3 Microthermometry

The result of fluid inclusion microthermometry are summarize in Table 6.1.

Table 6.1 Summary of fluid inclusion types and microthermometric data of the fluid inclusions in the EE3 prospect.

Sample No	Type veins	Type	T_m-CO_2 (°C)	$T_{m\text{-}cla}$ (°C)	T_h-CO_2 (°C)	T_h (°C)	T_m-ice (°C)	Salinity	FI (N)
EV1-1	Stage-I quartz vein	Two-phase Type A				260-362	-0.2 to -5.7	0.3 to 8.8	25
		Two-phase Type B				348-430	-0.3 to -3.8	0.5 to 6.2	8
		Three-phase Type C	-56 to -58	6.0 to 9.4	28.1 to 30.9	220-356		1.2 to 7.4	10
EV1-2	Stage-I quartz vein	Two-phase Type A				180-260	-0.5 to -6.0	0.9 to 9.2	12
		Two-phase Type B				315-346	-1.4 to -4.0	2.4 to 6.4	4
		Three-phase Type C	-56 to -58	5.8 to 7.9	28.0 to 30.6	280-310		4.1 to 7.8	5
EV2-1	Stage-II quartz vein	Two-phase Type A				176-387	-0.9 to -5.7	1.7 to 8.8	21
		Two-phase Type B				292-436	-2.1 to 7.5	3.5 to 11.1	15
EV2-2	Stage-II quartz vein	Two-phase Type A				200-320	-1.5 to -5.0	2.6 to 7.9	11
		Two-phase Type B				287-425	-2.4 to -6.7	4.3 to 10.1	9
EV3-1	Stage-III quartz vein	Two-phase Type A				196-340	-0.3 to -5.9	0.5 to 9.1	14
		Two-phase Type B				290-450	-0.7 to -6.6	1.2 to 9.9	14
EV3-2	Stage-III quartz vein	Two-phase Type A				158-313	-3.8 to -7.1	6.2 to 10.6	13
		Two-phase Type B				278-464	-0.9 to -7.5	1.6 to 11.1	23
EV3-3	Stage-III quartz vein	Two-phase Type A				177-335	-0.3 to -5.3	0.5 to 8.3	11
		Two-phase Type B				310-359	-2.1 to -3.3	3.6 to 5.4	4

Notes: Tm-CO_2= melting temperature of CO_2; $T_{m\text{-}cla}$= melting temperature of CO_2 clathrate; T_h-CO_2= partial homogenization of CO_2 inclusions; T_h= Total homogenization temperature of inclusions; T_m-ice= final ice melting temperature; N= total number of fluid inclusions.

6.3.1 Stage-I Vein

Two samples from two different veins in the same stage were analyzed. Type A, Type B and Type C fluid inclusions are found in quartz of the Stage-I veins. Homogenization temperatures (T_h) of Type A fluid inclusions of Stage-I vein quartz range from260 ° to 362 °(N=25) (EV1-1) and 180 °C to 260 °C (N=12) (EV1-2) and their mode of temperature are 300-320 °C (Figure 6.5a). Their final ice melting temperatures (T_m-ice) range from -6.0 °C to -0.2 °C (EV1-1), -6.0 °C to -0.5 °C (EV1-2) that correspond to salinities from 0.3 to 8.8 wt. % NaCl equiv (EV1-1), 0.9 to 9.2 wt. % NaCl equiv (EV1-2), (Figure 6.5b). Homogenization temperatures (T_h) of Type B fluid inclusions in quartz vein range from 348 °C to 430 °C (N=8) (EV1-1), 315 °C to 346 °C (N=4) (EV1-2), their mode temperature are 340-360 °C (Figure 6.5c).

Their final ice melting temperatures (T_m-ice) vary from -3.8 °C to -0.3 °C (EV1-1), -4.0 °C to -1.4 °C (EV1-2) which correspond to salinities between 0.5 and 6.2 wt. % NaCl equiv (EV1-1), 2.4 and 6.4 wt. % NaCl equiv for EV1-2 (Figure 6.5d). Total homogenization temperatures (T_h) of Type C fluid inclusions range from 220 °C to 356 °C (EV1-1) (N=10), 280 °C to 310 °C (EV1-2), their mode temperature are 280-320 °C (Figure 6.5e).

The melting temperatures of clathrate (T_m-clath) of Type C fluid inclusions range from +6.0 °C to +9.4 °C (EV1-1), +5.8 °C to +7.9 °C (EV1-2) corresponding to salinities ranging from 1.2 to 7.4 wt. % NaCl equiv (EV-1), 4.1 to 7.8 wt. % NaCl equiv in the Stage-I veins (Figure 6.5f). The CO_2 melting temperatures (T_m-CO_2) of fluid inclusions range from -58 °C to -56 °C for EV1-1 and EV1-2 (Figure 6.6a), suggesting that the carbonic phase is dominated by CO_2 with only minor components of other volatiles (Zou et al., 2017). The partial homogenization temperatures (T_h-CO_2) of CO_2 phase, mostly

homogenizing into the liquid phase, range from +28.1 °C and +30.9 °C (EV1-1), +28.0 °C and +30.6 °C (EV1-2) (Figure 6.6b).

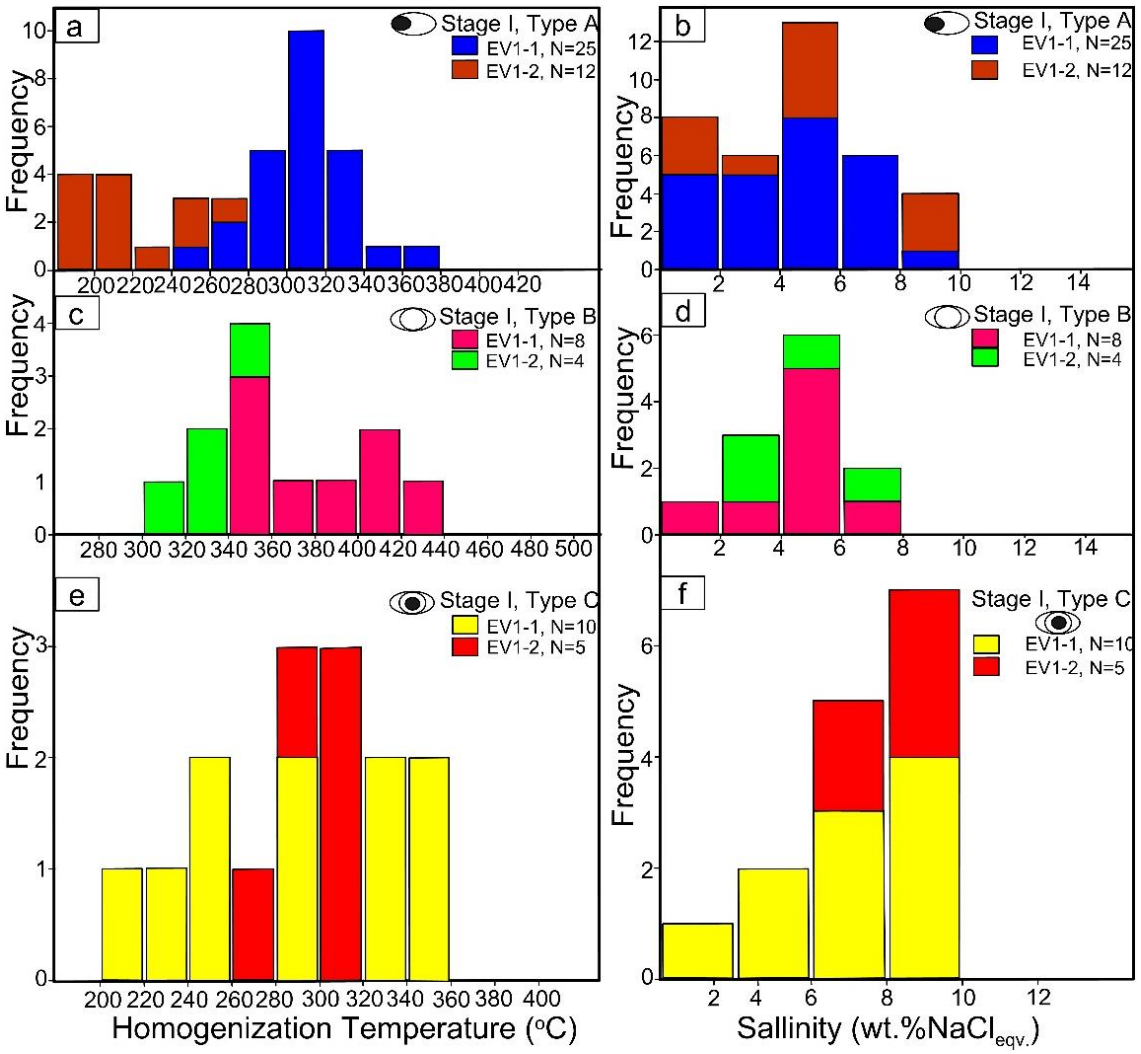

Figure 6.5 Histograms of total homogenization temperatures (T_h) of primary inclusions and salinities of fluid inclusions in Stage-I quartz-sulfide vein from EE3 Prospect, (a) Homogenization temperature of Type A fluid inclusions in Stage-I quartz-sulfide vein, (b) Salinity of Type A fluid inclusions from Stage-I quartz-sulfide vein, (c) Homogenization temperature of Type B fluid inclusions from Stage-I quartz-sulfide vein, (d) Salinity of Type B fluid inclusions from Stage-I quartz-sulfide vein, (e) Homogenization temperature of Type C fluid inclusion from Stage-I quartz-sulfide vein, and (f) Salinity of Type C fluid inclusion from Stage-I quartz-sulfide vein.

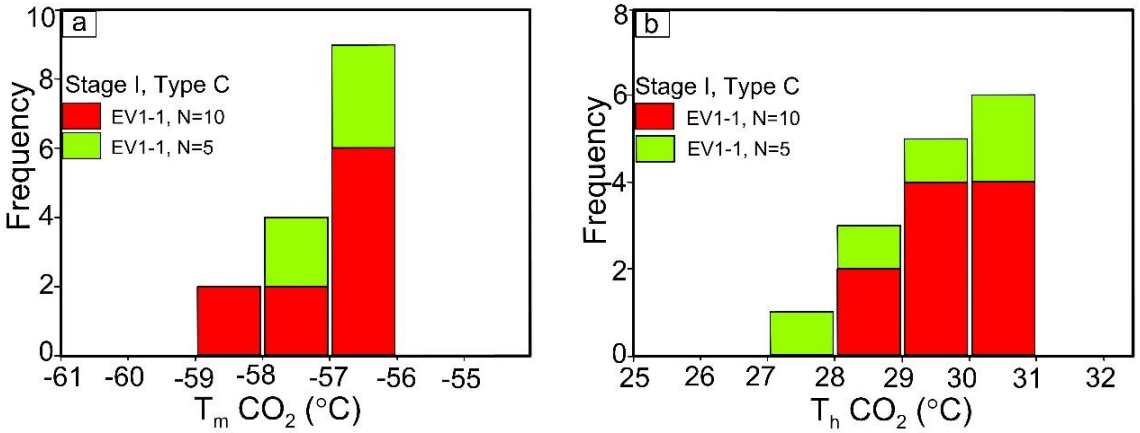

Figure 6.6 Summary of the microthermometric characteristics of the carbonic phase in aqueous-carbonic inclusion (Type C). (a) Temperature of melting of solid CO_2, and (b) Temperature of partial homogenization for CO_2.

6.3.2 Stage-II Vein

Two samples of quartz veins in the same stage were analyzed. Type A and Type B fluid inclusions are found in quartz of the Stage-II veins. Homogenization temperatures (T_h) of Type A fluid inclusions range from 176 °C to 387 °C (N=21) (EV2-1), 200 °C to 320 °C (N=11) (EV2-1), their mode at temperature are 300-320 °C (Figure 6.7a). Their final ice melting temperatures (T_m-ice) range from -5.7 °C to -1.0 °C for EV2-1, -5.0 °C to -1.5 °C for EV2-2 with corresponding salinities range from 1.7 to 8.8 wt. % NaCl equiv for EV2-1, 2.6 to 7.9 wt. % NaCl equiv for EV2-2 (Figure 6.7b).

The homogenization temperatures of the Type B fluid inclusions mainly range from 292 °C to 436 °C (N=15) for EV2-1, 287 °C to 425 °C (N=9) for EV2-2, their mode at temperature are 420 °C-440 °C (Figure 6.7c). Their final ice melting temperatures (T_m-ice) vary from -7.5 °C to -2.1 °C (EV2-1), -6.7 °C to -2.4 °C (EV2-2) with salinities ranging from 3.5 to 11.1 wt. % NaCl equiv for EV2-1, 4.3 to 10.1 wt. % NaCl equiv for EV2-2 (Figure 6.7d).

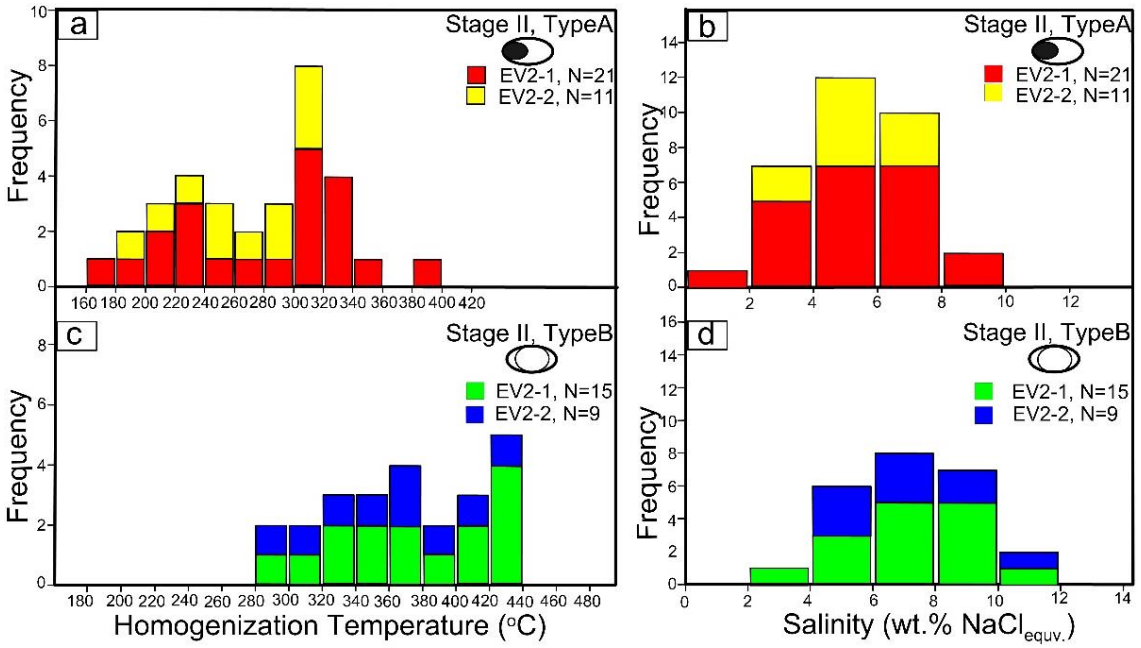

Figure 6.7 Histograms of total homogenization temperatures (T_h) of primary inclusions and salinities of fluid inclusions in Stage-II quartz vein from EE3 Prospect. (a) Homogenization temperature of Type A fluid inclusions in Stage-II quartz vein, (b) Salinity of Type A fluid inclusions from Stage-II quartz vein, (c) Homogenization temperature of Type B fluid inclusions from Stage-II quartz vein, and (d) Salinity of Type B fluid inclusions from Stage-II quartz vein.

6.3.3 Stage-III Vein

Three samples were collected from two different veins in same stage. Type A and Type B fluid inclusions are found in quartz of the Stage-III veins. Homogenization temperatures (T_h) of Type A fluid inclusions of quartz vein range from 196 °C to 340 °C (N=14) (EV3-1), 158 °C to 313 °C (N=13) (EV3-2), 177 °C to 335 °C (N=11) (EV3-3), their mode at temperature are 200-220 °C (Figure 6.8a). Their final ice melting temperatures (T_m-ice) range from -5.9 °C to -0.3 °C (EV3-1), -7.1 °C to -3.8 °C (EV3-2), -5.3 °C to -0.3 °C (EV3-3) with corresponding salinities from 0.5 to 9.1 wt. % NaCl equiv (EV3-1), 6.2 to 10.6 wt. % NaCl equiv (EV3-2), 0.5 to 8.3 wt. % NaCl equiv (EV3-3) (Figure 6.8b).

Homogenization temperatures (T_h) of Type B fluid inclusions Stage-III quartz vein range from 290 °C to 450 °C (N=14) (EV3-1), 278 °C to 464 °C (N=23) (EV3-2), 310 °C to 359 °C (N=4) (EV3-3), their mode at temperature are 340-360 °C (Fig. 6.8c). Their final ice melting temperatures (T_m-ice) vary from -6.6°C to -0.7°C (EV3-1), -7.5°C to -0.9°C (EV3-2), -3.3 °C to -2.1°C (EV3-3) which correspond to salinities between 1.2 and 9.9 wt. % NaCl equiv (EV3-1), 1.6 and 11.1 wt. % NaCl equiv (EV3-2), 3.6 and 5.4 wt. % NaCl equiv (EV3-3) (Figure 6.8d).

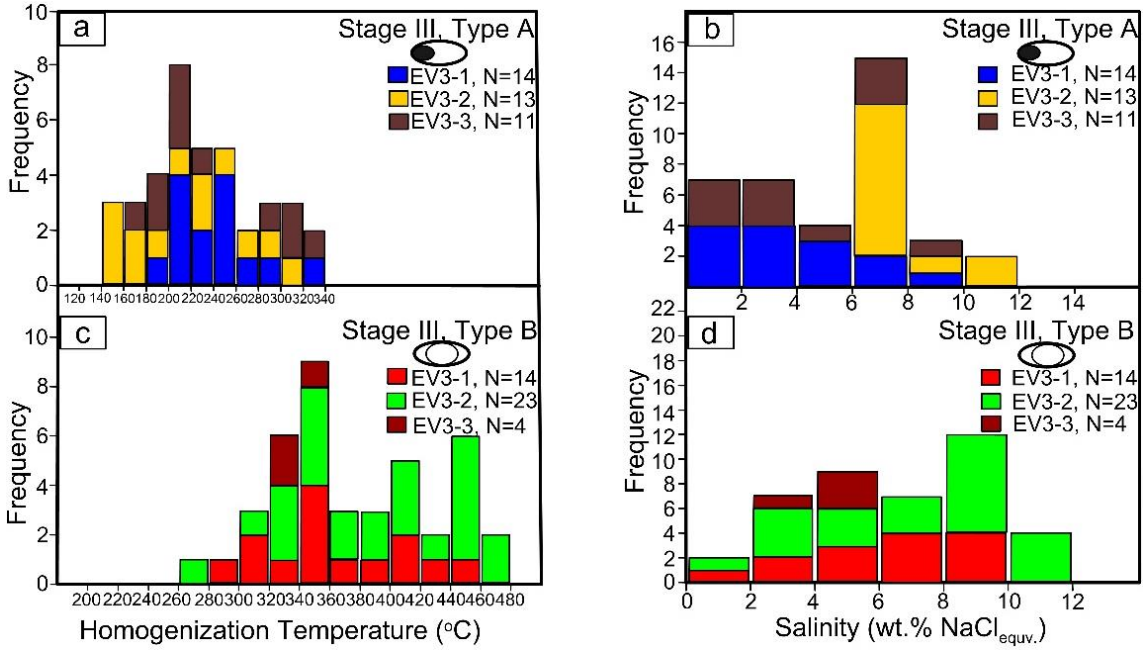

Figure 6.8 Histograms of total homogenization temperatures (T_h) of primary inclusions and salinities of fluid inclusions in Stage-III quartz vein from EE3 Prospect. (a) Homogenization temperature of Type A fluid inclusions in Stage-III quartz vein, (b) Salinity of Type A fluid inclusions from Stage-III quartz vein, (c) Homogenization temperature of Type B fluid inclusions from Stage-III quartz vein, and (d) Salinity of Type B fluid inclusions from Stage-III quartz veins.

6.3.4 Sulfur Isotopes

The $\delta^{34}S$ values of nine pyrite grains of Stage-I quartz veins of the EE3 Prospect range from -3.0 ‰ to +0.5 ‰ (Figure 6.9a) and the $\delta^{34}S$ values of nine pyrite samples of Stage-III quartz veins of the EE3 Prospect range from -2.4 % to -1.1 % (figure 6.9b). The

determined $\delta^{34}S$ values are summarized in Table 6.2 and shown in histograms (Figure 6.9a, b). The range of $\delta^{34}S$ values of the EE3 Prospect is a very narrow restricted range, with a unimodal distribution.

6.4 Discussions

6.4.1 Source of Sulfur

The bulk sulfur isotopic composition of the fluids can be interpreted from the $\delta^{34}S$ values of sulfides by assuming the absence of sulfate. There are three major reservoirs on earth, with different sulfur isotopic compositions: (a) mantle or magmatic (0 ‰ ± 3 ‰); (b) seawater (+20 ‰, present as SO_4^{2-}), and (c) reduced sulfur or biogenic sulfur in sedimentary rocks, characterized by $\delta^{34}S < 0$ ‰ (Hoefs, 1975). In this study, the $\delta^{34}S$ values of the sulfides narrowly range from -3 ‰ to +0.5 ‰, indicating a restricted sulfur source assuming the absence of sulfate (Figure 6.9a, b). These values are similar to the $\delta^{34}S$ values of sulfides in most magmatic hydrothermal deposits (-3 ‰ to +1 ‰; Hoefs, 2009). The range of sulfur isotope values of the EE3 prospect is also plotted in Figure 6.10.

The narrow range of $\delta^{34}S$ values of the sulfides near ±0‰ suggests a magmatic source, which can be interpreted to reflect either a leaching of sulfur from the andesite rocks that hosted the mineralization at the EE3 Prospect, or direct supply of sulfur from a magma chamber at depth. It is difficult to distinguish the sulfur derived from the volcanic rocks through water-rock interactions from that derived from a magma at depth.

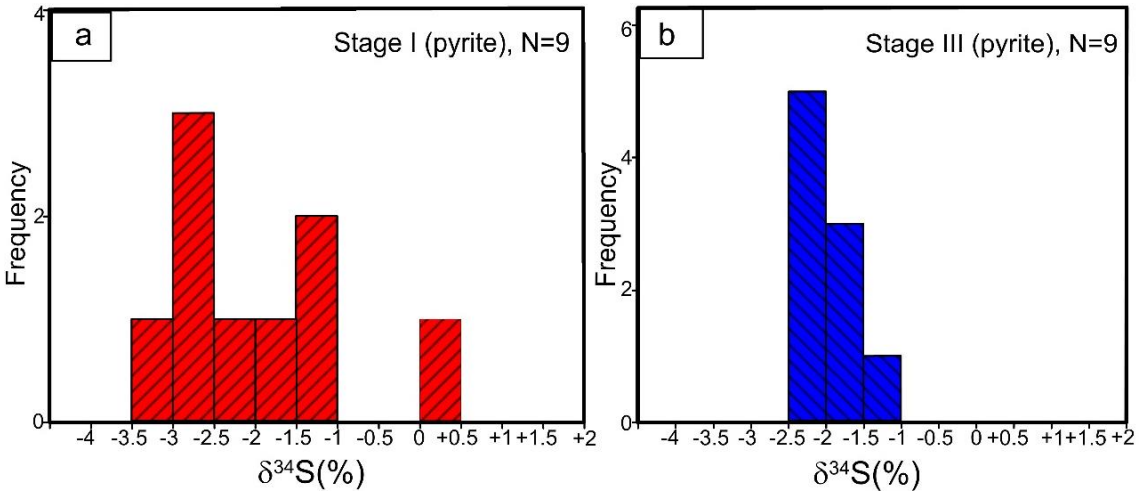

Figure 6.9 (a, b) Histograms showing variation of sulfur isotopic ratios of pyrite the EE3 Prospect, Banmauk district, Myanmar.

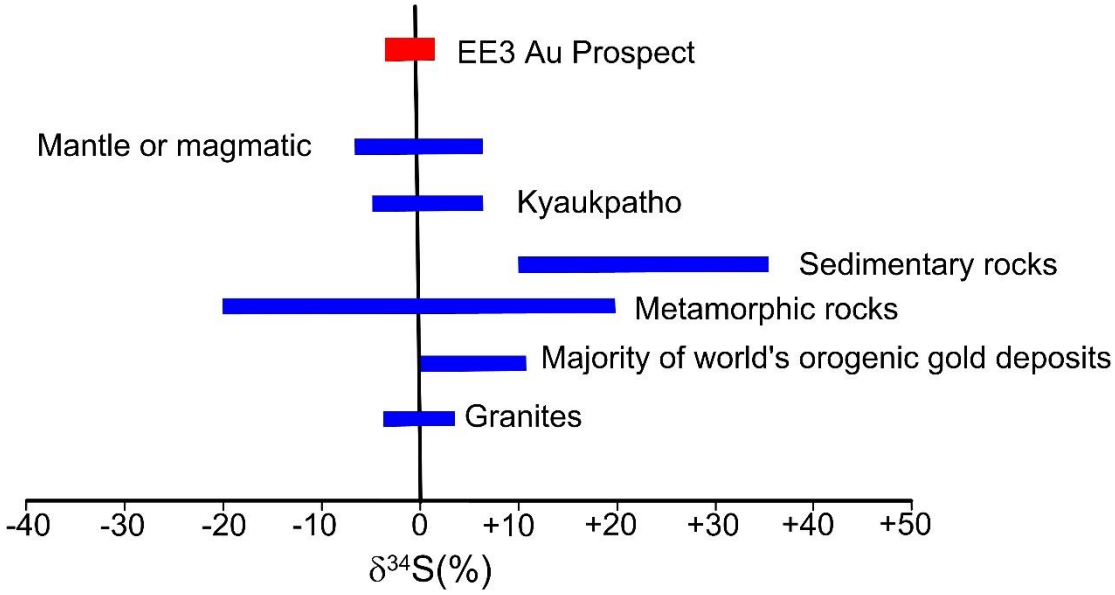

Figure 6.10 Sulfur isotopic compositions of the EE3 prospect compared with other deposits. Natural geological settings: metamorphic rocks, sedimentary rocks and granites Hoef (2004). Sedimentary rock-hosted Kyaukpatho gold deposit in Kawlin-Wuntho area (Khin Zaw, 2008).

Table 6.2 Sulfur isotope compositions of the sulfides from the EE3 Prospect.

Sample No	Mineral	Stage	$\delta^{34}S(\%)$
EV1-1	Pyrite	I	+0.5
EV1-2	Pyrite	I	-2.9
EV1-3	Pyrite	I	-1.4
EV1-4	Pyrite	I	-2.8
EV1-5	Pyrite	I	-3.0
EV1-6	Pyrite	I	-1.8
EV1-7	Pyrite	I	-2.3
EV1-8	Pyrite	I	-1.4
EV1-9	Pyrite	I	-2.6
EV3-1	Pyrite	III	-2.1
EV3-2	Pyrite	III	-2.2
EV3-3	Pyrite	III	-2.4
EV3-4	Pyrite	III	-2.3
EV3-5	Pyrite	III	-2.2
EV3-6	Pyrite	III	-1.7
EV3-7	Pyrite	III	-1.1
EV3-8	Pyrite	III	-1.6
EV3-9	Pyrite	III	-1.6

6.4.2 Immiscibility/Boiling of Ore-Forming Fluids

Based on the fluid inclusion petrography and microthermometry, three different types of fluid inclusions are recognized in the Stage-I veins: aqueous liquid-rich fluid inclusions (Type A), aqueous vapor-rich fluid inclusions (Type B), and aqueous-carbonic fluid inclusions (Type C). CO_2-rich fluid inclusions (Type C) coexist with the Type A and Type B aqueous inclusions in the same fluid inclusion assemblage. This suggests that

the Type A, Type B and Type C inclusions were trapped at the same time (Bodnar et al.,1985; Ramboz et al., 1982), and might represent the ore-forming fluid of the Stage-I quartz-carbonate-sulfide vein in the EE3 Prospect. The coeval occurrence of liquid-rich, vapor-rich aqueous inclusions and CO_2-rich inclusions, and the absence of any positive correlation between the homogenization temperatures and salinities (Figure 6.11a) suggest heterogenous entrapment of these fluids, which is an evidence of fluid immiscibly.

Fluid immiscibility in the Stage-I veins is also supported by the fact that the liquid-rich fluids are characterized by higher salinity values than the CO_2-rich fluids, as the escape of gases during the fluid separation leads to an increase in the salinity of the residual aqueous fluid (e.g., Collins, 1979). Assuming boiling condition or fluid immiscibility, the approximate entrapment temperature is interpreted to be the minimum homogenization temperature of these fluids, which in this case corresponds to 180 °C for the Stage-I veins. Thus, the Stage-I ore-forming fluids in the EE3 Prospect is interpreted to be low to intermediate temperature and low salinity fluid, belonging to H_2O-NaCl-CO_2 system, which separated into low density CO_2-bearing fluid and high-density H_2O-NaCl fluid due to the decrease of pressure and temperature that led to fluid immiscibility (e.g., Diamond, 1990; Mikucki, 1998; Klein et al., 2008).

From fluid inclusion petrography and microthermonmetry, two different types of fluid inclusions consisting of liquid-rich fluid inclusion (Type A) and vapor-rich fluid inclusion (Type B) are recorded in the Stage-II quartz veins. The coexistence of Type A fluid inclusions and Type B fluid inclusions in the same quartz grains in the Stage-II vein is also interpreted as an evidence for fluid immiscibility. Plotting of the fluid inclusions data on a salinity and homogenization temperature (Th) diagram is shown in Figure 6.11b. This diagram shows different homogenization temperature and similar salinity of fluid inclusions, whereas homogenization temperature of Type B is higher than Type A

because the purer end-member inclusions (70–95% VH_2O Type B inclusions) rather than 15–50% VH_2O Type A inclusions) were trapped at lower temperatures, which is consistent with fluid immiscibility (Roedder, 1984). Pure water or water-salt systems, production of a vapor phase can occur as a result of temperature increase, pressure decrease, or a combination of these (e.g., Roedder, 1984).

As for the Stage-III, high homogenization temperatures (peaking at 300 °C to 360 °C) and salinities (peaking at 6 to 10 wt. % NaCl equiv) were yielded. The coexistence of two different types of fluid inclusions, liquid-rich fluid inclusions (Type A) and vapor-rich fluid inclusions (Type B) in the same fluid inclusion assemblage (Figure 6.4b, c, d), the apparent skewness of homogenization temperature histograms to higher temperatures (Figure 6.8a, b, c), and the absence of any correlation between the homogenization temperatures and salinities (Figure 6.11c), suggest that the fluid immiscibility was the main fluid entrapment mechanism in the Stage-III quartz vein, same as in the Stage-I vein.

Total homogenization temperatures of the Type A inclusions (Figure 6.5), implying that the heterogenous trapping of a small amount of H_2O-rich fluid by Type B inclusions. Thus, the obtained apparent homogenization temperatures are higher than the actual trapping temperature (Wilkinson, 2001). Type A inclusions show slightly higher salinities (mode at 6-8 wt.% NaCl equiv for the three analyzed samples) than Type B inclusions (mode at 4-6 wt.% NaCl equiv mode of three sample), which is consistent with phase separation, as salt is preferentially fractionated into the aqueous phase (e.g., Lawrence et al., 2013). All these evidences indicate that fluid immiscibility or phase separation occurred in the Stage-III. Assuming boiling condition, the minimum entrapment temperature of the fluids during the Stage-II veining is estimated to be the minimum homogenization temperature which is 158 °C.

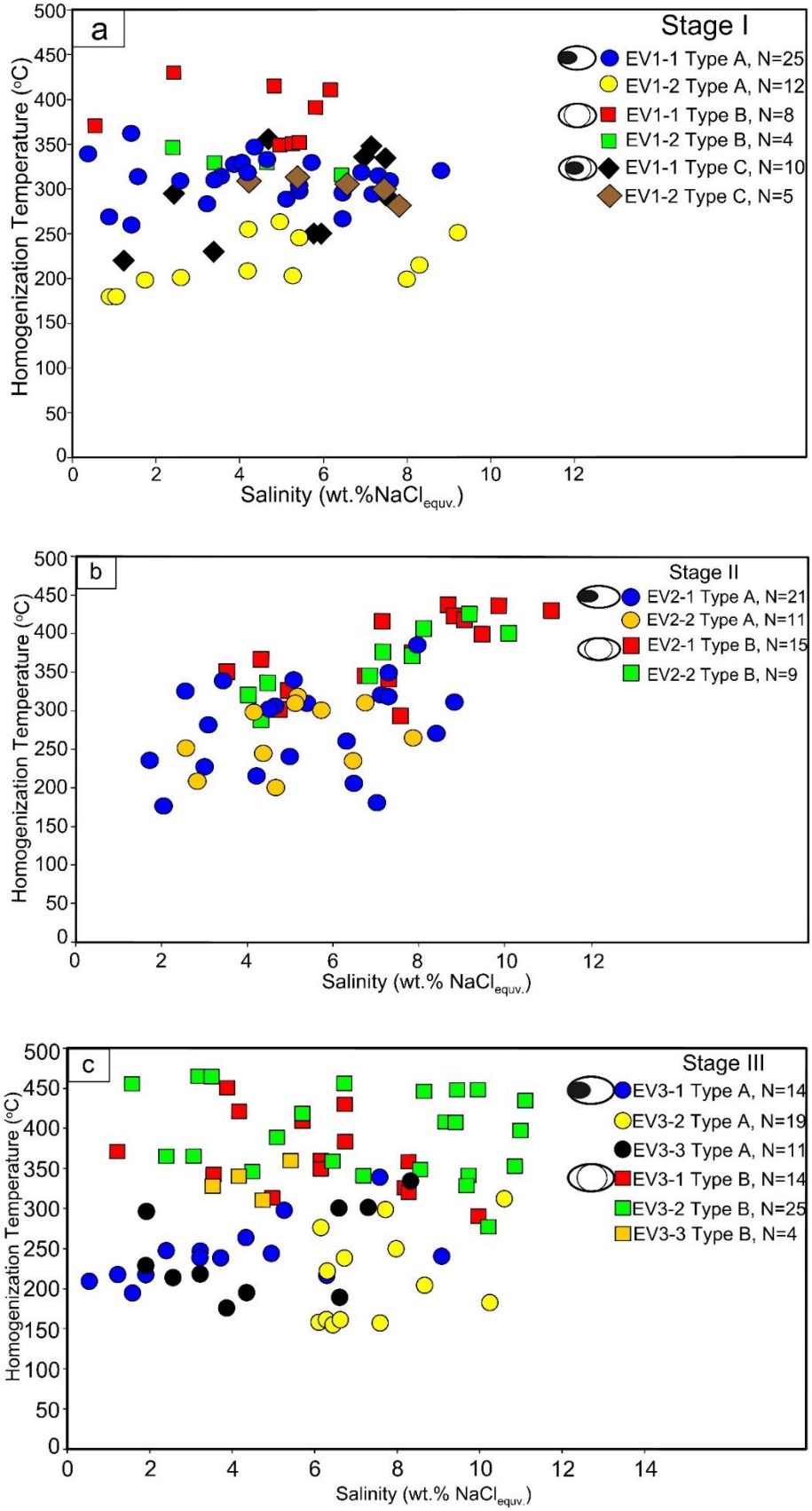

Figure 6.11 (a, b, c) Plot of homogenization temperature (Th) Vs. salinity of fluid inclusions in Stage-I, Stage-II, and Stage-III of the EE3d Prospect.

In summary, the fluid inclusions data show that the main mineralization stages in the EE3 Prospect, the Stage-I and Stage-III, are consistent with fluid immiscibility or boiling as the main fluid entrapment process. Fluid immiscibility is an important mechanism for ore deposition in several deposit types, including epithermal and mesothermal types, and is documented in several studies (e.g., Fan et al., 2003; Ramboz et al., 1982; Roedder, 1984; Sterner and Bodnar, 1984, 1991).

Phase separation processes associated with fluid unmixing are effective mechanisms associated with gold deposition in many hydrothermal systems (e.g., Hagemann and Lueders, 2003; Chai et al., 2016). Fluid immiscibility in the Stage-I and Stage-III veins could have resulted in the breakdown of gold sulfide complexes leading to the gold deposition. As a result of pressure decrease, the fluid may intersect its solvus and separate into a CO_2 -rich fluid and a saline fluid aqueous for the case of Stage-I vein.

6.4.3 Trapping Pressure and Depth of Ore Formation

The immiscible fluid inclusion assemblage in samples from the Stage-I and Stage-III of mineralization suggests that it is possible to estimate trapping temperatures and pressures. In this case, we consider the both immiscibility and boiling of fluids are similar ore-forming process in terms of phase separation of ore fluids due to pressure decrease. Hence, the immiscible fluids during the main entrapment mechanisms for the Stage-I and Stage-III are assumed to represent the minimum entrapment temperature condition of the fluids (Bodnar et al., 1985).

Based on this, the trapping temperature of hydrothermal fluids in the Stage-I, Stage-II and Stage-III veins are around 180 °C, 176 °C and 158 °C, respectively. These values were plotted along the boiling point curves of 5% wt% NaCl equivalent solution, (Haas., 1971), under hydrostatic condition (Figure 6.12). The estimated formation pressure for 180 °C (Stage-I), 176 °C (Stage-II) and 158°C (Stage-III) are 28 bars, 26 bars

and 21 bars, which correspond to formation depths of about 300 m, 260 m and 215 m, respectively (Figure 6.12).

The formation depths were calculated based on hydrostatic condition, assuming water density of 1 g/cm³ (Hass, 1971; Roedder and Bondar, 1980; Roedder, 1984). The low sulfidation epithermal deposits formed between 100 and 1000 meters below the paleowater table (Sillitoe et al., 2003; Takács et al., 2017) conforming to less than 100 bars of hydrostatic pressure. However, the presence of CO_2-bearing fluid inclusions in the early mineralized Stage-I and the structural setting in a fracture zone do not rule out a deeper condition than the common epithermal system and probably suggests a transitional environment from mesothermal to epithermal-type deposit.

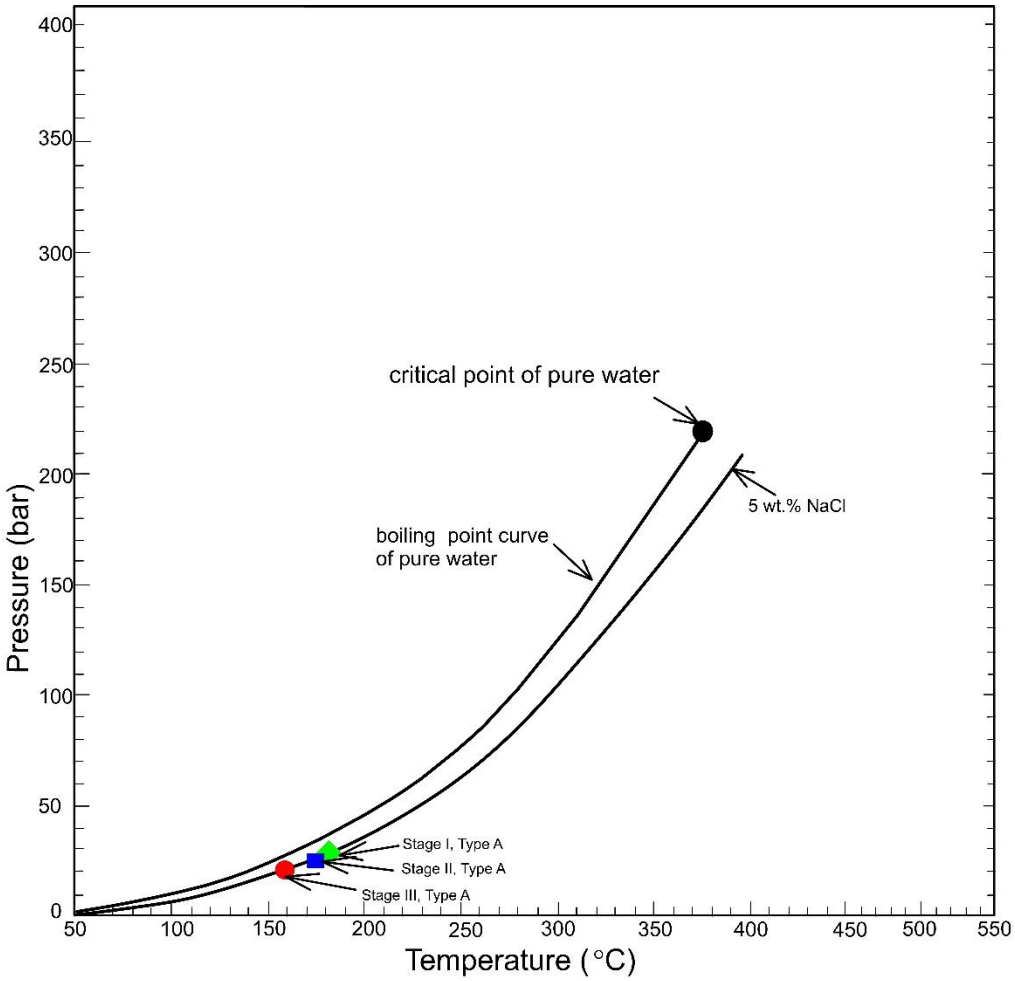

Figure 6.12 Estimated P-T conditions of formation for the indicated mineralization Stage-I, Stage-II and Stage-III. The boiling point curve originating from the critical point of pure water (Sourirajan and Kennedy, 1962).

6.5 Conclusions

The coexistence of aqueous Type A fluid inclusions, Type B fluid inclusions and CO_2-rich Type C fluid inclusions in the same quartz grains in the Stage-I veins is interpreted as an evidence for fluid immiscibility or boiling. Type A and Type B fluid inclusions of Stage-III also give fluid immiscibility features. Fluid immiscibility or boiling was possibly the key factor in the precipitation of gold and other metal sulfides.

Estimated P-T-depth condition of Stage-I is 180 °C and 28 bars which is approximately equivalent to 300 m. Estimated P-T-depth conditions of the Stage-III is 158 °C and 21 bars which is approximately equivalent to 215 m.

A narrow range of $\delta^{34}S$ values (+0.5 ‰ to -3.0 ‰) and near ±0 ‰ of sulfides of the EE3 Prospect, suggest that sulfur was most likely derived from the leaching of the volcanic rocks that hosted the mineralization or magmatic body at depth.

The ore fluids in the Stage-I and III ascended along the structural conduits within the Mawgyi Andesite and the ore deposition occurred due to decreasing in pressure and immiscibility of the ore fluids.

On the basis of the estimated temperature and pressure conditions of the mineralization in the Stage-I, Stage-II and Stage-III, presence of CO_2-bearing Type C inclusions and the sulfur isotope data, the associated ore paragenesis and alteration assemblages, the EE3 Prospect is likely to have formed in a transitional environment from mesothermal to epithermal-type deposit.

6.6 References

Bodnar, R.J., Burnham, C.W., Sterner, S.M., 1985. Synthetic fluid inclusions in natural quartz. III. Determination of phase equilibrium properties in the system H_2O-NaCl to 1000? C and 1500 bars. Geochim. Cosmochim. Acta, 49, 1861–1873.

Collins, P.L.F., 1979. Gas hydrates in CO_2-bearing fluid inclusions and the use of freezing data for estimation of salinity. Econ. Geol., 74, 1435-1444.

Diamond, L.W., Marshall, D.D., 1990. Evaluation of the fluid inclusion crushing-stage as an aid in exploration for mesothermal gold-quartz deposits. J. Geochem. Explor., 38, 285-297.

Fan, H.R., Zhai, M.G., Xie, Y.H., Yang, J.H., 2003. Ore-forming fluids associated with granite- hosted gold mineralization at the Sanshandao deposit, Jiaodong gold province, China. Miner. Depos. 38, 739–750.

Hass, J.L., 1971. The effect of salinity on the maximum thermal gradient of a hydrothermal system at hydrostatic pressure. Econ., 66, 940-946.

Hoefs, D.J., 1975. Geochemistry of Stable Isotopes. Angew. Chem. Int. Ed., 14, 75-79.

Hoefs, J., 2009. Stable Isotope Geochemistry, sixth ed. Springer-Verlag, Berlin Heidelberg, 201p.

Lawrence, D. M., Treloar, P.J., Rankin, A.H., Boyce, A., Harbidge, P., 2013. A fluid inclusion and stable isotope study at the Loulo mining district, Mali, West Africa: Implications for multifluid sources in the generation of orogenic gold deposits. Econ. Geol., 108, 229-257.

Mikucki, E.J., 1998, Hydrothermal transport and depositional processes in Archean lode-gold systems: A review. Ore Geol. Rev., 13, 307-321.

Ramboz, C., Pichavant, M., Weisbrod, A., 1982. Fluid immiscibility in natural processes. Use and misuse of fluid inclusion data: II. Interpretation of fluid inclusion data in terms of immiscibility. Chem. Geol., 37, 29–48.

Roedder, E., Bodnar, R. J., 1980 Geologic pressure determinations from fluid inclusion studies. Ann. Rev. Earth Planet. Sci., 8, 263-301.

Roedder, E., 1984. Fluid Inclusions. Rev. Miner. 12, 644p.

Sillitoe, R.H., J.W. Hedenquist, J.W., 2003. Linkages between volcanotectonic settings, ore fluid compositions, and epithermal precious metal deposits. Econ. Geol., 10, 315–343.

Sterner, S.M., and Bodnar, R.J., 1984. Synthetic fluid inclusions in natural quartz I. Compositional types synthesized and applications to experimental geochemistry Geochim. Cosmochim. Acta., 48, 2659-2668.

Sterner, S.M., Bodnar, R.J., 1991. Synthetic fluid inclusions: X. Experimental determination of P –V–T– X properties in the CO_2 –H_2O system to 6 kb and 700°C. Am. J. Sci., 291, 1–54.

Takahashi, R., Tagiri, R., Blamey, N.J.F., Imai, A., Watanabe, Y., Takeuchi, A., 2017. Characteristics and behavior of hydrothermal fluids for gold mineralization at the Hishikari deposits, Kyushu, Japan. Resour. Geol., 67, 279–299.

Zou, Z, Zhang, J.R, Hu, R.Z., 2017. Geology, fluid inclusions, and isotopic geochemistry of the Jinman sediment-hosted copper deposit in the Lanping Basin, China. Resour. Geol., 67, 384-398.

CHAPTER 7

GENERAL CONCLUSIONS

7.1 General Statement

This chapter concludes general conclusions, and recommendations for further research of the Thone Myae Song Area.

7.2 Type of Epithermal Deposit

Epithermal deposit systems form at shallow depths and at temperatures less than 300 °C (Hayba et. al., 1985); they encompass a variety of low and high sulfidation deposit, some mainly low sulfidation, display elevated silver contents and others are characterized by bonanza metal grades exceeding 30 g/t Au. Epithermal gold or gold-silver deposits may be classified in various way based on their tectonic setting, mineralization style, nature of host rocks. Hydrothermal alteration assemblage and zooning, ore fluid characteristic, the redox state of fluid and metal assemblage of the deposits (Mitchell and Leach, 1993: White and Hedenquist, 1995: White and Poizat, 1995) shown in Figure 7.1.

Most rock types can host epithermal gold deposits; however, they are most commonly found in igneous and sedimentary rocks. There are two principal types of epithermal gold deposits – Low Sulfidation (LS) and High Sulfidation (HS) Figure 7.1. Studies on epithermal gold-silver deposit have recognized as three principal varieties 1. Volcanic rock-related adularia-sericite type (low sulfidation) 1. Alunite-kaolinite type (high sulfidation), and 3. Sediment-hosted Carlin-type deposits (Berger and Henley, 1989). Low sulfidation epithermal Au-Ag deposits are distinguished from high sulfidation deposits primarily by the different sulfide mineralogy (pyrite, sphalerite, galena, chalcopyrite) typically within quartz veins with local carbonate, and associated near neutral wall rock alteration (illite clays), deposited from dilute hydrothermal fluids

(Corbett and Leach, 1998). Fluid mixing and boiling are the two principal mechanisms that cause ore minerals to be deposited. These features support the fact that the EE3 gold Prospect could be classified as an Epithermal type gold deposit in Myanmar.

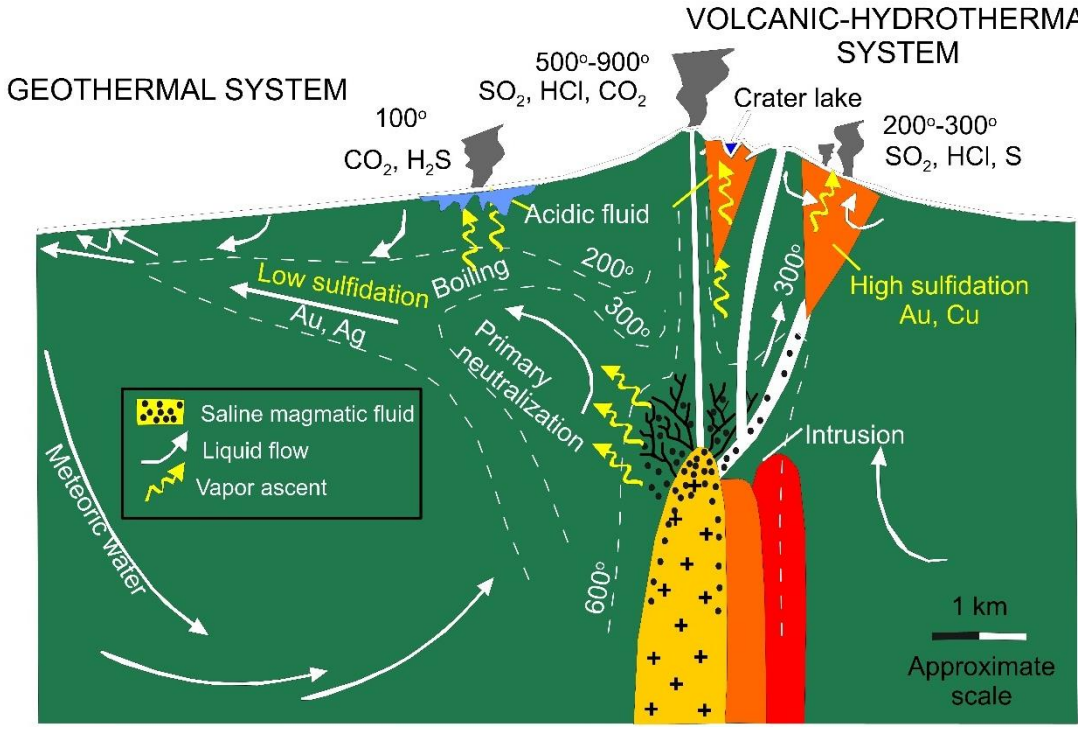

Figure 7.1 Simplified model for Low Sulfidation and high Sulfidation systems (Hedenquist and Lowenstern, 1994).

7.3 General Conclusions

Major conclusions for this research area are:

1. The EE3 deposit occurred in the Kawlin-Wuntho block in the northern part of the CMVB.
2. The gold deposit at the EE3 Prospect is hosted in Mesozoic Mawgyi Andesite.
3. Three mineralization stages are identified at the EE3 Prospect. They are (1) Stage-I quartz-carbonate-sulfide main veins, (2) Stage-II E-W trending veins that intersected the Stage-I main veins, and (3) the Stage-III veins parallel to the Stage-I main veins.
4. Stage-I veins contain pyrite, chalcopyrite, sphalerite, magnetite and native gold. Significant gold mineralization is not accompanied with the Stage-II veins.

Stage-III veins are characterized by tellurobismuthite, calaverite, petzite, native gold and magnetite associated with pyrite, chalcopyrite.

5. In the EE3 Prospect, the alteration is characterized by various amounts of chlorite and calcite away from the veins, but the altered rock at proximal parts from the vein comprise epidote, chlorite, and sericite. Based on alteration mineral assemblages, three types of alteration zones were identified (1) proximal (sericite-carbonate alteration), (2) intermediate (epidote-calcite±albite alteration) and (3) distal (chlorite-carbonate alteration) zones.
6. The coexistence of aqueous Type A liquid-rich two-phase fluid inclusions, Type B vapor-rich two-phase fluid inclusions and CO_2-rich Type C three phase fluid inclusions in the same quartz grains in the Stage-I veins is interpreted as an evidence for fluid immiscibility. Type A and Type B fluid inclusions of Stage-III also suggest boiling. Fluid immiscibility or boiling was possibly the key factor in the precipitation of gold and other metal sulfides in the EE3 deposit.
7. Estimated P-T condition of Stage-I is 180 °C and 28 bars approximately equivalent to the depth of 300 m. Estimated P-T condition of Stage-I is 176 °C and 26 bars approximately equivalent to the depth of 260 m. Estimated P-T conditions of the Stage-III is 158 °C and 21 bars which is approximately equivalent to the depth of 215 m.
8. A narrow range of $\delta^{34}S$ values (+0.5 ‰ to -3.0 ‰) near ±0 ‰ of sulfides of the EE3 Prospect suggest that sulfur was most likely derived from the leaching of the volcanic rocks that hosted the mineralization or magmatic body at depth.
9. The ore fluids in the EE3 deposit ascended along the structural conduits within the Mawgyi Andesite and the ore deposition occurred due to decreasing in pressure and immiscibility of the ore fluids.
10. On the basis of the estimated temperature and pressure conditions of the mineralization, the EE3 Prospect is likely to have formed under epithermal-type condition.
11. Wuntho-Banmauk Segment has a variety of styles of copper-gold deposits including Cu–Au–Mo porphyry (e.g., Shangalon), mesothermal Au (Kyaukpazat), polymetallic VHMS (e.g. Mahar San) and the epithermal Au deposit (e.g., EE3 Prospect).

7.4 Recommendation for Further Research

This study delivers a starting point for future studies into the ore genesis of the Thone Myae Song area, Banmauk district and of epithermal mineralization systems in the Central Magmatic Volcanic Belt. The followings summary recommendations were made for further study and exploitation.

- Mawgyi Andesite associated with mineralization should be dated in order to guess period of magmatic activity and hence the time of mineralization.
- Added analyses of hydrogen, carbon and oxygen isotopes can be used to illuminate the origin and evolution of hydrothermal fluids, and to determine conditions of ore formation.
- To do detail structural analysis of vein arrays, dikes and faults to better understand structural controls on mineralization.

7.5 References

Berger, B. R., Henley, R. W., 1989. Advances in understanding of epithermal gold-silver deposit: With special reference to the western United Staes. Econ. Geol, 403-405.

Corbett, G. J., and Leach, T. M., 1998. Southwest Pacific rim gold-copper systems: structure, alteration, and Mineralization. Society of Economic Geologists Special Publication 6, 234p.

Hayba, D. O., Bethke, P. M., Heald, P., and Foley, N. K., 1985. Geologic, mineralogic and geochemical characteristics of volcanic-hosted epithermal precious-metal deposits in geology and geochemistry of epithermal systems. Rev in Econ. Geol, 129-167.

Hedenquist, J. W., Lowensstern, J. B., 1994. The role of magmas in the formation of hydrothermal ore deposit. Nature, 519-527.

Mitchell. A. H. G., Leach, T. M., 1993. Epithermal gold in the Philippines: Island arc metallogenies, geothermal systems and geology. Academic pess.457p.

White, N. C., Hedenquist, J. W., 1995. Epithermal gold deposits: Styles, characteristics and exploration. SEG Newsletter, 1-13.

White, N. C., Poizat. 1995. Epithermal deposits diverse styles diverse origin? PACRIM Congress 95. Auckland. New Zealand, 623-628.